The University of Reading

Department of Meteorology

Identifying Large-Scale Features in the Data from a Cloud Resolving Model

Jennifer Catto

A dissertation submitted in partial fulfilment of the requirements for the degree of Master of Science in Weather Climate and Modelling.

August 2006

Abstract

The large-scale flow in the tropics is strongly connected to the deep convection that occurs in the region. Many observational and modelling studies have been performed to investigate exactly what this link is and how the cumulus scale interacts with the planetary scale. It is widely accepted that there are many different wave-like disturbances propagating along the equator which provide a possible mechanism that could lead to better prediction of tropical weather. The data from a large domain cloud resolving model covering almost the entire tropics in an aquaplanet simulation were studied. Using Fourier analysis techniques, the types of waves present in the data were found. A large range of gravity waves were found to be present. The precipitation rate data were analysed in an attempt to connect the explicitly resolved convection with the dynamical fields. The data showed superclusters with realistic westward propagation speeds at wavelengths of around 1500 km. These superclusters of convection were coupled with a wavenumber 25 Kelvin wave-type disturbance in the meridional velocity field.

This type of model provides an excellent source of data with which to study equatorially trapped waves. However, it was found in this case that the model run length of 11 days was insufficient to conclude with much certainty the types of waves and the mechanisms for their generation.

Contents

Acknowledgements

I would like to thank my supervisor, Dr Robert Plant, for all of his help and encouragement throughout this time. His positive comments have been a great motivator during the project.

I would also like to thank Dr Glenn Shutts from the Met Office for providing the data and valuable code for this project and for the very interesting meetings we had.

1. Introduction

1.1 The Importance of Clouds and Convection

Clouds in the atmosphere play a very important role in the global climate system. They provide a large uncertainty in the future climate of the Earth (IPCC 2001) and have a huge impact on humankind which depends greatly on rain. There are four main ways in which clouds affect the climate system (Arakawa 2004). Firstly, and most importantly, solar radiation is both reflected and absorbed by clouds and in turn the clouds reradiate this energy in the form of longwave radiation directly influencing the temperature at the surface of the Earth. Secondly, clouds redistribute heat and moisture fluxed from the surface of the Earth into the atmosphere. The third effect is that of precipitation produced in the clouds which affects the hydrological cycle at the surface. The last effect is that of the connection between the atmosphere and the ocean of which clouds play a part – a coupling which is extremely complex.

1.2 Convection in the Tropics

Despite the fact that the tropics cover half of the Earth's surface, there is relatively poor understanding of the circulations that occur there. Whereas for midlatitude dynamics there are well developed theories such as quasi-geostrophic theory which can explain very well the synoptic scale disturbances that occur, there is no such analogous theory for the tropics (Holton 1992). This is due in part to the different energy sources in these two regions. In the midlatitudes, the energy which drives the motion systems comes mainly from the strong north-south gradient of temperature. In the tropics it is the net latent heat released when deep convection produces heavy rain that gives most of the energy to the systems.

Where deep convection is present the vertical structure of the atmosphere shows that the large-scale circulations act to push the atmosphere out of equilibrium and the convection acts to get it back towards a stable state. Arakawa and Schubert (1974) put forward the quasi-equilibrium theory that states that this stabilisation occurs on a much smaller timescale than the destabilisation. Cohen and Craig (2004) found this adjustment time to be around one hour.

1.3 Variability and Waves in the Tropics

There are many different time- and space-scales of variability of weather in the tropics. These range from oscillations such as the quasi-biennial oscillation (QBO) up in the stratosphere, to the intra-seasonal or Madden-Julian oscillation (ISO or MJO) to squall lines which last for a few hours and individual convective events which only last about 30 minutes.

The organisation of convection into wave-like disturbances in the tropics provides potential predictability of weather (Shutts and Palmer 2005) which makes the study of these waves a very important subject for research. There have been many observational and theoretical studies into such waves in order to provide a better understanding of the variability in the tropics.

1.4 Importance of Cloud Resolving Models

Because of the strong and complex effects that convection produces in the tropics it is very important that clouds be accurately represented in general circulation models (GCMs). However, the scale at which individual deep convective clouds form is of the order of 1-2 km (LeMone and Zipser 1980) whereas even the highest resolution GCMs or climate models are of the order 100 km due to the computational expense of having any smaller grid spacing. It is therefore necessary to represent the existence and effects of clouds in a statistical way and this is called parameterisation.

Cloud resolving models (CRMs) are used as a tool to investigate the statistical effects of clouds to improve their representation in global scale models. Most CRMs have a small enough grid-spacing to explicitly resolve individual convective plumes but this means that the domain over which the simulations are performed must usually be small to keep computational expense down. This means that although the small scale effects of convection can be seen, often the domain is not large enough to capture the large scale flow which they induce (Shutts and Palmer 2005). There are different ways that have been used to try and overcome this problem for example recently Kuang et al (2005) used the Diabatic Acceleration and REscaling (DARE) approach which effectively reduces the scale difference between the convective plume scale and

the dynamical scale. They attempted a global aquaplanet simulation and found that this approach provided a valuable tool for analysing the interaction between large- and small-scales. Using the powerful Earth Simulator in Japan, Tomita et al (2005) attempted the first global CRM simulation on an idealised aquaplanet setup although the grid spacing was only 3.5km which is possibly still too coarse to capture some individual convective elements.

In this project the data from a CRM spanning 40,000km around the equator were studied in an attempt to better understand the large scale features that develop when the convection is explicitly resolved. In order to keep computational expense down, this model is configured with anisotropic horizontal grid spacing with 2.4 km spacing in the east-west direction and 40 km in the meridional direction.

The aim of this project is to investigate the types of wave features which become apparent in a very large-domain CRM with many simplifications and to try to link these waves to the equatorial wave theory presented in Gill (1982) and some of the theories of convective organisation. The following section reviews some of these organisational theories while Section 3 is an introduction to the wave theory which was first produced separately by Matsuno (1966) and Lindzen (1967). Having presented the theory a review is given of the observations of wave-like disturbances (e.g. Wheeler and Kiladis 1999, Roundy and Frank 2004). A description of the CRM and the methods used will be presented in section 5 with results and conclusions in sections 6 and 7 respectively.

2. The Organisation of Convection in the Tropics

2.1 Introduction

One of the most interesting things about convection in the tropics is the range of scales over which it organizes, from individual cumulus clouds of 1-2km to large scale structures of the order of millions of square kilometres (Wilcox and Ramanathan 2001). These organised structures take the form of cloud clusters and squall lines, up to tropical storms and hurricanes and even global scale structures like the Madden-Julian oscillation (MJO; Madden and Julian 1971).

The processes which cause the organisation of cumulus convection are not presently well understood. There are a large number of factors which are thought to be important in this organization process including cloud physics and dynamics, atmospheric waves, radiative processes and the coupling between atmosphere and ocean (Grabowski and Moncrieff 2001). Riehl and Malkus (1958) were the first to recognise that the organisation of cumulus convection in the tropics was connected to the large-scale circulations. Since then many studies have been carried out and many theories proposed for such interactions. This section aims to highlight some of the most important of these studies.

2.2 CISK and Wave-CISK

Conditional Instability of the Second Kind (CISK) was a theory first proposed in a famous paper by Charney and Eliassen (1964) (and also Ooyama 1964) and is a feedback mechanism whereby if there is low level convergence over a warm ocean, and some large-scale forcing acts to lift air to such a height where it will condense, latent heat is released. This heat warms the air so that deep cumulus convection occurs. This convection then further increases the convergence at the surface by lowering the pressure and so the loop continues. CISK states that the maximum convection occurs where there is maximum convective available potential energy (CAPE). It is this CAPE that is released when the convection occurs. The initial convergence required at the surface has to come from some large-scale system. Figure 1 shows the relationship between the warm and cold anomalies in the

atmosphere and the region of convection in a Kelvin wave (to be discussed in sections 3 and 4).

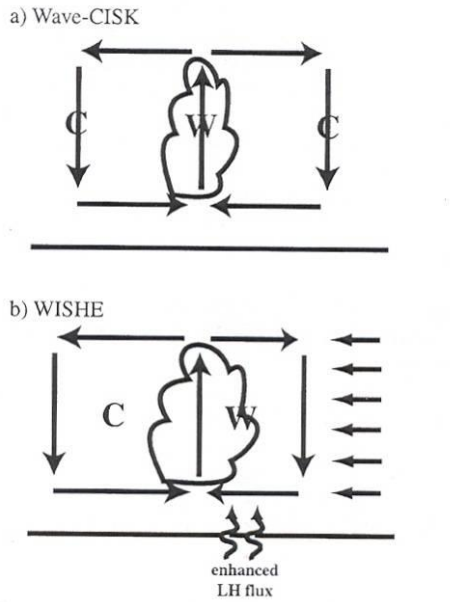

Figure 1 – *Schematic showing the relationship between warm and cold anomalies (W and C) and vertical motion in a Kelvin wave structure with a) CISK and b) WISHE (Source Straub and Kiladis 2003)*

CISK was used by Charney and Eliassen (1964) to try to explain the formation of hurricanes and in this case the source of the convergence was Ekman pumping. Other studies (e.g. Lindzen 1974) proposed that the convergence required for CISK to occur could be generated by atmospheric waves. In this case the theory is known as wave-CISK.

CISK fails to account for many observed properties of the tropics, for example the scale selection that favours instability of the larger scales, and has been greatly criticised with Emanuel et al (1994) going so far as to say that CISK has been an "influential and lengthy dead-end road in atmospheric science". However, the criticisms by Emanuel et al (1994) seem to be of a very limited classification of the CISK theory. The theory fails to take into account the effect of surface fluxes on the convection which, when considering the development of tropical cyclones especially, becomes very important. Ooyama (1982), who was one of the first pioneers of the CISK theory, did specify the importance of these fluxes in the intensification of tropical cyclones but did not give this mechanism a different name.

2.3 WISHE

It was Emanuel (1987) who gave more prominence to a different feedback mechanism which relied on the surface fluxes over the ocean to provide the energy required for convection to occur. This mechanism is known as WISHE (wind induce surface heat exchange) and is an asymmetrical process whereby the maximum convection occurs in regions of maximum surface winds. This occurs when the perturbation zonal wind velocity is in the same direction as the mean flow, therefore producing a maximum in zonal velocity in this region.

WISHE was originally intended to account for the MJO which has a period between 30 and 60 days but this mechanism actually produces maximum instability at the smallest scales. However, Yano and Emanuel (1991) modified the original WISHE model to include a coupling of the troposphere and stratosphere and found that the longer wavelength disturbances grew, giving a more realistic picture of the nature of the MJO.

2.4 Wind-Shear

A pattern of convective organisation that is evident in both midlatitudes and in the tropics is the squall line which is defined by Rotunno et al (1988) as an area of "long-lived, line-oriented, precipitating cumulus convection". That is, squall lines are long lines consisting of many convective thunderstorm cells which have grouped together and they can last for a number of hours.

The usual lifespan of a convective cell is around 30 to 60 minutes (Rotunno et al 1988). In this cycle the convection begins creating strong updrafts. This causes the cumulus to become large cumulonimbus with heavy precipitation. This precipitation then produces downdrafts due to the cooling of the air through evaporation. The downdrafts soon cut off the supply of warm air and the system decays. In regions of strong vertical wind shear, however, the downdrafts and the updrafts are in different places so that the downdraft no longer cuts off the updraft and the system stays in a steady state for a long period of time.

Many different conceptual models of this phenomenon have been developed through the analysis of data from different observational studies and three important ones are depicted in Figure 2. An early study, the Thunderstorm Project (Byers and Braham, 1949 p19) led Newton (1950) to develop his first model which he later modified to that shown in Figure 2b. Two other conceptual models developed by Zipser (1977) and Carbone (1982) although showing different patterns of shear (Figure 2a and c) have the same equivalent potential temperature structure and result in a long lived squall line showing that wind shear does play an important role in organisation of convection.

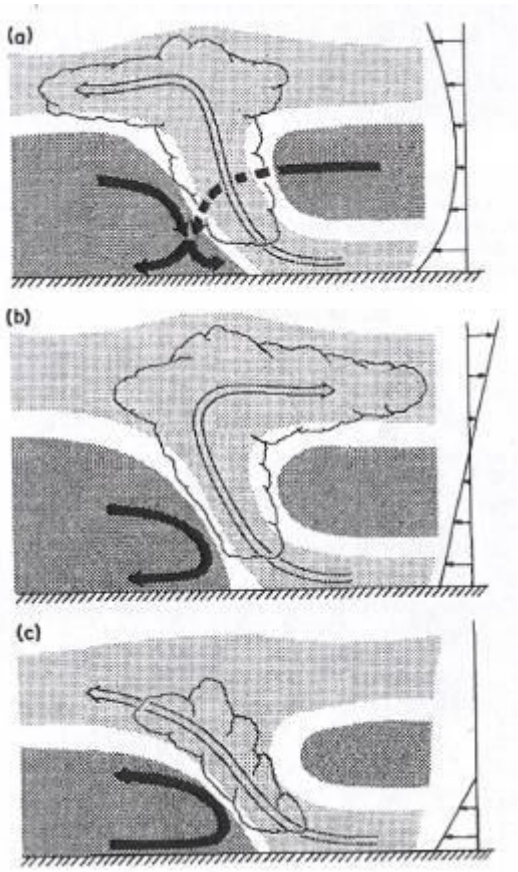

Figure 2 – *Schematics of conceptual models of squall lines from observations of a) GATE – Zipser (1977) b) the Thunderstorm project – Newton (1966) and c) a Californian squall line – Carbone (1982). Shading represents equivalent potential temperature (dark is high and light is low), small arrows represent the wind shear present and the thick arrows represent the updrafts and downdrafts. (Source - Rotunno et al 1988)*

2.5 Water Vapour

Tompkins (2001a) conducted modelling experiments to investigate if there were other factors that could organise convection other than wind-shear and sea surface

temperatures. In order to isolate the effect of water vapour he imposed a constant sea surface temperature of 300K over the model domain and a horizontally uniform fixed radiative forcing. This second step was taken to ensure that the radiative-convective feedbacks that had previously been shown to be important in convective organisation (Tompkins and Craig 1998) did not mask the other effects. A feedback loop with the water vapour seemed to be the cause of the convective organisation. This result was tested by introducing water vapour anomalies into the atmosphere and it was found that the position of the convective clusters was a direct consequence of the water vapour.

Different aspects of the role of water vapour were investigated in this experiment and it was found that when a low vertical wind shear was imposed the water vapour was still important in the convective organisation but when a strong shear was added the water vapour field was mixed in the horizontal and did not have such a great effect. It was also found that when the sea surface temperature (SST) was changed to vary in the horizontal with an imposed region of higher SST (the warm pool) beside a region of lower SST (the cold pool), the cold pool thermodynamics showed an interesting effect whereby within the region of cooler sea surface, the air contained less water vapour than in general but on the margin of the cold pool, there was more moisture. A study was performed (Tompkins 2001b) to further investigate this effect and found that the role of cold pools in generating convection is strongly related to the water vapour effect.

2.6 Other effects

The clustering nature of convection in the tropics can be partly attributed to the effect of the Earth's rotation. Liu and Moncrieff (2004) found in their numerical experiments, that rotation increases the static stability of the atmosphere in regions close to deep convection. This tends to localise the subsidence which is necessary to compensate for the upward motion. The subsidence causes drying of the atmosphere therefore inhibiting further convection. In the tropics, however, the Coriolis parameter is small and so this suppression effect does not take place, meaning that natural clustering of convection occurs most at the equator.

In fact Bretherton et al (2005) performed numerical experiments with a CRM and found that without rotational effects or mean wind and a uniform SST, the convection still clustered together eventually (after 50 days of the model run) with one area of strong convection and therefore heating and the rest of the domain remaining dry. The cause of this was found to be mainly radiative-convective feedbacks whereby the dry regions cool from the surface upwards causing further drying.

3. Wave Theory

3.1 Introduction

In this project the dispersion relations for 3 different types of waves (Gill 1982, equations 11.10.3 – 11.10.5) will be used to analyse the dataset which has been produced by the CRM. It is therefore be appropriate to give a general background of the theory on which these relations are based.

In order to understand the dynamics of the atmosphere it is necessary to make some basic assumptions and to simplify the system into one for which a mathematical model can be used as a description. It was Matsuno (1966) who originally developed this theory in relation to the atmosphere whereby the shallow water equations have been used as a starting point. They can be assumed to be valid when the hydrostatic approximation holds, that is, the horizontal length scale is much greater than the vertical length scale. Since the circumference of the Earth is approximately 40,000km and the depth of the atmosphere in which we are interested is less than 50km this assumption is valid. It is also assumed that the depth is constant in the equilibrium state and given by *H.*

The rotation of the Earth must be accounted for when deriving the relevant shallow water equations and this produces an additional acceleration term related to the Coriolis parameter, *f* where $f = 2\Omega \sin\varphi$. For low frequency waves the curvature of the Earth becomes very important. Laplace first derived the shallow water equations on a sphere, but in this case we will be considering only motion in the tropics and in a direction around the equator with small variation in latitude so for this purpose it is possible to use the beta-plane approximation. This assumes the small angle approximation, $\sin\varphi \approx \varphi$ and $\cos\varphi \approx 1$, so that f is a linear function of the latitude given by, $f = \beta y$ where $y = r\varphi$, r is the radius of the Earth and φ is the latitude.

The two momentum equations are;

$$\partial u/\partial t - fv = -g\,\partial \eta/\partial x, \qquad 1)$$

$$\partial v/\partial t + fu = -g\,\partial \eta/\partial y, \qquad 2)$$

where η is a surface perturbation, g is the acceleration due to gravity, and x and y are the zonal and meridional directions with corresponding wind velocities, u and v. The continuity equation is given as

$$\partial\eta/\partial t + \partial(Hu)/\partial x + \partial(Hv)/\partial y = 0. \qquad 3)$$

These three equations can be combined to give one equation, for which a solution will be sought,

$$\partial^2\eta/\partial t^2 - c^2\Delta\eta + fH\zeta - \beta Hu = 0, \qquad 4)$$

where ζ is the vertical component of vorticity, Δ is the horizontal Laplacian, and $c = \sqrt{gH}$, known as the phase speed.

3.2 Equatorially trapped waves

The term equatorially trapped refers to waves which can propagate both zonally, parallel to the equator, and vertically, but which die away with increasing distance from the equator. This trapping occurs due to the Coriolis parameter decreasing to zero on the equator producing sine waves that cross this straight line boundary. In the case of inertio-gravity waves the frequency, ω, is conserved following wave packets. One of the conditions of the existence of this type of wave is that the frequency of the wave is greater than the Coriolis parameter (Andrews et al 1987) so when the energy moves away from the equator where f = 0, it comes upon a latitude where its frequency is equal to f and the energy cannot go any further. It therefore gets reflected back producing a wave that is trapped. There are 4 main types of equatorially trapped waves that will be looked at here, the Kelvin wave, Rossby waves, mixed Rossby-gravity waves and inertio-gravity waves. Initially the dispersion relations for these 4 wave types will be derived assuming no vertical propagation, then in section 3.3 the theory will be expanded to consider the vertically propagating waves which will be studied from the model data.

3.2.1 The Kelvin Wave

The Kelvin wave is a special case of these waves in that it involves no meridional motion and this can be seen in Figure 3a.

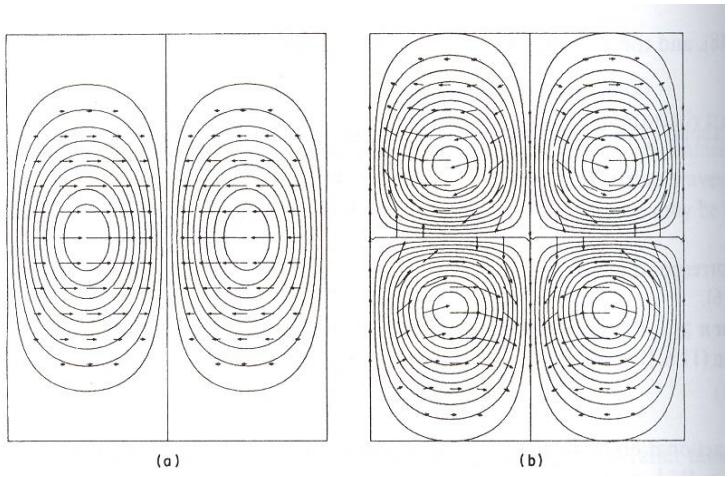

Figure 3 - *Arrows show wind and contours show surface elevation for a) a Kelvin wave and b) and eastward-propagating mixed Rossby-gravity wave. (Taken from Gill 1982)*

The general solution for the Kelvin wave is found to be the sum of two non-dispersive waves travelling in opposite directions. The physical solution is then the wave which decays exponentially as distance from the equator increases which is,

$$\exp\left(-\tfrac{1}{2}\beta y^2/c\right)G(x-ct), \qquad 5)$$

where G is an arbitrary function (the other solution having an exponential increase in amplitude away from the equator). This shows that the Kelvin wave only propagates eastwards since G is only a function of $(x\text{-}ct)$ and not $(x+ct)$, and gives the linear dispersion relation between frequency and zonal wavenumber,

$\omega = kc$.

3.2.2 Other Waves

As well as the Kelvin wave there are other types of wave that can be trapped by the equatorial waveguide. Planetary scale waves (or Rossby waves as they will be called here) result from the poleward potential vorticity gradient, also known as the beta-effect, and have relatively low frequency. Pure gravity waves however, are high frequency waves caused by the stratification of the atmosphere. The pure gravity

wave will not be considered here in the theory but will be discussed in section 4.3. The inertio-gravity wave is also a high frequency wave but it is produced by the interaction of the stratification and rotation of the Earth. There is also a mixed Rossby-gravity wave which behaves like Rossby waves at low frequencies and like inertio-gravity waves at higher frequencies.

For these waves solutions of the form,

$$\exp\left(ikx - i\omega t\right), \qquad 6)$$

are sought. Again assuming that the waves decay away from the equator a solution is found which gives the dispersion relation as,

$$\left(\omega/c\right)^2 - k^2 - \beta k/\omega = \left(2n+1\right)\beta/c\,, \qquad 7)$$

where *n* is an integer which is sometimes called the meridional wavenumber or the mode number. These curves can be seen in Figure 4 along with the Kelvin wave dispersion curve.

For $n = 0$, the mixed Rossby-gravity wave (shown in Figure 3b) equation (7) can be reduced to

$$\omega/c - k - \beta/\omega = 0\,, \qquad 8)$$

using algebra involving parabolic cylindrical functions which will not be repeated here but which can be found in Gill (1982) or Andrews et al (1987).

For $n \geq 1$ the inertio-gravity wave dispersion curves are the upper curves in Figure 4 so for these high-frequency curves $\beta k/\omega$ in equation (7) is small so the dispersion relation is

$$\omega^2 \approx \left(2n+1\right)\beta c + k^2 c^2. \qquad 9)$$

The Rossby wave dispersion curves are the lower curves in the same figure and for these low-frequency waves the term ω^2/c^2 is small so that equation (7) becomes

$$\omega = -\beta k/\left(k^2 + \left(2n+1\right)\beta/c\right). \qquad 10)$$

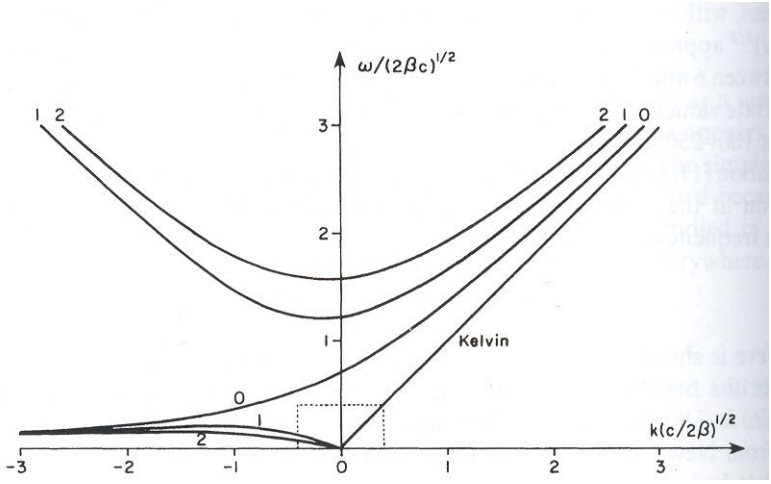

Figure 4 – *Dispersion curves for equatorial waves. The vertical axis shows frequency in units of* $(2\beta c)^{\frac{1}{2}}$ *and the horizontal axis is the zonal wavenumber in units of* $(2\beta/c)^{\frac{1}{2}}$. *The curve labelled 0 is the mixed Rossby-gravity wave. The upper two curves show the first two inertio-gravity wave modes and the lower two curves show the first two Rossby wave modes. (Taken from Gill 1982).*

3.3 Relation between horizontal and vertical motion

When the consideration of vertical propagation is included in the wave theory these dispersion relations must be modified slightly to give a connection between the zonal and vertical wavenumbers, (*k* and *m*). The solutions are now proportional to

$$\exp(ikx + imz - i\omega t). \qquad 11)$$

The derivation of the dispersion relations continues as before but now *c* which appears in equations (7) to(10) is equal to N/m where *N* is the buoyancy frequency (assumed to be constant, the value of which will be found in section 5.4).

Using non-dimensional forms of *m* and *k* given by

$m^* = m\omega^2/\beta N$ and $k^* = k\omega/\beta$

the final equations are

$$m^* = k^*, \qquad 12)$$

for the Kelvin wave,

$$m^* = k^* + 1, \qquad 13)$$

for the mixed Rossby-gravity wave where n = 0,

$$m^* = n + \tfrac{1}{2} \pm \left\{\left(k^* + \tfrac{1}{2}\right)^2 + n(n+1)\right\}^{\frac{1}{2}}, \qquad 14)$$

for the rest of the waves, the positive solution giving inertio-gravity waves and the negative solution, Rossby waves. The corresponding curves are shown in Figure 5.

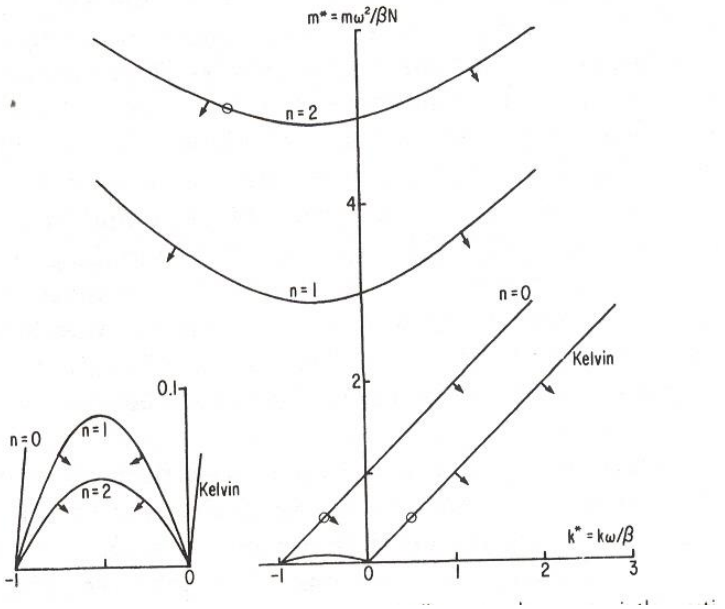

Figure 5 – *Dispersion curves for vertically propagating equatorially trapped waves. The upper curves show the gravity wave solutions and the lower curves (and inset enlargement) are the Rossby wave solutions. The x- and y- axes are the non-dimensional values k* and m*. (Source – Gill 1982)*

3.4 Equivalent Depth

The equivalent depth is a parameter used to relate the shallow water equations with the vertical structure equations. It has not been used in the theory and will not be used in the analysis performed in this project. However, it is a parameter which is widely used in the observational studies of equatorially trapped waves so the definition is given here for clarity.

The equivalent depth, H_e, relates the gravitational acceleration and the value c defined earlier by

$$H_e = c^2/g\,.$$

4. Waves in the Atmosphere

4.1 Introduction

The wave theory which was presented in the previous section was first produced by Matsuno (1966) and separately by Lindzen (1967). This type of theory has since been used extensively to try to explain the spatial and temporal variability of weather in the tropics. It has long been known that a lot of the weather in the tropics is organised into wave like features which propagate along the equator. These disturbances manifest themselves in many of the observable fields, for example temperature, winds and pressure and they occur on many different time and space scales. In order to use these waves as a possible predictor for weather in the tropics it is important to connect the large scale structures with the convection. As Yang et al (2003) put it "a key question … is the relationship between the dynamical structure and the convection", that is, the coupling of the waves with convection which is presently quite poorly understood.

4.2 Low Frequency Waves

One of the largest of the oscillations in the equatorial region is the quasi-biennial oscillation (QBO) (Lindzen and Holton 1968) which is a disturbance in zonal winds between heights of 20 and 30 km, with an average period of 28 months. The winds alternate between easterlies and westerlies and the disturbance propagates downwards. The theory put forward by Lindzen and Holton (1968) was that vertically propagating equatorial gravity waves interact with the mean flow to produce a much longer timescale oscillation. Gravity waves will be further discussed in the next section.

Questions regarding the momentum budget in the QBO prompted Wallace and Kousky (1968) to investigate synoptic scale disturbances using radiosonde data. They used wind and temperature data in this investigation and found evidence for a vertically propagating Kelvin wave-type disturbance in winds and temperature in the stratosphere with a period of about 15 days. The temperature fluctuation was found to

have a phase lag of a quarter wavelength behind the zonal wind which agreed with the Kelvin wave theory of Holton and Lindzen (1968).

Shortly before Wallace and Kousky's (1968) study, Yanai and Maruyama (1966) had found evidence for different waves with a period of 5 days. These disturbances were not of the Kelvin wave-type as they showed a meridional component of motion as well as zonal and vertical motion and the zonal propagation was found to be westward. (It was shown in section 3 that Kelvin waves are purely eastward propagating.) These two early studies, despite only having a short period over which data was collected (e.g. 6 months; Wallace and Kousky 1968) clearly identified the existence of different waves in the tropics. This indicated that there were different wave modes contributing to the observed variability of weather in this region and since then there has been a huge amount of interest in investigating the modes present in both the troposphere and the stratosphere along with what effects they have on convective activity.

Different methods have been used to investigate these wave modes and their coupling with convection. Some of the early studies used the first satellite pictures of cloudiness (e.g. Chang 1970). Zangvil (1975) and Zangvil and Yanai (1980, 1981) used power spectrum analysis of the satellite cloudiness data to reveal the existence of Kelvin waves, inertia gravity waves, mixed Rossby-gravity waves and Rossby waves. Again, these studies used only data from 6 month periods so the results suffered from the effect of not including longer timescale variability. The fact that only cloudiness data were studied misses an important factor in the equatorial circulation and that is the connection between said cloudiness and the dynamical fields.

Using an 18 year long record of outgoing longwave radiation (OLR) data from the National Oceanic and Atmospheric Administration (NOAA) as a proxy for cloudiness and other complementary datasets, Wheeler and Kiladis (1999; from herein WK) produced a study which aimed to investigate the "dominant frequencies and wavenumbers" of tropical convection. Using the spectral analysis method developed by Hayashi (1982) (which will be discussed in the conclusions) they produced strong evidence for the existence of Kelvin waves and mixed Rossby-gravity waves with equivalent depths between 12 and 50 m. This study concentrated on waves with

periods ranging from the intraseasonal down to 1.25 days but the main focus was on the convective coupling of the waves and so a summary of their results will be presented here. They found that an equatorial Kelvin wave with quite a wide range of frequencies and zonal wavenumbers (see Table 1) could account for almost the same amount of convective variability as the MJO despite being very different to this intraseasonal oscillation. The equatorial Rossby wave for which they found evidence could account for less on a tropics wide scale but in particular regions away from the equator it was seen to have a large effect.

One of the interesting conclusions of the WK study was that the coupling of convection with waves seems to give them a smaller phase speed that they would have if there was no moisture involved. This is an indication that simple linear wave theory is not enough to account for all of the variation in the tropics.

Table 1 – *Summary of wave types observed by Wheeler and Kiladis (1999)*

Wave-Type	n	Wavenumber	Period
Kelvin wave	-1	2 to 8	3-20 days
Equatorial Rossby wave	1	6	10-15 days
Mixed Rossby-gravity wave	0	up to 4	3.5-6 days
Eastward gravity wave	0	up to 8	2-4 days
Westward gravity wave	1	4 to 14	1.25-2.5 days
Westward gravity wave	2	1 to 10	1-2 days

The large-scale dynamical fields (e.g. wind and divergence) that occur due to various types of waves were presented by Wheeler et al (2000) and Yang et al (2003). Figure 6 shows these fields for the Kelvin wave, the n = 1 and 2 Rossby wave, eastward and westward mixed Rossby-gravity (EMRG and WMRG) and n = 1 eastward and westward gravity waves (EG and WG). All of the waves shown have zonal wavenumber 1. For odd n the structure is symmetric about the equator and for even n it is antisymmetric. It can be seen from these diagrams also that for n even the zonal wind component is zero at the equator and for n odd the meridional component is zero. Yang et al (2003) also pointed out where the maximum convection should occur with respect to these waves if the WISHE mechanism is considered. These are the regions circled in blue in Figure 6. The winds here are easterly perturbations so that added to the mean zonal wind will have the strongest surface winds.

Wheeler et al (2000) also found that the vertical structure of the temperature anomalies associated with the waves had a boomerang shape. The height at which the elbow of the boomerang occurs represents the boundary at which the upward and downward phase propagations meet. Using the same linear regression analysis as they used for the fields of divergence and winds, they found that the vertical wavelengths of the waves propagating into the stratosphere are between 6 and 8 km.

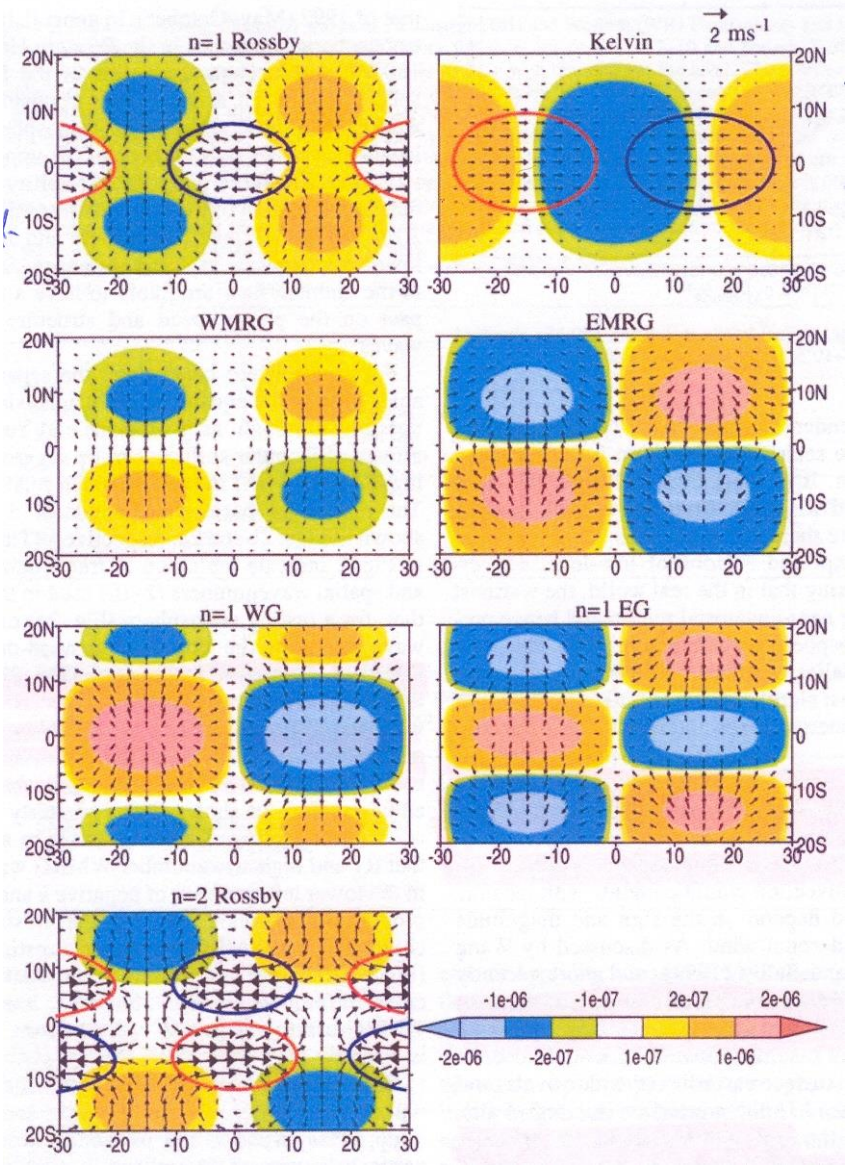

Figure 6 – *Horizontal wind (vector ms^{-1}) and divergence (colours – blue is convergence and pink is divergence, s^{-1}). Colour circles for Kelvin and Rossby waves indicate regions where convection would likely occur considering surface energy fluxes. (Source – Yang et al 2003)*

Roundy and Frank (2004) continued the work of Wheeler and Kiladis (1999) by using different data and less constraints to produce a climatology of waves focussing on clouds and humidity. They found that precipitable water (PW) used together with

OLR provided a better dataset on which to perform their analysis. Roundy and Frank (2004) used the same sort of spectral analysis methods as WK and their results indicated that perhaps the equatorial beta plane linear wave theory is far more inadequate for explaining the convective variability in the tropics than WK found.

4.3 Gravity Waves

Gravity waves in the stratosphere are particularly important with respect to convection as deep tropical convection can actually trigger these high frequency oscillations. The waves then go on to influence the circulation patterns in the middle atmosphere (Andrews et al 1987). Due to the relatively high frequency of these waves they can be difficult to observe with the usual methods of radiosondes or rockets as these types of profiles are not gathered at short enough time periods (Alexander et al 2000).

Alternative techniques need to be used to study these waves and Alexander et al (2000) used measurements of 3-D wind velocities measured by the NASA ER-2 aircraft. Although the errors in the measurement technique were quite large due to the practicalities of taking measurements from an aircraft which may change direction or height quickly, the fact that the main interest was in wavelengths in the horizontal of about 10km or greater meant these errors could be greatly reduced through averaging. Their results showed that the largest momentum flux occurred over the highest clouds (i.e. there is a strong relationship between gravity waves and deep convection).

This forcing by convection of gravity waves in the stratosphere has been attributed to the latent heating that occurs in the convection (Manzini and Hamilton 1993). Manzini and Hamilton (1993) found that the wave response in a full GCM was very similar to that in a linear model with waves forced only by heating suggesting that linear analysis is quite appropriate for this sort of study.

Alexander et al (2000) and Pandya and Alexander (1999) both performed spectral analysis on the numerically simulated waves generated by convective heating finding a broad spectrum of vertically propagating gravity waves. The vertical wavelengths of these waves were between 6 and 10 km (Pandya and Alexander 1999) which was

dependent on the depth of the convective heating and the increase in static stability at the tropopause. However, these waves were found to have a peak in the horizontal wavelength power spectrum of about 10 km, much shorter than the waves that will be analysed in this project. A 2-dimensional CRM developed by Tulich and Randall (2003) showed large-scale convectively coupled gravity waves with a vertical structure very similar to the observations of the Kelvin wave (Wheeler et al 2000). Their results show that convection is strongest when there is a cold anomaly at the tropopause and the surface and a warm anomaly in the mid troposphere.

It has been shown in this section that there have been many observations of waves in the atmosphere with varying frequencies and wavelengths. In this project, only waves with relatively short periods (less than 2 days) will be analysed due to the short model run of only 11 days. The next section will describe the data that will be used for this analysis, where they have come from and what methods will be used to study them.

5. Tools and Methods

This section describes the model used from which the data were taken and compares its configuration with other CRMs. The methods used to analyse the data are presented along with a brief test of this method. An analysis of the errors affecting the results is given and finally the value of the buoyancy frequency parameter, *N*, is calculated.

5.1 The Model Used in this Study

As was mentioned in the introduction, due to computational restrictions cloud resolving models are unable to cover the entire globe with a realistic set-up. For this reason different schemes are used to reduce the computational cost in order to use CRMs to gain better understanding of the atmosphere. In the past many large domain CRMs have been limited to 2 dimensions (e.g. Grabowski and Moncrieff 2001, Oochi 1999) and three-dimensional models have been limited in domain size. Both of these simplifications produce their own complications and problems.

A limited domain size means that properties of the rest of the atmosphere have to be parameterised and different boundary conditions used. For open boundary conditions it is assumed that the rest of the atmosphere is everywhere the same and maintains this homogeneity (Mapes 2004). The wind speeds at the boundaries therefore have to be specified and will not change realistically. Periodic boundary conditions, on the other hand, assume that the rest of the atmosphere behaves the same as in the domain. Mapes (2004) stated that this has the effect of trapping vertical motion within the domain. Petch (2006) through sensitivity studies found that the minimum domain size required for the development of realistic convection in a 2D model is around 100 km and in a 3D model 25 km. This size of domain will show the early development of convection sufficiently but is not large enough to see the organisation of the individual convective plumes.

Here, a large domain 3 dimensional cloud resolving model was developed by Glenn Shutts from the UK Met Office. It covers a 40,000 km cyclic strip representing approximately the equator and reaches to 23° North and South on a beta-plane with 50

height levels up to 30 km with a damping layer in the top 4 km. In order to overcome partially the computational expense of such a setup, the model employs the method of anisotropic grid spacing. The grid used is 2.4 km in the east-west direction and 40 km in the north-south direction. This allows a larger area in which the convective systems can grow and develop with the aim of observing how large-scale dynamics evolve when the convection is resolved (although Bryan et al 2003 indicated that to truly resolve cumulus convection, a grid length of 200m is required). One of the problems with this set up is that the updrafts and downdrafts associated with the convection will essentially become two-dimensional. Since in this project only the data from one latitude (i.e. the equator) are being analysed, this problem should not be an issue. In this case the periodicity of the boundary conditions in the zonal direction is a suitable setup since the motions are moving all the way around the equator and there are no assumptions required to be made. In the meridional direction the periodic boundary conditions mean that there is a big jump in the Coriolis parameter (given by βy in the case of a beta-plane set-up) at the northern and southern boundaries. This problem has little consequence in this model and in the analysis since the values of v at the boundaries are small and the equatorially trapped waves have negligible amplitude there (Shutts 2006).

The model was initialised with zero water vapour mixing ratio which was actually unintentional. In the similar run in Shutts (2006) the initial profile for the water vapour mixing ratio decreased with height approximately exponentially from about 15 g/kg at the surface to zero at a height of 12 km. Figure 7 shows a plot of q after 5 days at one particular point on the equator and the profile looks similar to the initial reference profile from Shutts (2006) showing that by this time the model has adjusted itself fairly quickly from an unusual starting point. This initial lack of water vapour is probably the reason why the precipitation data show no rainfall until after almost 3 days (shown later in section 6.6).

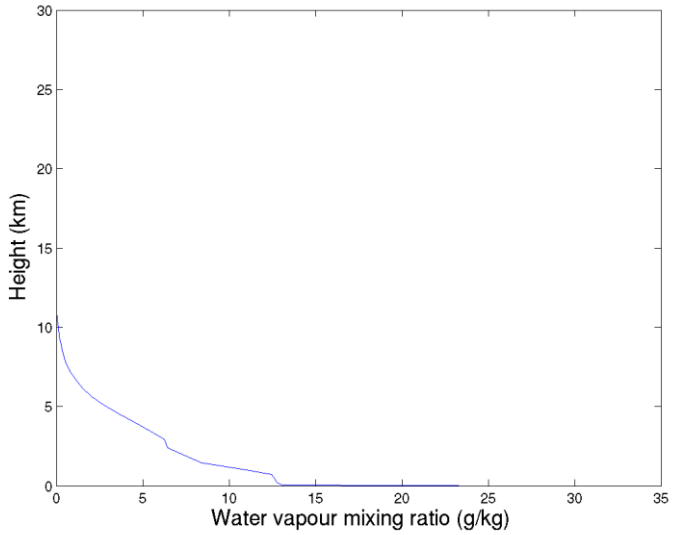

Figure 7 – *Water vapour mixing ratio (g/kg) with height after 5 days of the model run.*

In the tropics from 30^{o} North to 30^{o} South the prevailing winds are both equatorwards and westwards. This is due to the descending air at the edges of the tropics flowing towards the equator and being deflected westwards due to the Coriolis force and these winds are known as the trade winds. This model does not have any trade wind forcing function which would act as a zonal momentum sink. Without this forcing the precipitation does not become concentrated in a band about the equator but is more uniformly distributed in the meridional direction (Shutts 2006) although still decreases towards the northern and southern boundaries. Imposed on the flow is a geostrophic easterly wind of 5 ms^{-1} which is typical at the equator. Maximum sea surface temperature is at the equator and has a value of 301 K which varies as the square of meridional distance to a minimum of 299.2 K at the northern and southern boundaries. Sea surface temperature gradients were shown in section 2 to be an important factor in the organisation of convection so this variation with latitude is an important feature.

The radiation scheme is switched off in this model run but instead a cooling rate of 1.5 K/day is imposed throughout the troposphere. This discounts any possibility of the convective organisation which will be shown later to be present in the data being caused by radiative-convective feedback mechanisms.

The model is initialised with a reference potential temperature profile which is shown in Figure 12 in section 5.4. This is a typical vertical profile for the atmosphere. In the model itself, the total potential temperature is defined as follows,

$$\theta_{tot} = \theta_{ref}(z) + \theta'(x, y, z, t), \qquad 15)$$

where the value $\theta'(x, y, z, t)$, from herein given as θ', is the outputted value of potential temperature.

5.2 The Data Used

As the domain is so large in the zonal direction, due to disk space considerations, it was decided only to gather data from 64 points spread evenly around the equator. At each point the values of zonal, meridional and vertical wind (*u*, *v* and *w* respectively), potential temperature perturbation and water vapour mixing ratio (θ and *q*) were gathered for each height level. This provided a basis for the analysis. The precipitation rate from every single grid point along the equator was also gathered in order to try to make a connection between the convection and the dynamical fields.

The data had to be extracted from the 64 separate files by way of some Fortran 90 code that was provided by Glenn Shutts and amended for use on the local computers. More code was then developed to output the fields into a format for producing plots using Matlab.

5.3 Method for Estimating Wave Types

5.3.1 Wave Analysis Methods

The analysis performed in this project follows that performed in Shutts (2006) and the results will be compared to those therein.

Any series of ordered data may be described in terms of a number of sinusoidal waves which are superimposed upon one-another. This is the basis of Fourier analysis (Bloomfield 1976). These sinusoids will be in the form

$$A(z,t)\cos\left[\frac{2\pi Kx}{L_x}+\phi(z,t)\right] \qquad 16)$$

where $A(z,t)$ is the amplitude and $\phi(z,t)$ is the phase (as a function of height, *z*, and time, *t*) of the zonal wavenumber *K* component of whichever field is being analysed. L_x is the length of the domain in the zonal direction (Shutts 2006). For a number of different values of *K*, the amplitude and phase of the waves will be calculated. In order to find these coefficients of the sinusoidal functions, the discrete Fourier transforms of the data series must be computed. This was done with a method called the Fast Fourier Transform (FFT) using Fortran 90 code adapted from previous analysis. The code was originally provided in Fortran 77 format and was adapted for use on local computers and for the data in use. The coefficients were then plotted on a time versus height plot (e.g. Figure 8) in order to pick out the waves which were present.

5.3.2 Identifying Waves in the Data

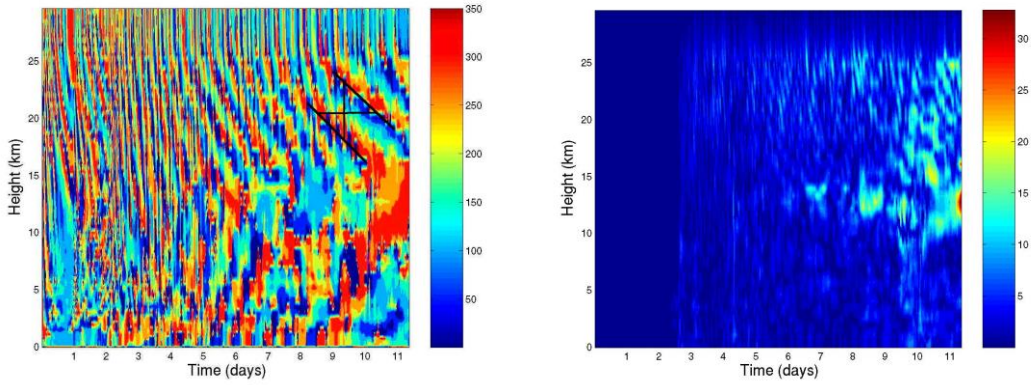

Figure 8 – *Plots showing phase (left) and amplitude (right) for the zonal wavenumber 11 in v. The slanted black lines added to the phase plot show an estimate of the lines of constant phase. The vertical line shows the vertical wavelength (h) and the horizontal line the period. In the phase plot the scale goes from 0 to 360^o (blue to red) and for the amplitude from 0 to 33 ms^{-1}.*

The phase plot shown in Figure 8 is an example of the type of plot used to calculate the period and vertical wavelength of the waves in order to use this data in the dispersion relations given in section 3. The constant phase isopleths were drawn on by hand after being chosen subjectively as the best lines to fit the contours. The vertical wavelength is the distance between these isopleths in the vertical direction and the period is the same in the horizontal direction. The horizontal and vertical lines were then drawn in order to measure these values. The phase plot shown in Figure 8, in the region where the lines are drawn, shows the colours ranging gradually from red to blue with increasing time. This is indicative of decreasing phase with time and therefore westward motion. Increasing phase with time indicates eastward motion. The effect of the 4 km deep damping layer can be clearly seen in the plots in Figure 8 as the waves die away above a height of 26 km.

Initially the period was used in the dispersion relations for the different types of waves and a table drawn up to test whether any of the theoretical waves seemed to estimate sensible vertical wavelengths or phase speeds. This provided convincing evidence that the linear wave theory could indeed represent some of the visible waves and the analysis was continued in a slightly different way. These tables are shown in Appendix C for completeness.

From the measured values of period and vertical wavelength, the required values were found from the equations

$$\omega = 2\pi/T\,, \qquad 17)$$

$$m = 2\pi/h\,, \text{ and} \qquad 18)$$

$$k = 2\pi \times K/L_x\,, \qquad 19)$$

where L_x is the domain length in the zonal direction as in equation 16. These values were used to find $m^* = m\omega^2/\beta N$ and $k^* = k\omega/\beta$ and the results plotted on a graph of the ideal dispersion relations given by equations 12 – 14 in order to compare and try to estimate what type of wave is present in the data. Since the Fourier analysis method does not split the data up into westward and eastward moving components, when the data is plotted onto the dispersion curves plot, the sign of k^* needs to be chosen according to the change of phase with time, with k^* positive for eastward moving waves and k^* negative for westward moving waves.

This method was tested using the data in Shutts (2006) from the plots given in Figure 9 and Figure 10. In that run the horizontal domain was 3,840 km (small compared to the model run used for this project) and the model configuration was quite different but a brief analysis of those results will indicate how useful the analysis method will be on the data from the larger domain model studied here.

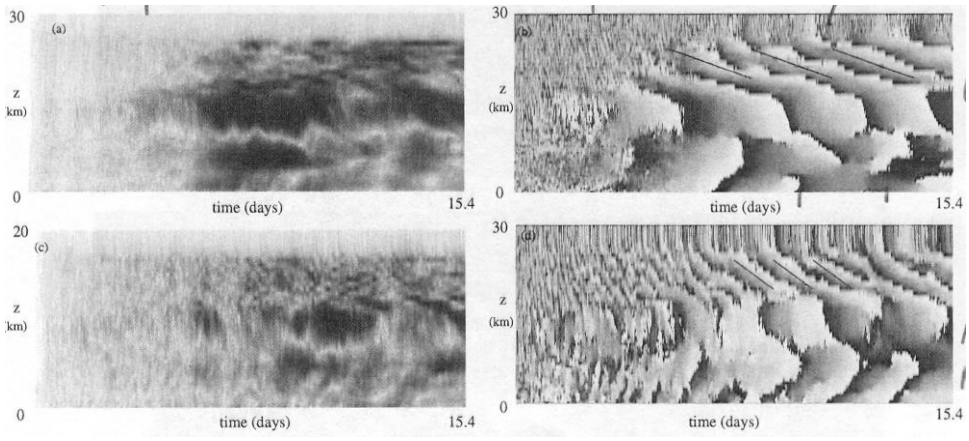

Figure 9 – *Amplitude (left) and phase (right) plots for u (top) and v (bottom) for wavenumber 1. The parallel black lines added to the phase plots show the constant phase isopleths.*

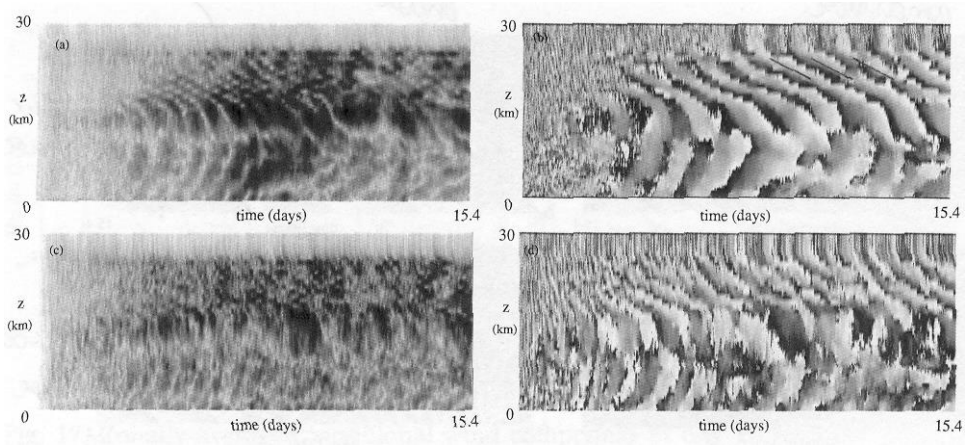

Figure 10 – *As Figure 9 but for wavenumber 2.*

The period was taken from the information in Shutts (2006) and the vertical wavelength measured by hand so that the values of k^* and m^* could be calculated. The values are shown in Table 2 and the results plotted in Figure 11. It can be seen that the results match well with the linear wave theory, confirming the conclusions in Shutts (2006).

Table 2 – *Summary of results taken from Shutts (2006). The vertical wavelength was measured from the plots shown in Figure 9 and Figure 10*

Field	*K*	Period (hours)	*h* (km)	*k**	*m**	Phase Speed (ms^{-1})	Type of Wave
u	1	69	4.9	1.8	1.78	15.4	Kelvin
u	2	35.7	3.65	6.96	8.94	31.9	*n=1* gravity
v	1	33.4	5.22	3.72	7.15	14.9	*n=2* gravity

The plots of amplitude (Figure 8) were used to confirm that the waves being studied did have a significant signal and were not just noise produced by the model. The example shown in Figure 8 has amplitude of between 12 and 20 ms^{-1} at the height at which the waves have been analysed. These plots have not been included in this report since most of them show roughly the same pattern but each one was checked before the analysis took place.

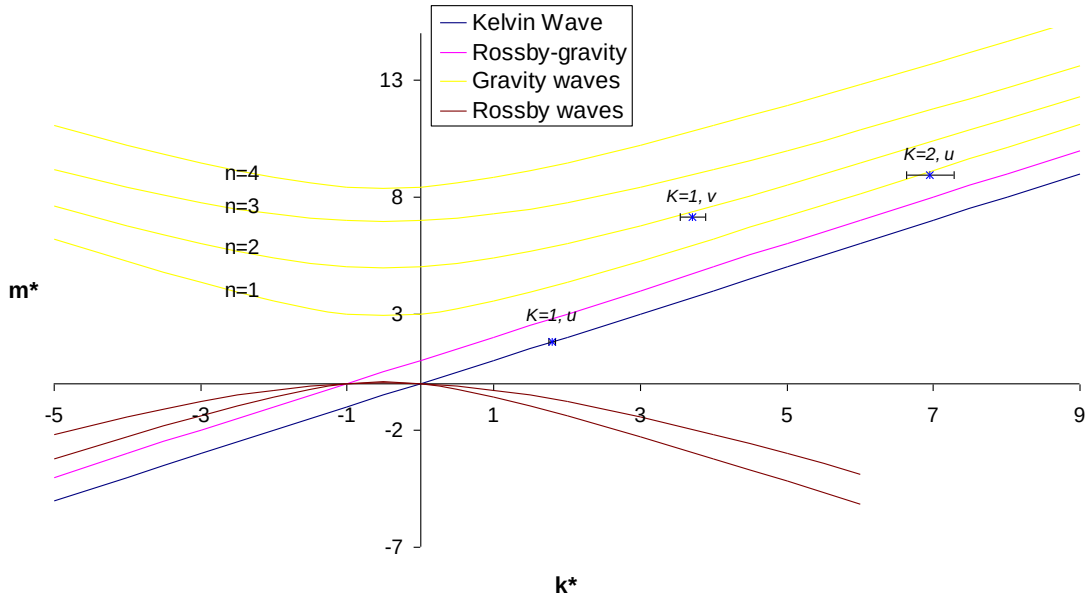

Figure 11 – *Dispersion curves with points plotted for wavenumber 1 in u and v and wavenumber 2 in u for the data from Shutts (2006).*

5.3.3 Errors

The method used to measure the period and vertical wavelengths of the phase plots obviously incurs significant human errors. This section will give a brief derivation of those errors which have been plotted on figures such as Figure 11.

The main error that occurred in the analysis procedure was in the judgement of the correct position of the constant phase isopleths. The error in period was estimated to be ±5054 seconds and in vertical wavelength, ±84 m. Basic error analysis was used to compute the errors in the calculated values. As an example the error in frequency will be calculated here. The relation between period (T) and frequency (ω) is $\omega = 2\pi/T$ and the error relation is $\Delta\omega = \frac{\partial\omega}{\partial T}\Delta T$ giving

$$\frac{\Delta\omega}{\omega} = \frac{\Delta T}{T} = \frac{\Delta k^*}{k^*} \quad . \qquad 20)$$

In a similar way the error relation between the measured vertical wavelength (*h*) and the vertical wavenumber *m* is

$$\frac{\Delta m}{m} = \frac{\Delta h}{h} \qquad 21)$$

which gives the error for *m** as the combination of 3 other errors as

$$\Delta m^* = m^* \left(\frac{\Delta m}{m} + \frac{2\Delta\omega}{\omega} + \frac{\Delta N}{N} \right) \qquad 22)$$

and the value of ΔN will be calculated in the next section.

5.4 Calculating the buoyancy frequency, N

The buoyancy frequency is a measure of the stratification of the atmosphere and is related to the potential temperature and the acceleration due to gravity as follows,

$$N^2 = \frac{g}{\theta_z} \frac{\partial \bar{\theta}}{\partial z}, \qquad 23)$$

where $\bar{\theta}$ is the average value of potential temperature at each level and θ_z is an appropriate value of potential temperature for the height range in question.

As was discussed in section 5.1, the model used in this study was designed with an initial reference profile of potential temperature. This can be seen in Figure 12 showing a surface value of 299 K and increasing slightly with height in the troposphere up to 380 K at a height of approximately 18 km. Above this height the potential temperature increases rapidly with height which is what would be expected in the stratosphere.

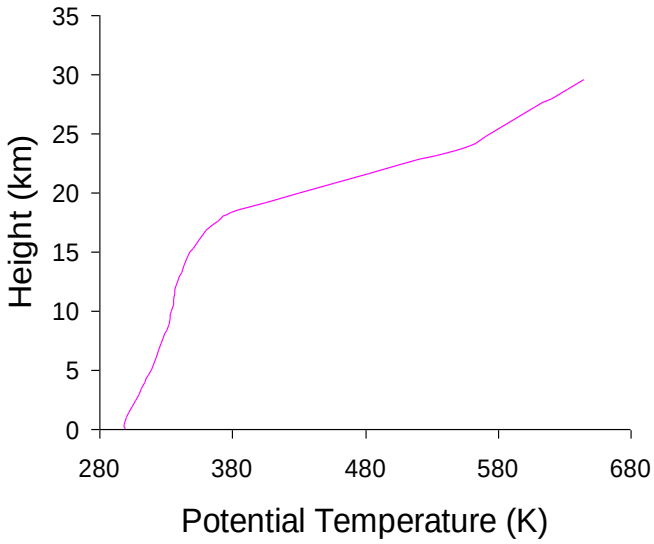

Figure 12 – *Reference profile of potential temperature with height.*

Over the model run the potential temperature deviates from this reference profile and Figure 13 shows the zonally averaged potential temperature perturbations. It is interesting to note that from days 1 to 4 there is a cooling in the troposphere and not much happening in the stratosphere. At the start of the model (as was discussed previously in section 5.1) there is no water vapour and therefore no convection until around day 3. Therefore, the cooling that can be seen is due to the imposed cooling rate at all heights of 1.5 K/day with no convective heating to compensate. From days 4 to 8 the cooling decreases in the troposphere as the convection provides the necessary latent heat to counteract the cooling. There is also significant change in the stratosphere until day 8 showing that the convection that is occurring is also transferring some energy into the middle atmosphere. From day 8 onwards the perturbation values do not change very much. This indicates that after this length of time the model has finished spinning up.

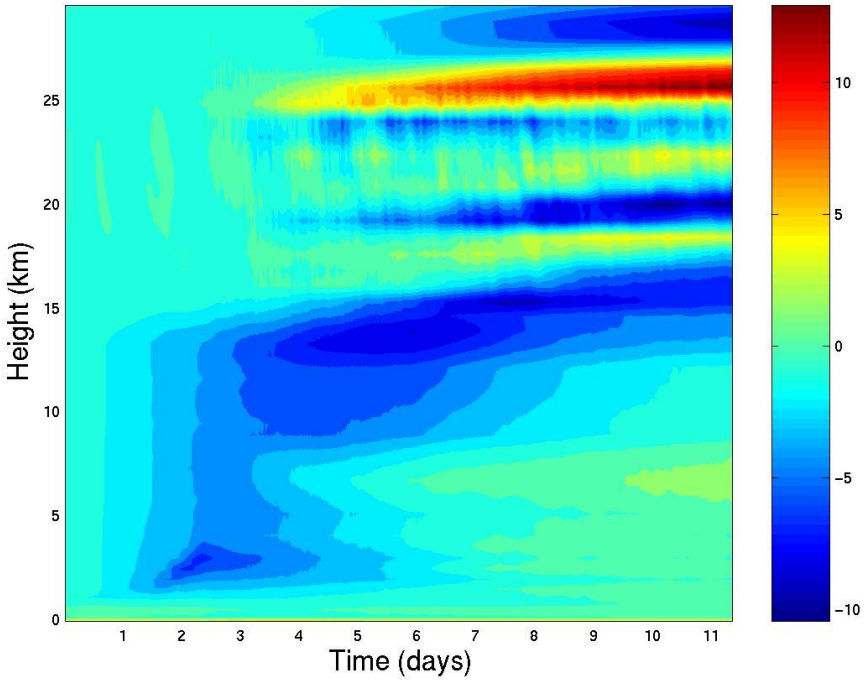

Figure 13 – *Zonally averaged potential temperature perturbations over the model run (K)*

In this study the waves that will be looked at are stratospheric waves usually between a height of 20 km and 25 km therefore this is the height range over which *N* will be calculated. Looking at the zonally averaged perturbations in Figure 13 it would seem as though the actual potential temperature by day 11 is quite a lot different to the initial reference profile. However, when looking at the overall values (θ_{tot} as defined in equation 15, shown in Figure 14) the perturbations are not significant. Therefore, in order to calculate the gradient of potential temperature with height, it is sufficient to use the reference profile. Figure 15 shows the reference potential temperature (θ_{ref}) points between the heights of 20 km and 25 km with a line of best fit added. The gradient of this line was calculated and used in equation 23 along with the value from a central point over this range θ_z = 507 K. This gives a value of $N = 2.52\times10^{-2} \pm 2.59\times10^{-5} s^{-1}$. The error was calculated by taking the gradient with the point above and below and calculating the error and also by estimating an error in the value θ_z. The error in *N* was then calculated using the equation

$$\Delta N = \tfrac{1}{2} N^2 \left(\frac{\Delta\theta_z}{\theta_z} + \frac{\Delta\partial\bar{\theta}/\partial z}{\partial\bar{\theta}/\partial z} \right). \qquad 20)$$

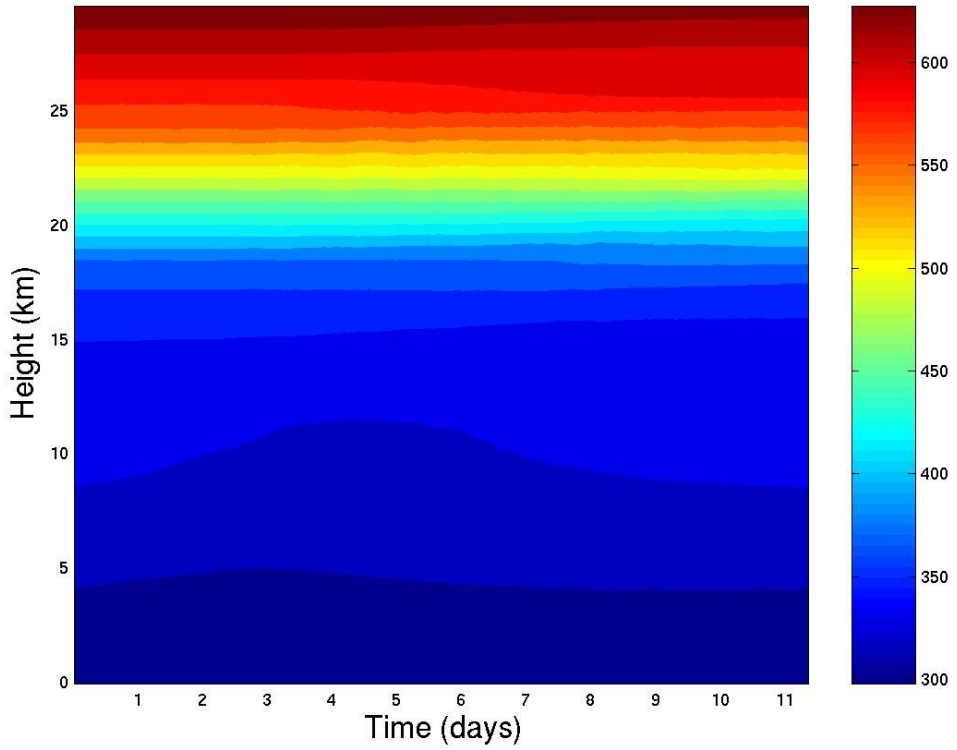

Figure 14 – *Actual potential temperature, θ_{tot} (K) with reference values added to perturbation values.*

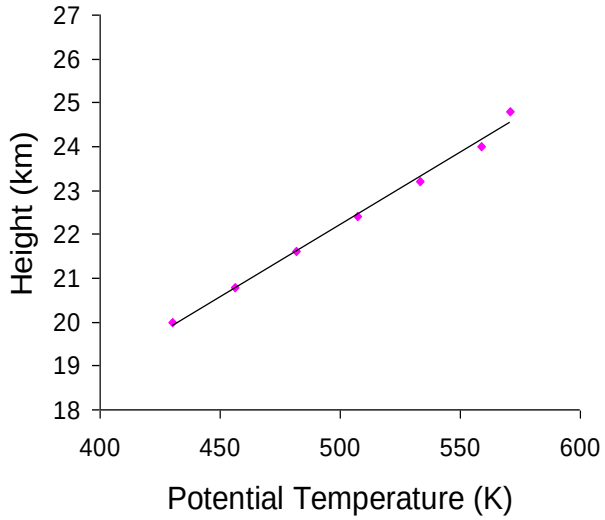

Figure 15 – *Reference potential temperature (θ_{ref}) with height between 20 and 25 km with best fit straight line added to calculate gradient***.**

6. Results

The general development of the model fields through the 11 day run will be presented and discussed here followed by an analysis of the waves in the stratosphere. Hovmöller plots of precipitation will be shown and an attempt made to connect the different large scale model fields to the waves visible in the rain rate data.

6.1 Development of Model Fields

The data from the 64 points around the equator were plotted as functions of distance along the equator and height and the results from days 5, 9 and 11 of zonal wind are shown in Figure 16. The initial zonal wind field was set to an easterly geostrophic wind of 5 ms^{-1} and over the first few days this starts to show perturbations from this starting value. After 5 days it can be seen that most of the flow is still easterly with just a few patches of westerly flow and there is no real organisation to the pattern. By day nine there is a lot more organisation visible and it would appear that a jet has set itself up between the heights of 10 km and 15 km. Still the flow is mainly easterly with some patches of strong westerly flow in the lower stratosphere. The lines of constant *u* slope westwards with height in the troposphere and eastwards with height in the stratosphere. This shows a baroclinic structure to the atmosphere which is confirmed in the *v* field analysis. The tropics are known to have both barotropic and baroclinic structures but since the data comes only from one latitude it is not possible to see if the model shows a barotropic nature as well. The winds above 26 km reduce to zero, the effect of the 4 km deep damping layer at this level. This layer is visible in both the *u* and *v* field plots (Figure 16 and Figure 17).

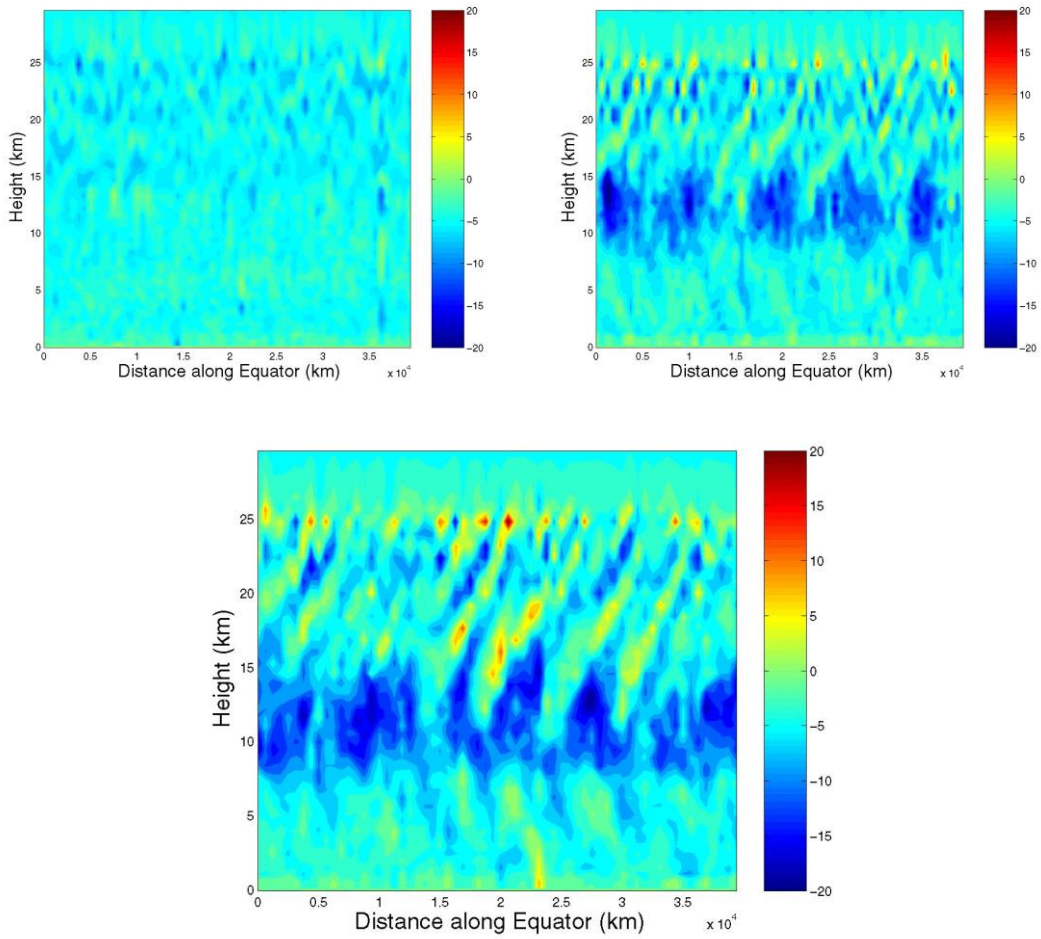

Figure 16 – *Plots of zonal wind as a function of zonal distance and height at 3 different days in the model run, a) 5, b) 9 and c) 11. The scale is goes from -20 ms^{-1} (blue) to 20 ms^{-1} (red).*

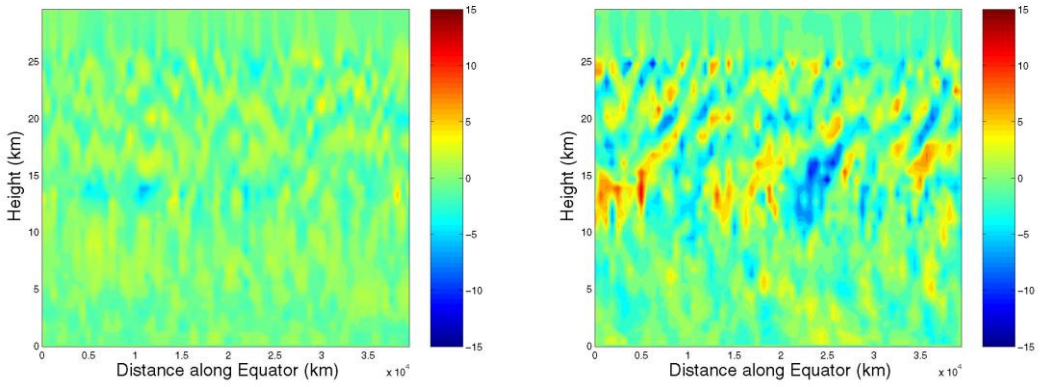

Figure 17 – *Plots of meridional wind as a function of zonal distance and height at 2 different days in the model run, a) 6 and b) 11. The scale goes from -15 ms^{-1} (blue) to 15 ms^{-1} (red)*

The plots of *v* (Figure 17) show a similar development with the initial value being zero everywhere. This field, however, seems to take longer to become patterned in the same way as the *u* field. It does show the same structure in the vertical with westward sloping lines at low altitudes and eastward sloping lines higher up. Again,

the strongest winds of around 13 ms^{-1} can be seen between 10 km and 15 km and also oscillating in the stratosphere.

The phase plots for *v* (e.g. Figure 8) show constant phase lines sloping backwards with height in the stratosphere where most of the analysis has been performed but there are also lines visible sloping forwards in the troposphere. The backwards sloping lines mean that energy is propagating upwards and the forward-sloping lines mean downward propagation of the same. This would suggest that there is an energy source at a height of around 13 km. Looking at the plots of the *u* and *v* fields it is possible to see the strongest winds occur at this height and this could be the source of the energy. However, it would be very interesting to investigate how much the convection in the model forces these waves as this height is presumably around the top of the deep convection. Much of the reviewed literature suggests that convection does provide a significant amount of energy to the upper troposphere through the latent heat released; energy which is then carried into the stratosphere by the vertically propagating waves.

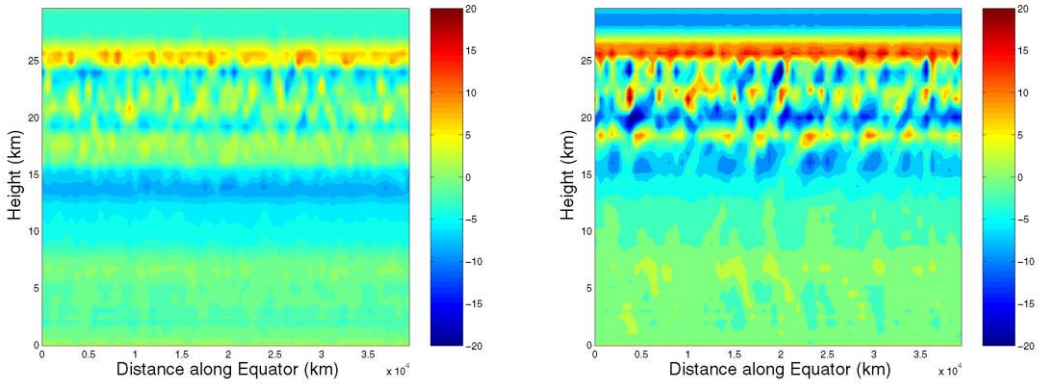

Figure 18 – *Plots of potential temperature perturbation, θ', as a function of zonal distance and height at days 6 and 11 of the model run. The scale goes from -20 K (blue) to 20 K (red).*

The evolution of the potential temperature perturbation shows a different sort of pattern to the wind profiles. It would appear that the potential temperature is trying to adjust from an initial reference state that was not quite right. There is cooling in the troposphere and general warming high up in the stratosphere. This can be seen clearly in Figure 18. There is not really any hint of a wave-like disturbance in the troposphere but above 18 km there is some degree of oscillation.

6.2 Comparison with Theory

In section 2 different theories for the organisation of convection were presented and in this section a comparison of the data from this model with those theories will be attempted.

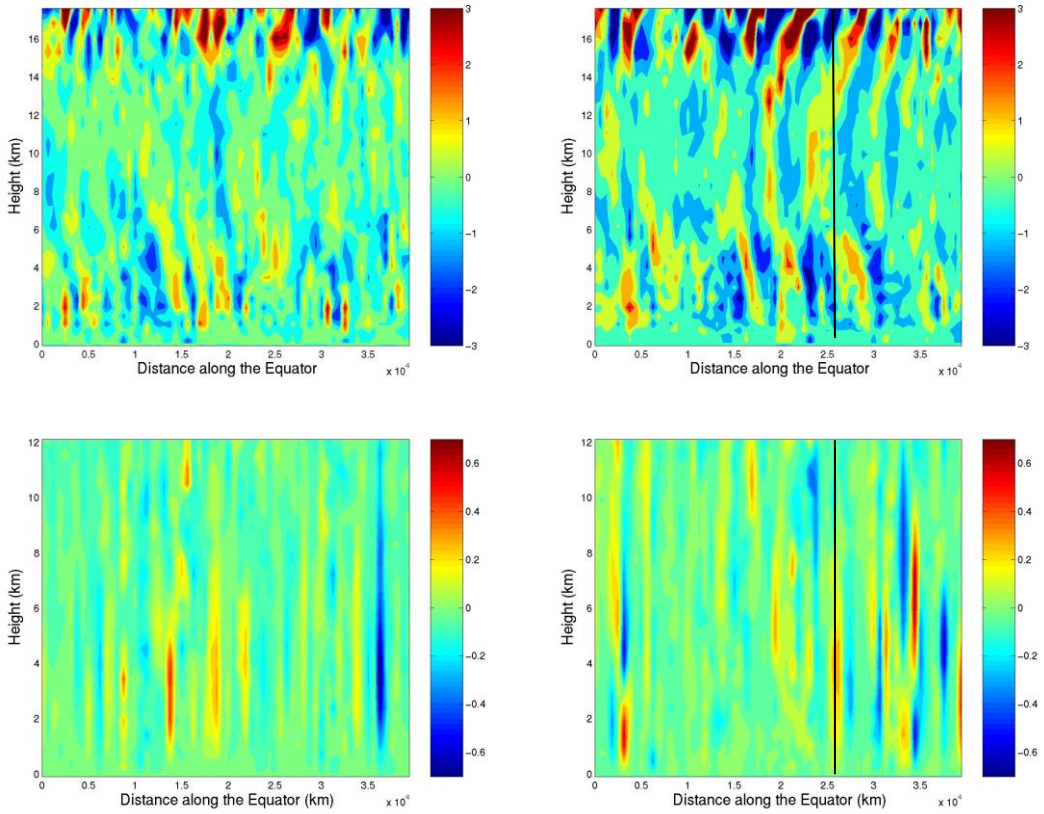

Figure 19 – *Plots of theta (top) and vertical velocity (bottom) on days 9 (left) and 11 (right) up to a height of 12km only. The scale of the theta plot is from -2 K to 2 K (blue to red) and the scale of the w plots is -0.7 ms^{-1} to 0.7 ms^{-1} (blue to red). The black line represents a region of strong vertical motion.*

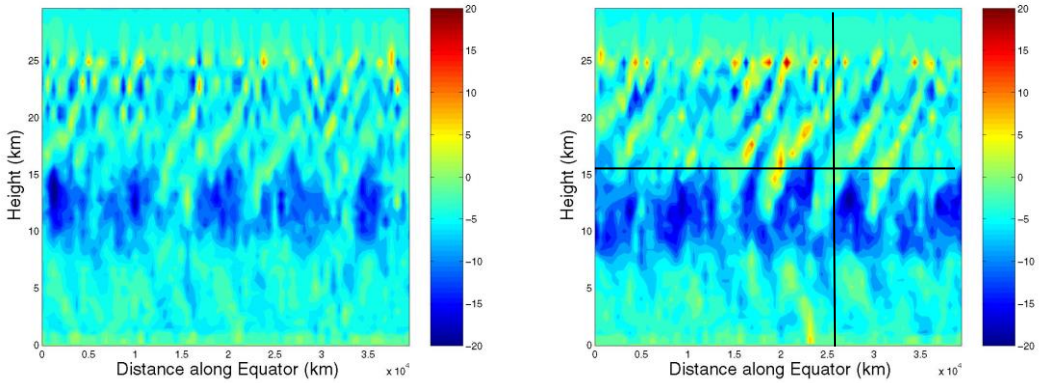

Figure 20 – *Zonal wind with height on days 9 and 11. Scale goes from -20 ms^{-1} to 20 ms^{-1}. The added vertical black line shows the position of the strongest vertical motion and the horizontal black line corresponds to the height at which the strongest westerly perturbations occur in Figure 21.*

Figure 19 shows a deviation from the average potential temperature perturbation up to a height of 17 km, calculated as

$$\theta'' = \overline{\theta'} - \theta' ,$$

where $\overline{\theta'}$ is the potential temperature perturbation averaged over all points in the zonal direction, and the vertical velocity up to a height of 12 km.

Tulich and Randall (2003) found that the maximum convection takes place in a region where there was a cold anomaly in the lower and upper troposphere and a warm anomaly in the middle troposphere. It would appear that this is indeed the case at the position indicated by the black line in Figure 19 where there is a cold anomaly near the surface, a warm anomaly in the mid-troposphere and a cold anomaly above 15 km. Between 2 and 6 km the line of maximum vertical velocity is in between a warm and cold anomaly in the same structure as that for the WISHE mechanism shown in Figure 1.

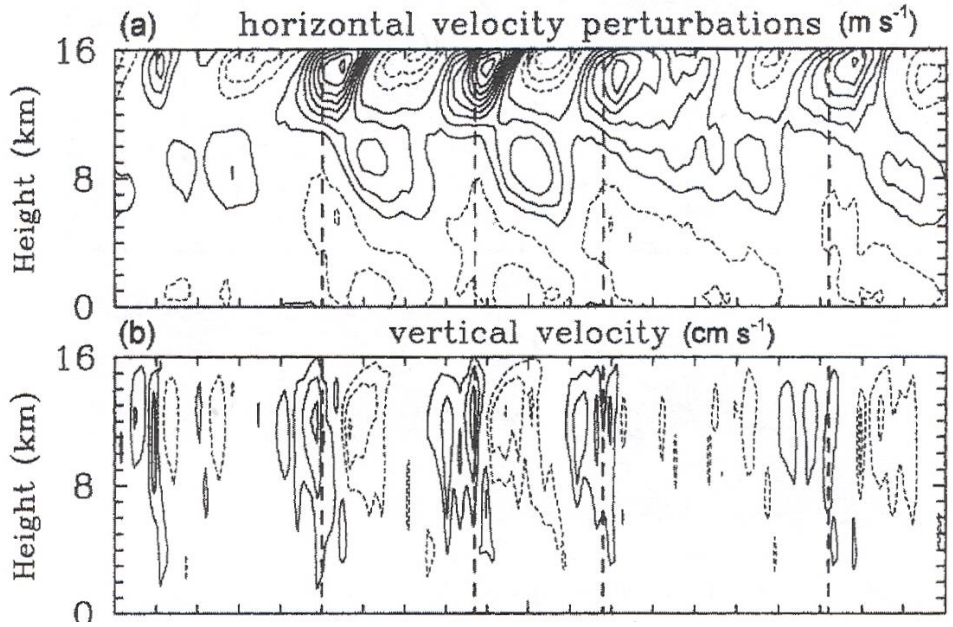

Figure 21 – *Plots of horizontal velocity perturbations and vertical velocity taken from Grabowski and Moncrieff (2001) showing the relation between the maximum vertical velocity and zonal wind.*

The two dimensional modelling study performed by Grabowski and Moncrieff (2001) produced very similar results in comparison with the structure of the zonal wind and the vertical velocity. Figure 21 shows these results from Grabowski and Moncrieff (2001) where the vertical dashed lines represent the position of the maximum vertical velocity just west of the maximum westerly zonal wind perturbations. Figure 20

shows the same sort of feature with the maximum vertical velocity occurring just west of the westerly flow in the upper tropospheric winds at about 15 km (shown by the intersection of the two black lines). Grabowski and Moncrieff (2001), using mass transport theory, deduced that the convection was the cause of the westerly perturbations rather than the other way around. The momentum flux defined in Moncrieff (1992) has the opposite sign to the direction of the travelling convective systems. This means that the convection carries westerly momentum upwards and deposits it at the top of the cloud layer (at about 15 km) producing westerly zonal wind perturbations.

6.3 Stratospheric Waves

6.3.1 Zonal Wavenumber 1

Since a lot of the literature reviewed showed the theoretical structure for a zonal wavenumber 1 disturbance (wavelength 40,000 km), this was the first wave to be analysed. Figure 22 shows the phase plots for *u* and *v*. The considerable difference in appearance between the two plots will be discussed in section 6.3.3. The results of the dispersion relation calculations for *u* and *v* are shown graphically in Figure 23. This plot shows that the waves that may be present at this wavelength are high order (large *n*) gravity waves. The phase speeds calculated for such wavelengths and periods are shown in Table 3 and it can be seen that these are very high speeds indeed - much larger than those found in Shutts (2006). However, in that study there was only a tenth of the horizontal domain therefore a tenth of the distance to travel in the measured period.

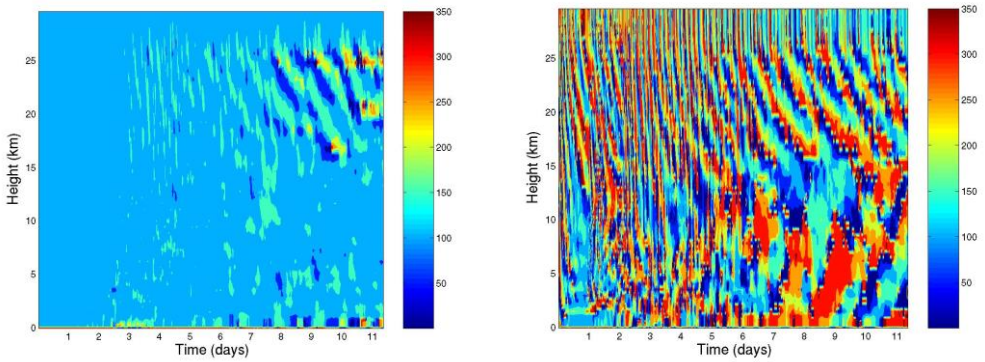

Figure 22 – *Phase plot for wavenumber 1 in u (left) and v (right)*

The only observed zonal wavenumber 1 disturbance is the MJO which has a period between 30 and 50 days (giving a phase speed of around 12 ms^{-1}) so it would not be possible to see that kind of disturbance in this limited time model run.

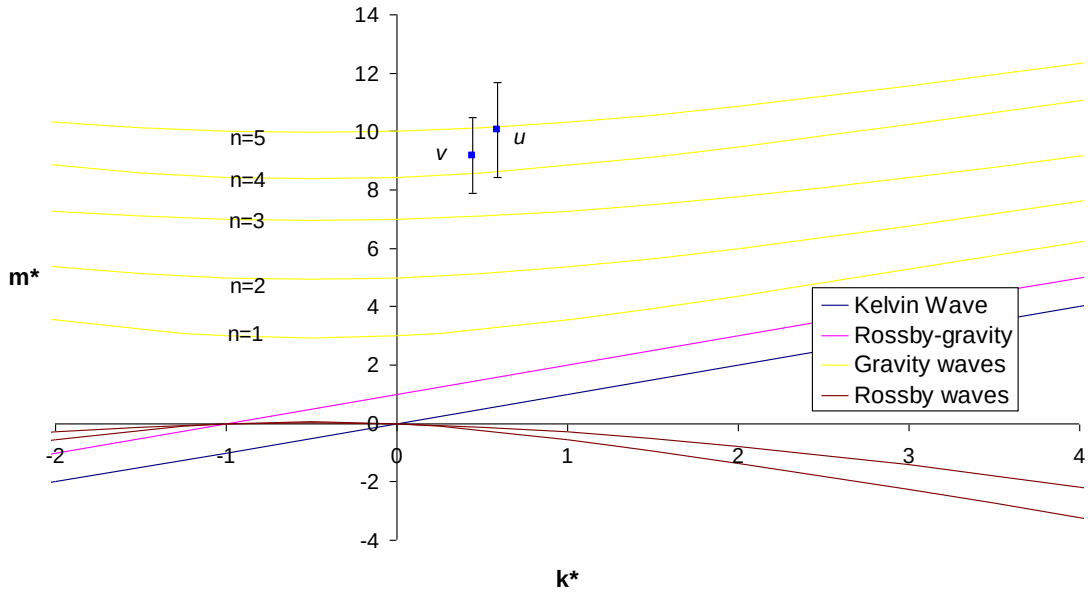

Figure 23 – *Dispersion curves with points plotted for wavenumber 1 in u and v (labelled).*

Table 3 – *Measured period and vertical wavelength (h) and calculated values for wavenumber 1 in u and v.*

Field	Period	Wavelength (km)	*h* (km)	*k**	*m**	Phase speed (m/s)
u	72576	40000	8.092	0.59	10.04	551.15
v	96033.6	40000	5.055	0.447	9.180	416.52

From the theory and observations presented in sections 3 and 4 it was shown that for even *n*, *u* is zero at the equator and for odd *n*, *v* is zero. Because of this we can say that the wave in *u* is an $n = 5$ gravity wave and that in *v* is an $n = 4$ gravity wave even though the error bars indicate that they could both be either $n = 4$ or 5. This is further confirmed by the point for *u* in Figure 23 being closer to the $n = 5$ curve and *v* closer to the $n = 4$ curve.

6.3.2 Higher wavenumbers in the *u* field

The same analysis was performed for higher wavenumbers (i.e. shorter zonal wavelengths) of between 2 and 20. Not all of the plots exhibited clear phase structures which could indicate a large amount of interference between different waves or might be a remnant of the long spin-up time of the model. The results for a selection of the most significant structures are shown in Figure 24.

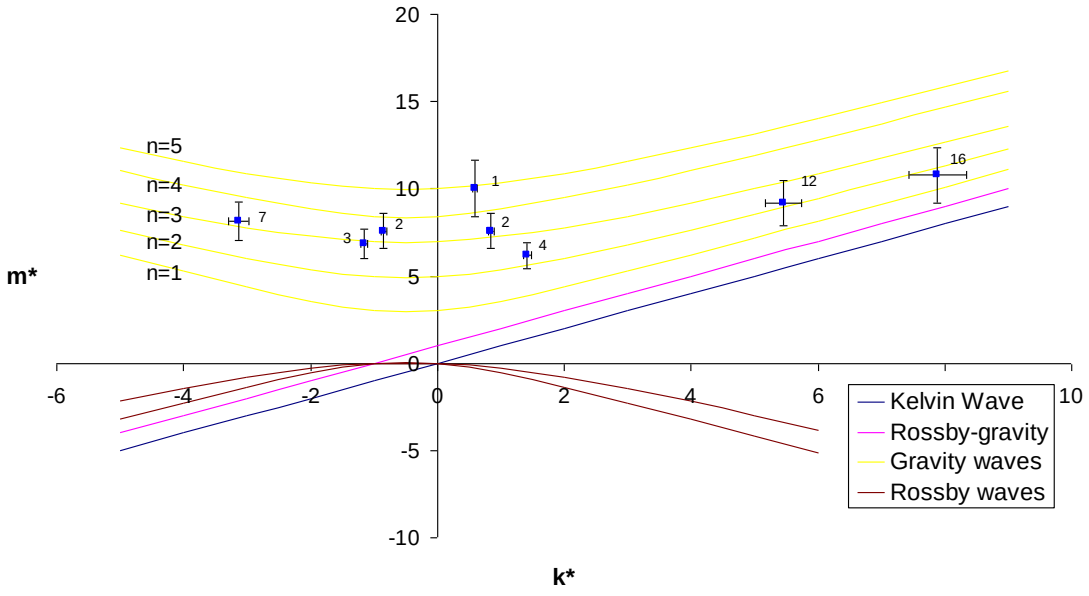

Figure 24 – *Dispersion curves with points plotted for various wavenumbers (labelled) in u.*

It would appear from the distribution of the points on the dispersion curves that as the wavenumbers increase, the waves move lower down the meridional structure order, i.e. *n* decreases. From the wave theory it is expected that the waves in *u* will have odd *n* and it can be seen that most of the points on the plot in Figure 24 are, within the error bounds, lying on the curves of odd *n* waves. Wavenumbers 2, 3 and 7 lie very close to the $n = 3$ gravity wave curve while the higher wavenumbers, 12 and 16 lie closer to the $n = 2$ curve but wavenumber 12 could be on the $n = 3$ curve and wavenumber 16 on the $n = 1$ curve within the estimated errors.

6.3.3 Higher wavenumbers in the *v* field

The results looking at the *v* field are considerably different to the *u* field. It is possible to see an evolution over time of the waves so that the constant phase isopleths at day 8 are distinctly more vertically aligned than at day 10, say. This shows the waves slowing down. Where this is visible more than one wave for each wavenumber has been analysed to investigate what is happening to the wave structures as the model runs.

The phase plot for wavenumber 2 is shown since this has the most interesting structure with 3 possible orientations of constant phase lines fitting the data (Figure 25).

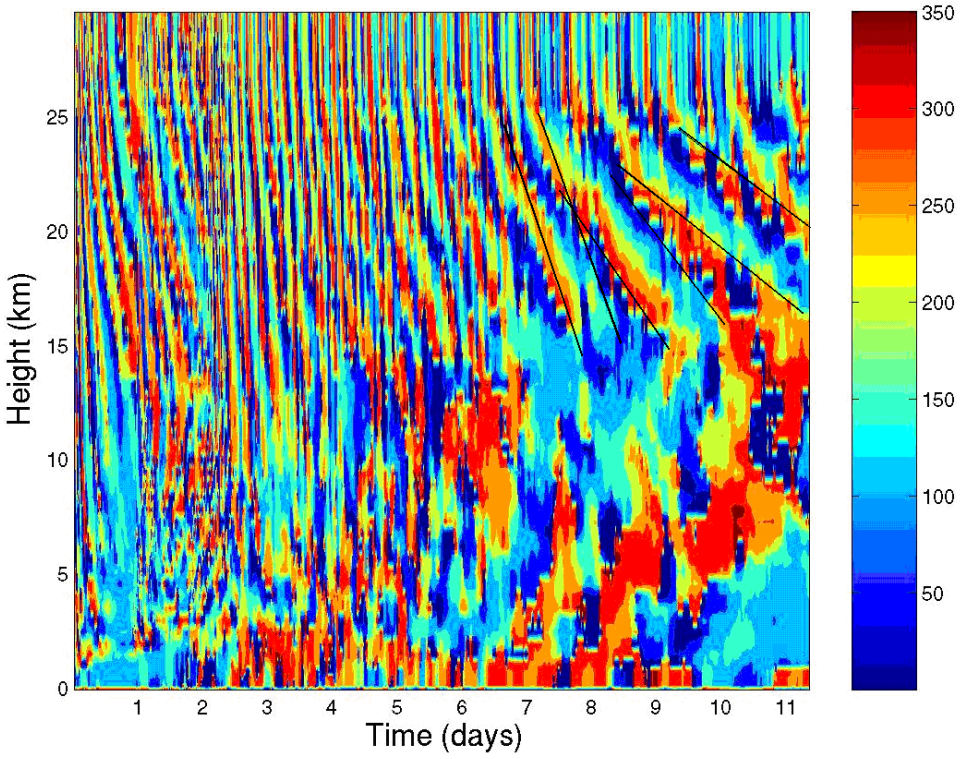

Figure 25 – *Phase plot for wavenumber 2 in v. The 3 pairs of parallel lines show the 3 possible orientations of the waves.*

Table 4 – *Measured period and vertical wavelength and calculated values for wavenumber 2 in v.*

Time (day in the model run)	Period (hours)	*h* (km)	*k**	*m**
8	16.848	6.066	1.415	19.178
9	30.888	6.74	0.772	5.135
10-11	42.12	4.381	0.566	4.249

In the case of wavenumber 2 the plot shows quite clearly a decreasing phase with time therefore westward propagation. In other plots, however, it is not quite as easy to interpret. It is quite possible that there are both eastward and westward moving components of the same wavenumber.

The changing shape of the wave structures shows an increase in period over time. This gives decreasing values of both k^* and m^* (Table 4) so the points on the dispersion curve plot get closer to the axes as can be seen in Figure 26.

One of the effects of rotation on fluid motion is a tendency to produce larger, simpler structures where small-scale motions such as turbulent eddies get absorbed into the larger scale motions. Perhaps this is one of the reasons for the apparent simplification over time of the wave structures.

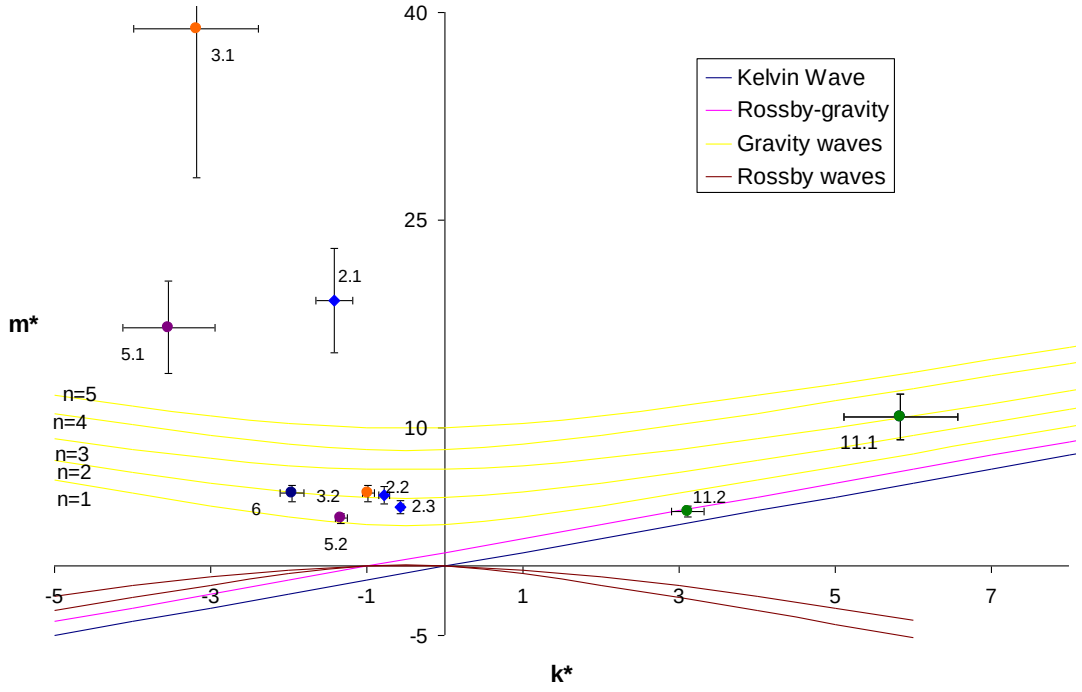

Figure 26 - *Dispersion curves with points plotted for various wavenumbers (labelled) in v. The labels show the wavenumber and whether the measured wave was the 1st, 2nd or 3rd in time (e.g. 2.1 is wavenumber 2 and the first measured wave).*

A brief comparison of the waves found for the fields of *u* and *v* shows some agreement in wave types between the two fields (see Table 5). For instance, wavenumber 2 shows both westward and eastward propagation for both fields. A direct comparison cannot be made between all of the waves as each wave did not show up with the same clarity in both fields. All of the wave periods in the *v* field are longer than in the *u* field. The vertical wavelengths measured here are all less than the theoretical values found in Wheeler et al (2000) of 6 to 8 km.

Table 5 – *A summary of the types of waves found for the u and v fields. In the cases where more than one wave type was found for the same wavenumber, the wave at the latest time in the model run is listed.*

Field	Wavenumber	Period (days)	*h* (km)	Direction of Propagation	Type of Wave
v	2	1.755	4.318	Westward and Eastward	*n = 2* gravity wave
v	3	1.521	4.718	Westward	*n = 2* gravity wave
v	5	1.872	4.718	Westward	*n = 1* gravity wave
v	6	1.521	4.718	Westward	*n = 2* gravity wave
v	11	1.755	4.718	Eastward	mixed Rossby-gravity
u	2	1.176	5.476	Westward and Eastward	*n = 3* gravity wave
u	3	1.287	5.055	Westward	*n = 3* gravity wave
u	4	1.4	4.72	Eastward	*n = 2* gravity wave
u	7	1.1115	5.72	Westward	*n = 3* gravity wave
u	12	1.092	5.236	Westward and Eastward	*n = 2* gravity wave
u	16	1.008	5.236	Westward and Eastward	*n = 1* gravity wave

The differences between the phase plots in the *u* and *v* fields are large (although they give similar results in the types of waves present). It can be seen in Figure 22 that the waves in *v* evolve over the model run whereas the waves in *u* get stronger but stay at the same speed and size. This indicates that perhaps there are different mechanisms producing the waves in the two fields. There is also a significant difference in the troposphere with there being almost no signal in *u* and a very strong evolving signal in *v*. Looking at Figure 25 it can be seen that in the troposphere there is nothing significant happening in the first 3 days below 12 km and then a forward sloping structure starts to form. This is about the same time that convection begins. From this time onwards there is a pattern of slowing and growing in the waves in the stratosphere. This suggests that there is a feedback between the waves in the meridional wind and the convection.

6.4 Potential Temperature

As was seen in section 6.1 the potential temperature perturbation shows a different structure to that of the wind fields. When the Fourier analysis was carried out on this field it produced phase plots which were all very similar to that shown in Figure 27. The streak of high phase just above 25 km could be a vestige of the spin up from the initial reference profile of potential temperature. It is possible, however, to see distinct constant phase lines sloping backwards with height between 20 km and 24 km. Figure 27 shows the same sort of time evolution as the *v* field plots.

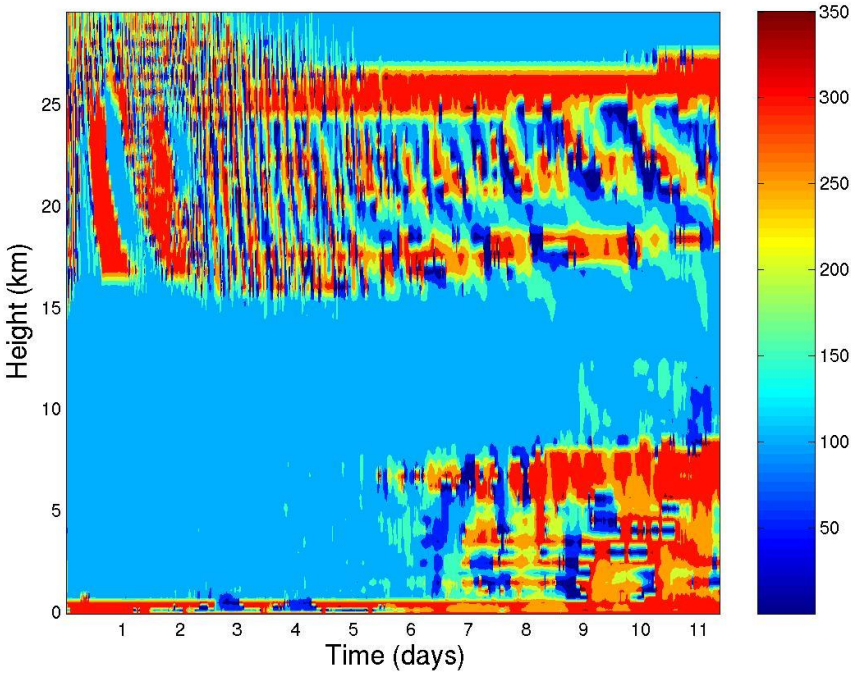

Figure 27 – *Phase plot for wavenumber 2 in* θ'.

Comparing the phase plots produced for this model with those produced in Shutts (2006) (shown in Figure 28) it is clear to see that something must be significantly different in the structure of the potential temperature field between these two models. The results from Shutts (2006) show an excellent example of the "boomerang" structure described in Wheeler et al (2000) and explained in section 4.2.

Due to the difficulty in picking out the lines of constant phase in the potential temperature field it was decided that this field would not be used in the analysis of the wave structures.

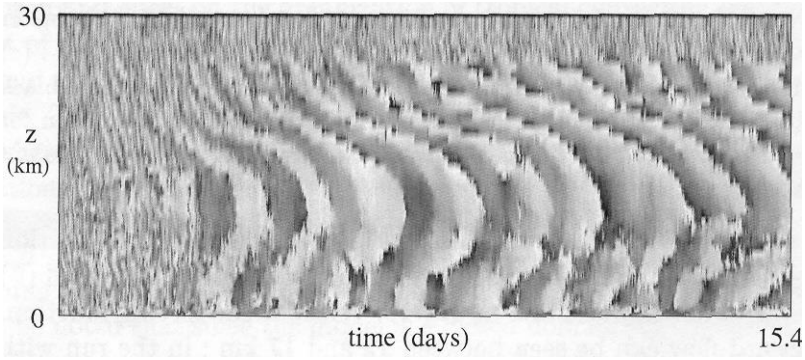

Figure 28 – *Phase plot for wavenumber 2 in* θ' *from Shutts (2006).*

Had there been more time it might have been interesting to use the value θ'' calculated in section 6.2 to produce the phase plots as this might have shown a clearer pattern with an easier structure to analyse.

6.5 Tropospheric Waves

The zonal wind field with height after 9 days in the model run which can be seen in Figure 29 shows an interesting pattern at a height of between 10 km and 15 km. This is where the strongest easterly winds occur and there appears to be an oscillation of the strength of this wind with a wavelength of approximately 8,000 km giving 5 waves around the 40,000 km circumference.

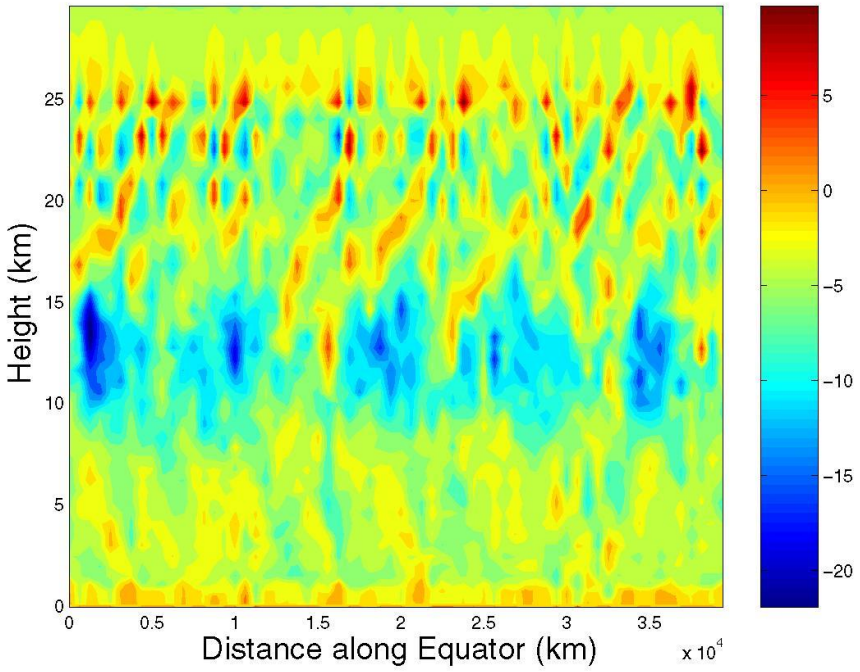

Figure 29 – *The zonal wind (u) with height after 9 days of the model run. The wind speed varies from 22ms^{-1} westwards (blue) to 10m/s eastwards (red).*

In order to investigate these waves the spectral analysis was performed for wavenumber 5 and the results for the amplitude can be seen in Figure 30. This shows clearly that there is a strong signal for this mode at the required height. However, looking at the phase diagram (Figure 31) it is possible to see from the very slight change in phase angle at this height that this oscillation is quasi-stationary. The phase moves gradually between 100 and 150 degrees. This means that this oscillation has no eastward (or westward) phase speed. This type of standing wave has not generally been observed in the literature reviewed.

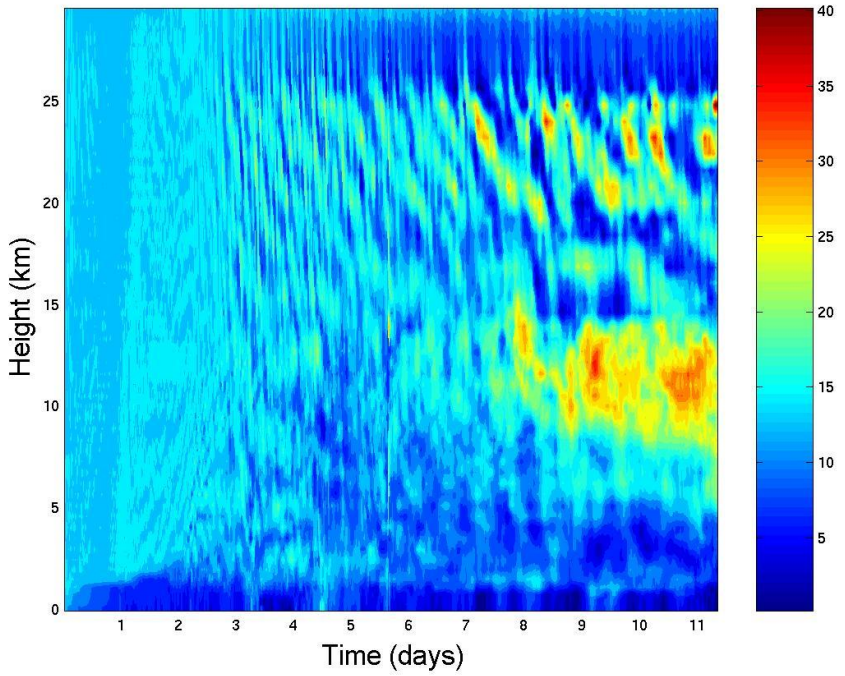

Figure 30 – *Amplitude of signal for wavenumber 5 in u. Scale is from 0 to 40 ms^{-1} (blue to red).*

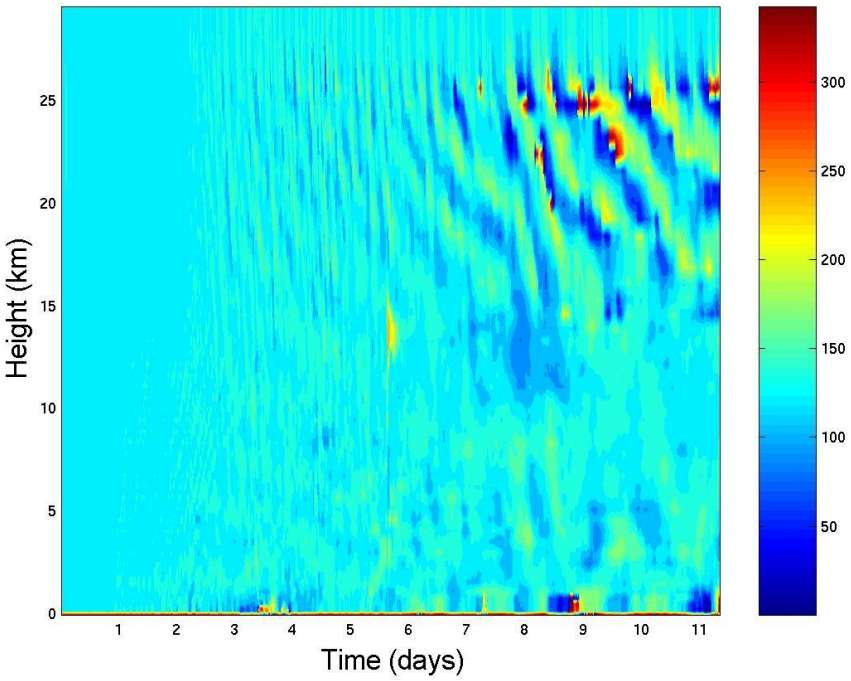

Figure 31 – *Phase of signal for wavenumber 5 in u.*

6.6 Precipitation

The precipitation rate at each grid point along the equator was plotted as a Hovmöller diagram in order to study the structural evolution and organisation of the deep tropical convection. Due to the massive number of points (over 16 million) at which this data was gathered (16,384 grid points by 999 time steps) it was not possible to plot all the data on one diagram. They were, instead, split into 8 sections of equal length and plotted separately. All 8 Hovmöllers are shown in Appendix D.

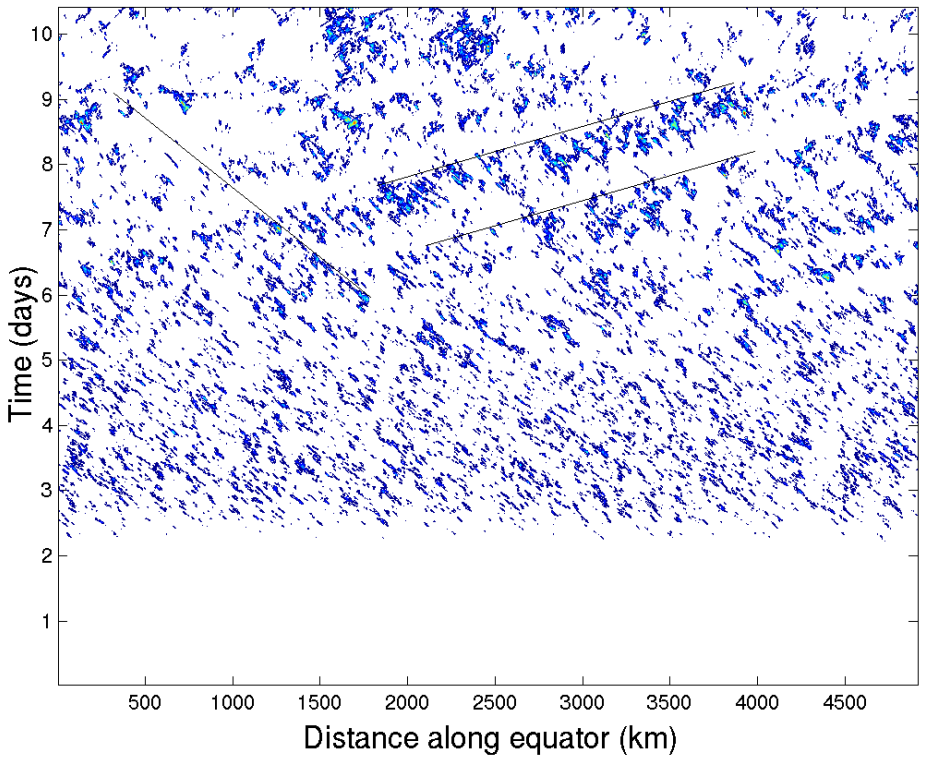

Figure 32 – *Hovmöller diagram of rainfall from 0 to 5000 km along the equator over 10. 4 days. The parallel black lines represent an eastward propagating wave of phase speed 13 ms^{-1}. The backward sloping black line shows easterly phase speed of 5.7 ms^{-1}.*

It can be seen in Figure 32 that over the first two and a half days there is no rainfall at all, probably due to the fact that the model was initialised with no water vapour. After that, rain bands form at seemingly random intervals but with a clear westward movement in small packets. By day 7 the small clusters have organised together to form larger clusters of convection which are moving eastwards. Towards the end of the model run the precipitation looks like it is disorganising but it is possible that it

has started to organise into even larger structures. Without more data from a longer run of the model it is not possible to say what is happening at that stage.

The single backward sloping line added to Figure 32 represents the movement of the individual small clusters and it might be expected that the phase speed for this line would be approximately equal to the tropospheric wind speed as individual clouds are carried along by the large scale flow. It was not possible to use the same Fourier analysis technique to analyse the precipitation data as this would have involved lengthy coding for which there was not enough time. Instead, using the same method as for the phase plots, the time taken for the cluster to move a certain distance was measured and the phase speed calculated. This turns out to be 5.713 ms^{-1} which is close to the imposed geostrophic wind of 5 ms^{-1}. This implies that the small clusters of convection are being moved along by the ambient zonal wind as expected.

The parallel lines are drawn subjectively along the edge of the larger clusters of rainfall. The wavelength and period were calculated in the same way and it was found that this wave has a horizontal wavelength of 1,562 km and period of 27.3 hours. This gives a phase speed of 15.9 ms^{-1} and a zonal wavenumber of between 25 and 26. These large clusters are known as superclusters and are large-scale envelopes of smaller clusters of convection. Observations of such superclusters have shown they usually have an eastward phase speed of around 15 ms^{-1} and horizontal wavelength between 2000 and 3000 km (Majda et al 2004). The clusters visible in this simulation agree very well in phase speed but are slightly smaller in horizontal extent.

With such a high zonal wavenumber it is difficult to analyse the dynamical fields definitively to confirm the existence of such a wave since there are only 64 points at which the data are available. However, it is interesting to see whether there is any suggestion of this type of wave either in *u* or *v*.

The phase plots for *v* can be seen in Appendix B but the plots for *u* are shown here in Figure 33. They show lines of constant phase with a much gentler slope than previous wavenumbers studied. These wave structures have a longer period than the smaller wavenumbers.

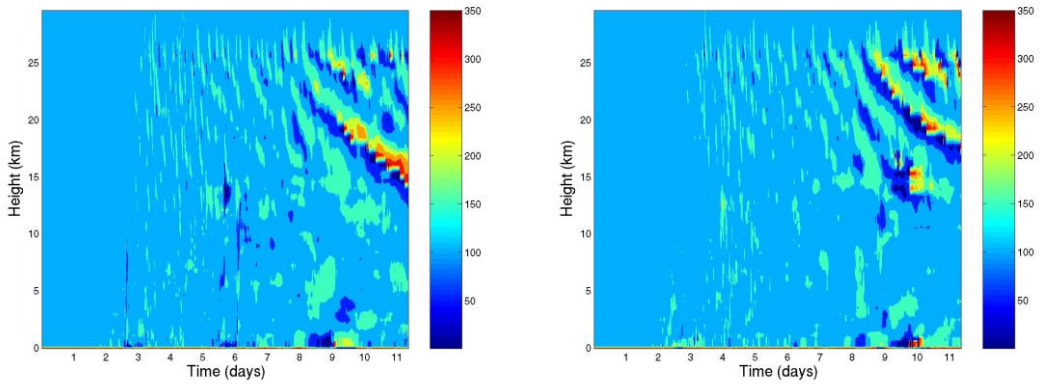

Figure 33 – *Phase plots for u with wavenumbers 25 (left) and 26 (right).*

The phase speed of the wavenumber 25 disturbance in the *v* field (Table 6) shows a good match with the phase speed of the eastward propagating superclusters of precipitation which was found to be 15.9ms^{-1}.

Table 6 – *Summary for wavenumbers 25 and 26 in the u and v field.*

Field	Wavenumber	Period (days)	Vertical Wavelength (km)	Phase Speed (ms^{-1})
u	25	1.7534	4.546	10.56
u	26	1.2752	4.546	13.96
v	25	1.1955	4.3187	15.49
v	26	1.1955	4.546	14.89

Plotting the values of *m** and *k** for wavenumbers 25 and 26 in the *v* field shows that within the error bars wavenumber 25 has the properties of a Kelvin wave (Figure 34). It is important to note in Figure 34 that all of the other dispersion curves lie above the Kelvin wave curve therefore there is not any closer curve that would be an alternative in this case.

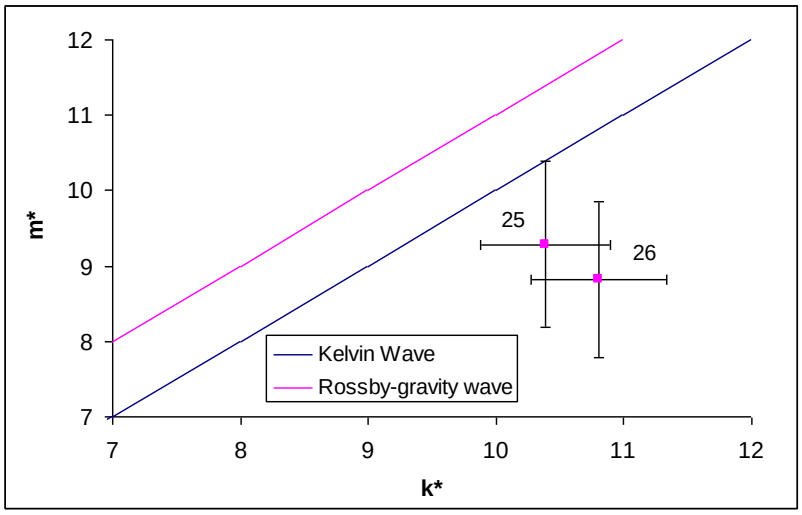

Figure 34 – *Kelvin wave dispersion curve with wavenumber 25 and 26 in the v field.*

It is possible that the errors have been underestimated in this case due to the difficulty in judging the edges of the superclusters since in the *v* field it would be expected that the wave would resemble a mixed Rossby-gravity wave as this has even *n.* The Kelvin wave has *n* equal to -1, so this type of wave is expected in the *u* field. Due to the limited number of points along the equator, such large waves are difficult to confirm with the same certainty of the smaller waves so perhaps the errors in this case should have been larger.

7. Conclusions

Convection in the tropical atmosphere is a major issue in atmospheric science at present as there is no single theory that can explain the complex motions that occur there. Many proposed mechanisms for the organisation of convection from the small clusters up to the largest scale global wave disturbances have been presented here. A large proportion of the disturbances in the tropics have been shown to be well represented by the linear wave theory put forward by Matsuno (1966) and Lindzen (1967) and a systematic analysis of these types of disturbances has begun (e.g. Roundy and Frank 2004, Wheeler and Kiladis 1999).

In order to investigate some of these types of disturbances, the data from a cloud resolving model which spans the circumference of the Earth were used. Fourier analysis was performed on the fields of zonal and meridional wind and it was found that there are indeed many different waves present. In the meridional wind field the wave structures seemed to be moving closer over the course of the model run to those that have been frequently observed (e.g. the Kelvin wave or mixed Rossby-gravity wave). However, without a longer model run it is not possible to say what structure these waves will eventually take.

It was found that the precipitation in the model organised itself into small clusters moving westwards with the ambient zonal wind enveloped in a larger supercluster with horizontal wavelength around 1500 km and eastward phase speed of 15.9 ms^{-1}. This seemed to be coupled to a disturbance in the meridional wind which (within the bounds of the errors) appears to be a Kelvin wave (but is more likely a mixed Rossby-gravity wave). After 10 days however, these structures seemed to start breaking down (or reorganising into even larger structures) but again without a longer model run it is not possible to say what these are. It would also have been beneficial to have more data points along the equator in order to better resolve the larger zonal wavenumber disturbances.

The data used in this project, apart from the precipitation data, were only from points along the equator. In order to investigate more fully what types of waves are present it would have been very interesting to look at the data from off the equator since the

meridional structure of the waves are more distinctive than the structure on the equator.

There were many uncertainties involved in the method and tools used in this study, for instance, the subjective nature of the positioning of the constant phase isopleths and the edges of the superclusters of convection. Also, the difficulty in the choice of direction of propagation of the waves, particularly in the *v* field, suggests that perhaps a better method of wave analysis could have been used. The spectral analysis methods used by WK and Yang et al (2003) which are similar to those developed by Hayashi (1982) separate eastward and westward moving waves then the data can be filtered using FFT (Yang et al 2003).

Cloud resolving models like the one studied here are an excellent way to analyse wave features in the tropical atmosphere as they provide a full dataset including winds, temperatures and precipitation rates, from equally spaced points around the globe. Observational analyses, on the other hand, use proxies for precipitation such as outgoing longwave radiation and precipitable water data taken from satellites and may not have such a uniform distribution of data points. Although it is imperative that observational studies carry on, the modelling approach can provide valuable information allowing the improvement of cloud parameterisations in GCMs and the opportunity to improve the predictability of weather in the tropics.

Performing experiments with models such as this can glean information on what the most important mechanisms are in the organisation of convection and the large-scale waves. It would have been very interesting to do different runs of this model with the trade wind forcing function or the radiation scheme switched on and even with orography included to investigate the effect of land-sea contrasts on the development of equatorial waves.

8. References

ALEXANDER, M. J., J. H. BERES and L. PFISTER, 2000: Tropical stratospheric gravity wave activity and relationships to clouds, *J. Geophys. Res.*, **105**, 22,299-22,309.

ALEXANDER, M. J., J. R. HOLTON, and D. R. DURRAN, 1995: The gravity wave response above deep convection in a squall line simulation, *J. Atmos. Sci*., **52**, 2212-2226.

ANDREWS, D. G., J. R. HOLTON, and C. B. LEOVY, 1987: *Middle-Atmosphere Dynamics*. Volume 40 in the International Geophysics Series, Academic Press.

ARAKAWA, A., 2004: The cumulus parameterization problem: past, present and future, *J. Clim*., **17**, 2493-2525

ARAKAWA, A. and W. H. SCHUBERT, 1974: The interaction of a cumulus cloud ensemble with the large-scale environment, Part I., *J. Atmos. Sci*., **31**, 674-701.

BLOOMFIELD, P., 1976: *Fourier Analysis of Time Series: An Introduction.* John Wiley and Sons, New York, 258pp.

BRETHERTON, C. S., and P. N. BLOSSEY, 2005: An energy-balance analysis of deep convective self-aggregation above uniform SST, *J. Atmos. Sci*., **62**, 4273-4292.

BRYAN, G. H., J. C. WYNGAARD, and J. M. FRITSCH, 2003: Resolution requirements for the simulation of deep moist convection, *Mon. Wea. Rev*., **131**, 2394-2416.

BYERS, H. R. and R. R. BRAHAM, 1949: *The Thunderstorm*. U.S. Gov't Printing Office, Washington DC, 287 pp. [NTIS PB-234-515.]

CARBONE, R. E., 1982: A severe frontal rainband. Part I: Stormwide hydrodynamic structure, *J. Atmos. Sci*., **39**, 258-279.

CHANG, C. P., 1970: Westward propagating cloud patterns in the tropical Pacific as seen from time composite satellite photographs, *J. Atmos. Sci*., **27**, 133-138.

CHARNEY, J. G. and A. ELIASSEN, 1964: On the growth of the hurricane depression, *J. Atmos. Sci.,* **21,** 69-75.

COHEN, B. G., and G. C. CRAIG, 2004: The response time of a convective cloud ensemble to a change in forcing, *Q. J. R. Meteorol. Soc*., **130**, 933-944.

EMANUEL, K.A., 1987: An air-sea interaction theory of intraseasonal oscillations in the tropics, *J. Atmos. Sci*., **44**, 2324-2340.

EMANUEL, K.A., 1994: *Atmospheric Convection*. Oxford University Press, New York.

EMANUEL, K. A., J. D. NEELIN and C. S. BRETHERTON, 1994: On large-scale circulations in convecting atmospheres. *Q. J. R. Meteorol. Soc.* **120**, 1111-1143.

GILL, A. E., 1982: *Atmosphere-Ocean Dynamics*. Volume 30 in the International Geophysics Series. Academic Press.

GRABOWSKI, W. W. and M. W. MONCRIEFF, 2001: Large-scale organization of tropical convection in two-dimensional explicit numerical simulations. *Quart. J. Roy. Meteor. Soc.*, **127**, 445-468

HAERTEL, P. T. and G. N. KILADIS, 2004: Dynamics of 2-day equatorial waves, *J. Atmos. Sci.*, **61**, 2707-2721.

HAYASHI, Y., 1982: Space-time spectral analysis and its applications to atmospheric waves, *J. Meteor. Soc. Japan*, **60**, 156-171.

HOLTON, J. R., 1992: *An Introduction to Dynamic Meteorology*. Academic Press, 507 pp.

IPCC, 2001: *Climate change 2001: The scientific basis (Summary for policymakers.* A report of Working Group 1 of the Intergovernmental Panel on Climate Change).

KILADIS, G., N. and M. WHEELER, 1995: Horizontal and vertical structure of observed tropospheric equatorial Rossby waves, *J. Geophys. Res.*, **100**, 22,982-22,997.

KUANG, Z., P. N. BLOSSEY, and C. S. BRETHERTON, 2005: A new approach for 3D cloud-resolving simulations of large-scale atmospheric circulation, *Geophys. Res. Lett*., **32**, L02809.

LEMONE, M. A., and E. J. ZIPSER, 1980: Cumulonimbus vertical velocity events in GATE. Part I: Diameter, intensity, and mass flux, *J. Atmos. Sci*., **37**, 2444-2457.

LINDZEN, R. S., 1967: Planetary waves on beta planes, *Mon. Wea. Rev*., **95**, 441-451.

LINDZEN, R. S. and J. R. HOLTON, 1968: A theory of the quasi-biennial oscillation, *J. Atmos. Sci.*, **25**, 1095-1107.

LINDZEN, R. S., 1974: Wave-CISK in the tropics. *J. Atmos. Sci*., **31**, 156-179.

LINDZEN, R., S., 2003: The interaction of waves and convection in the tropics. *J. Atmos. Sci.*, **60**, 3009-3020.

LIU, C., and M. W. MONCRIEFF, 2004: Effects of convectively generated gravity waves and rotation on the organization of convection, *J. Atmos. Sci*, **61**, 2218-2227.

MADDEN, R. A., and P. R. JULIAN, 1971: Detection of a 40-50 day oscillation in the zonal wind in the tropical Pacific, *J. Atmos. Sci*., **28**, 702-708.

MAJDA, A. J., and B. KHOUIDER, 2004: A model for convectively coupled tropical waves: Nonlinearity, rotation, and comparison with observations, *J. Atmos. Sci.*, **61**, 2188-2205.

MAPES, B. E., 2004: Sensitivities of cumulus-ensemble rainfall in a cloud-resolving model with parameterized large-scale dynamics, *J. Atmos. Sci*., **61**, 2308-2317.

MATSUNO, T., 1966: Quasi-geostrophic motions in the equatorial area, *J. Meteor. Soc. Japan*, **44**, 25-43.

MONCRIEFF, M. W., 1992: Organized convective systems: Archetypal dynamical models, mass and momentum flux theory, and parametrization, *Q. J. R. Meteorol. Soc*., **118**, 819-850.

NEWTON, C. W., 1950: Structure and mechanism of the prefrontal squall line, *J. Meteor*., **7**, 210-222.

NEWTON, C. W., 1966: Circulations in large sheared cumulonimbus, *Tellus*, **18**, 699-713.

OOUCHI, K., 1999: Hierarchical organization of super cloud cluster caused by WISHE, convectively induced gravity waves and cold pool, *J. Meteorol. Soc. Japan*, **77**, 907-927.

OOYAMA, K., 1964: A dynamical model for the study of tropical cyclone development. *Geophys. Int*., **4**, 187-198.

OOYAMA, K., 1982: Conceptual evolution of the theory and modelling of the tropical cyclone, *J. Meteorol. Soc. Japan*, **60**, 369-379.

PANDYA, R. E. and M. J. ALEXANDER, 1999: Linear stratospheric gravity waves above convective thermal forcing, *J. Atmos. Sci*., **56,** 2434-2446.

PETCH, J. C., 2006: Sensitivity studies of developing convection in a cloud-resolving model, *Q. J. R. Meteorol. Soc*., **132**, 345-358.

RIEHL, H. and J. MALKUS, 1958: On the heat balance in the equatorial trough zone, *Geophysica,* **6**, 503-537.

ROTUNNO, R., J. B. KLEMP and M. L. WEISMAN, 1988: A theory for strong, long-lived squall lines, *J. Atmos. Sci,* **45**, 463-485.

ROUNDY, P. E. and W. M. FRANK, 2004: A climatology of waves in the equatorial region, *J. Atmos. Sci.*, **61**, 2105-2132.

SHUTTS, G., 2006: Upscale effects in simulations of tropical convection on an equatorial beta-plane, *Preprint submitted to Dyn. Atmos. Ocean Sci.*

SHUTTS, G., and T. N. PALMER, 2005: Statistical fluctuations in convective forcing computed from a cloud-resolving model and their relevance to the parametrization problem, *Preprint submitted to J. Clim*., 23pp.

STRAUB, K. H. and G. N. KILADIS, 2003: The observed structure of convectively coupled Kelvin waves: Comparison with simple models of coupled wave instability, *J. Atmos. Sci.,* **60**, 1655-1668.

TINDALL, J. C., J. THUBURN and E. J. HIGHWOOD, 2006: Equatorial waves in the lower stratosphere. I: A novel detection method, *Q. J. R. Meteorol. Soc.,* **132**, 177-194.

TINDALL, J. C., J. THUBURN and E. J. HIGHWOOD, 2006: Equatorial waves in the lower stratosphere. II: Annual and interannual variability, *Q. J. R. Meteorol. Soc*., **132**, 195-212.

TOMITA, H., H. MIURA, S. IGA, T. NASUNO, and M. SATOH, 2005: A global cloud-resolving simulation: Preliminary results from an aqua planet experiment, *Geophys. Res. Lett*., **32**, L08805.

TOMPKINS, A. M., 2001a: Organization of tropical convection in low vertical wind shears: The role of water vapour, *J. Atmos. Sci*., **58**, 529-545.

TOMPKINS, A. M., 2001b: Organization of tropical convection in low vertical wind shears: The role of cold pools, *J. Atmos. Sci.*, **58**, 1650-1672.

TOMPKINS, A. M. and G. C. CRAIG, 1998: Time-scales of adjustment to radiative-convective equilibrium in the tropical atmosphere, *Q. J. R. Meteorol. Soc*., **124**, 2693-2713.

TULICH, S. N. and D. A. RANDALL, 2003: Large-scale convectively coupled gravity waves in a two-dimensional cloud resolving model, submitted to *J. Atmos. Sci.*

WALLACE, J. M., and V. E. KOUSKY, 1968: Observational evidence of Kelvin waves in the tropical stratosphere, *J. Atmos. Sci*., **25,** 900-907.

WHEELER, M. and G. N. KILADIS, 1999: Convectively coupled equatorial waves: analysis of clouds and temperature in the wavenumber-frequency domain, *J. Atmos. Sci.,* **56**, 374-399.

WHEELER, M., G. N. KILADIS and P. J. WEBSTER, 2000: Large-scale dynamical fields associated with convectively coupled equatorial waves, *J. Atmos. Sci*., **57**, 613-640.

WILCOX, E. M. and V. RAMANATHAN, 2001: Scale dependence of the thermodynamic forcing of tropical monsoon clouds: Results from TRMM observations, *J. Clim*., **14**, 1511-1524.

YANAI, M., and T. MARUYAMA, 1966: Stratospheric wave disturbances propagating over the equatorial Pacific, *J. Meteor. Soc. Japan*, **44**, 291-294.

YANG, G. Y., B. HOSKINS and J. SLINGO, 2003: Convectively coupled equatorial waves: a new methodology for identifying wave structures in observational data, *J. Atmos. Sci*., **60**, 1637-1654.

YANO, J.-I. and K. A. EMANUEL, 1991: An Improved WISHE model of the equatorial atmosphere and its coupling with the stratosphere. *J. Atmos. Sci*., **48**, 377-389.

ZANGVIL, A., 1975: Temporal and spatial behavior of large-scale disturbances in tropical cloudiness deduced from satellite brightness data, *Mon.Wea. Rev*., **103**, 904-920.

ZANGVIL, A., and M. YANAI, 1981: Upper Tropospheric waves in the tropics. Part II: Association with clouds in the wavenumber-frequency domain, *J. Atmos. Sci*, **38**, 939-953.

ZIPSER, E. J., 1977: Mesoscale and convective-scale downdrafts as distinct components of squall-line structure, *Mon. Wea. Rev*., **105**, 1568-1589.

ZIPSER, E. J. and M. A. LEMONE, 1980: Cumulonimbus vertical velocity events in GATE. Part II: Synthesis and model core structure, *J. Atmos. Sci.*, **37**, 2458-2469

Appendix A – Phase plots for *u*

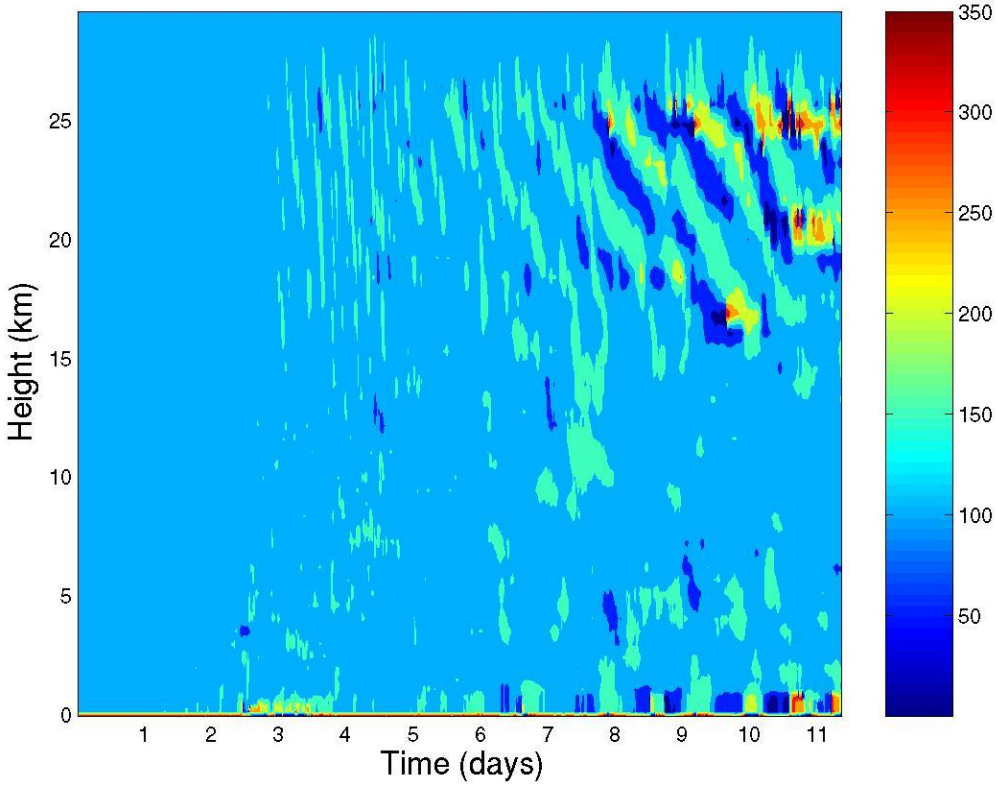

Phase plot for u 1 – *wavenumber 1*

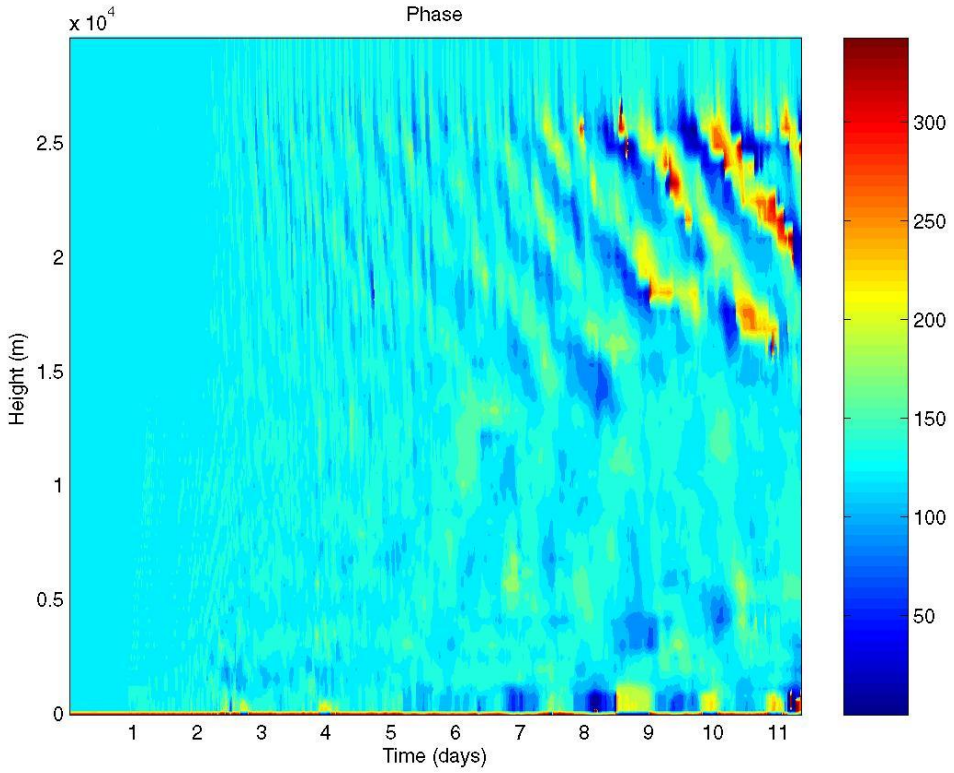

Phase plot for u 2 – *wavenumber 2*

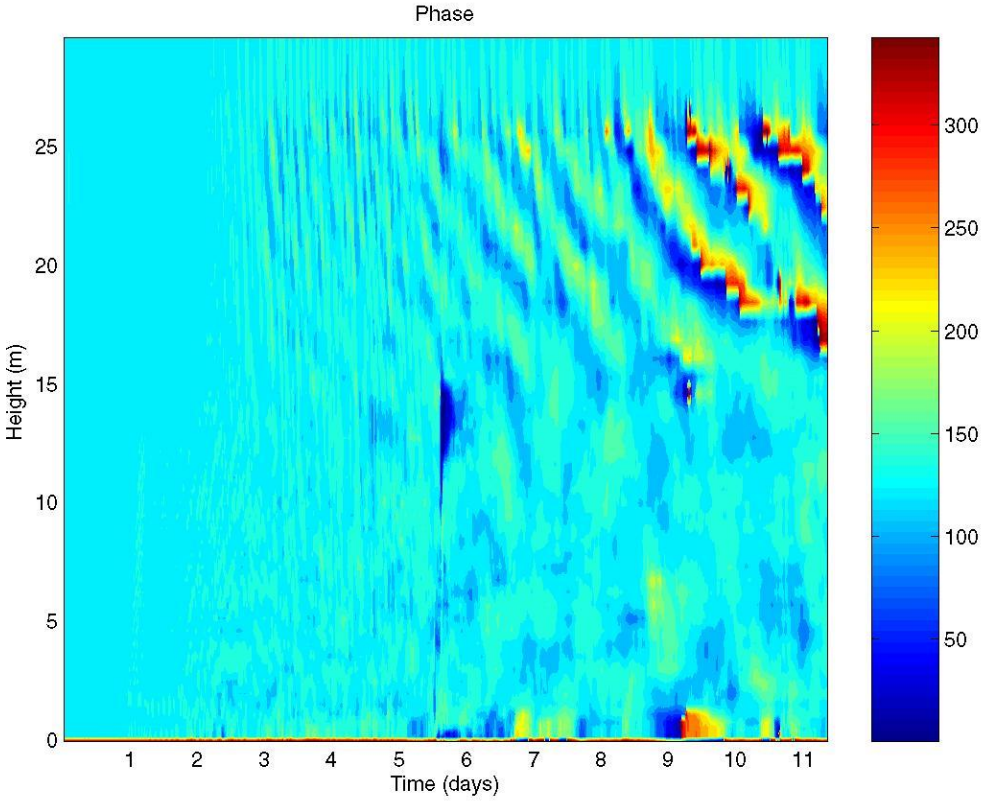

Phase plot for u 3 – *wavenumber 3*

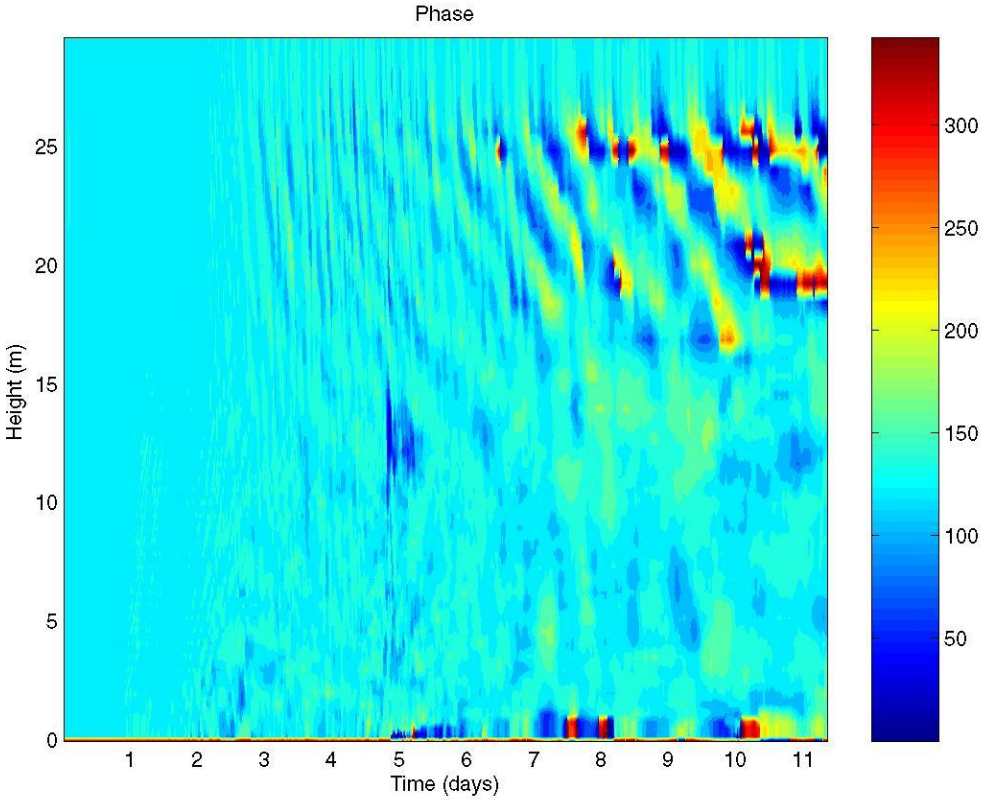

Phase plot for u 4 – *wavenumber 4*

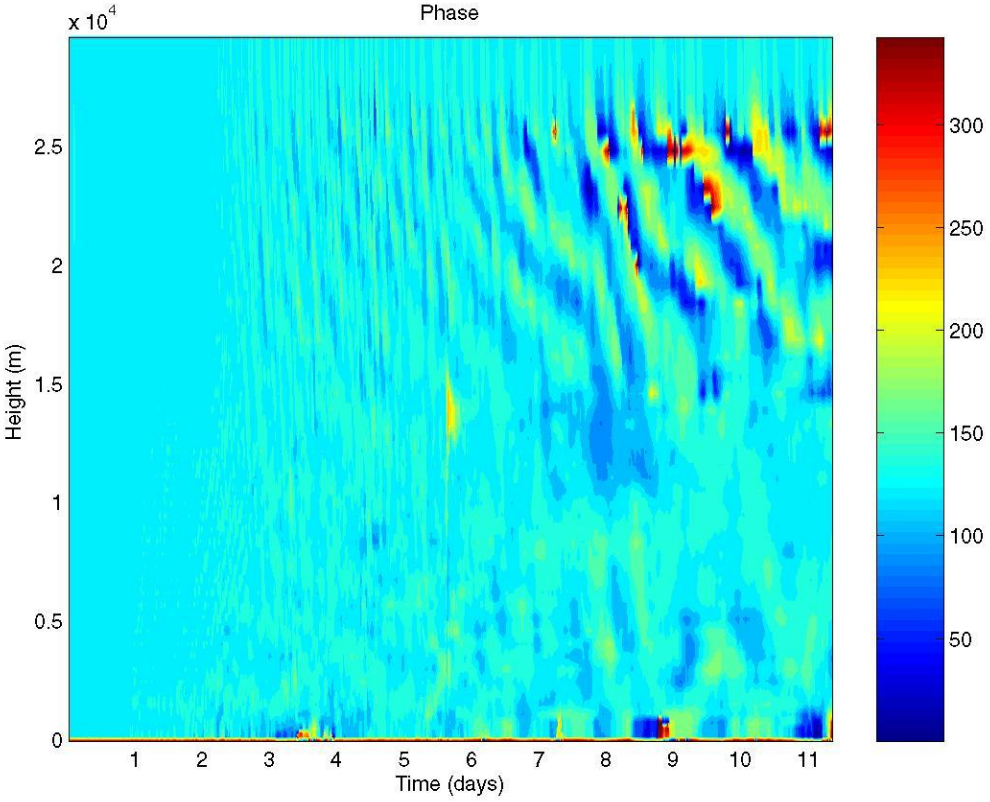

Phase plot for u 5 – *wavenumber 5*

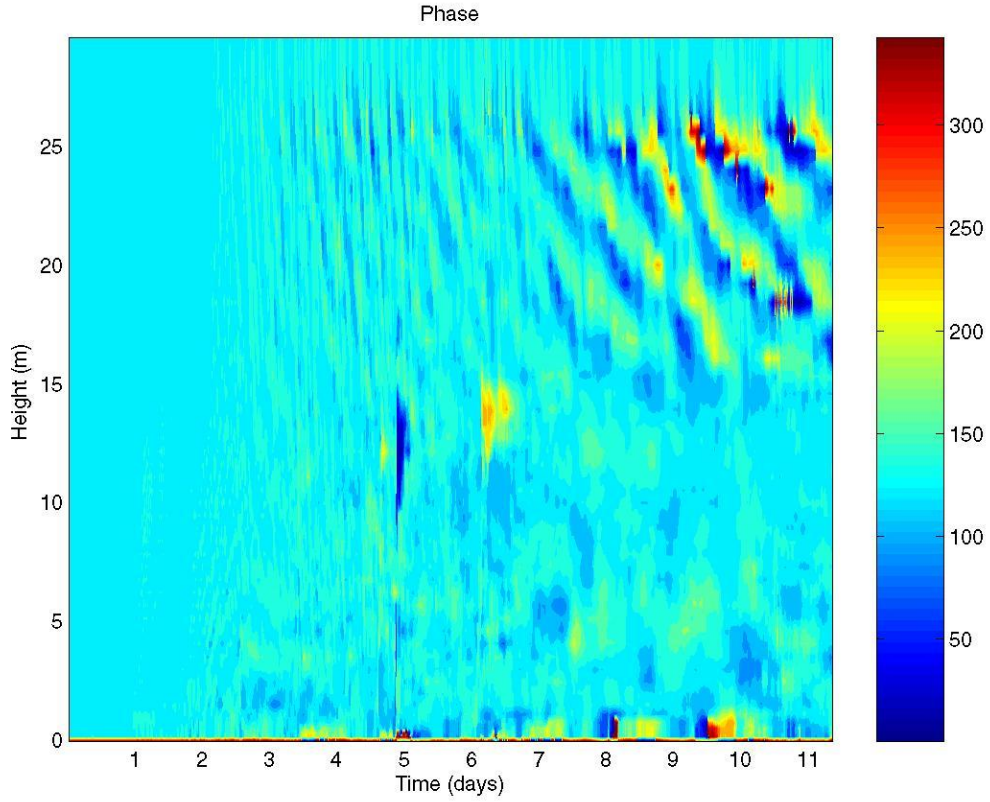

Phase plot for u 6 – *wavenumber 6*

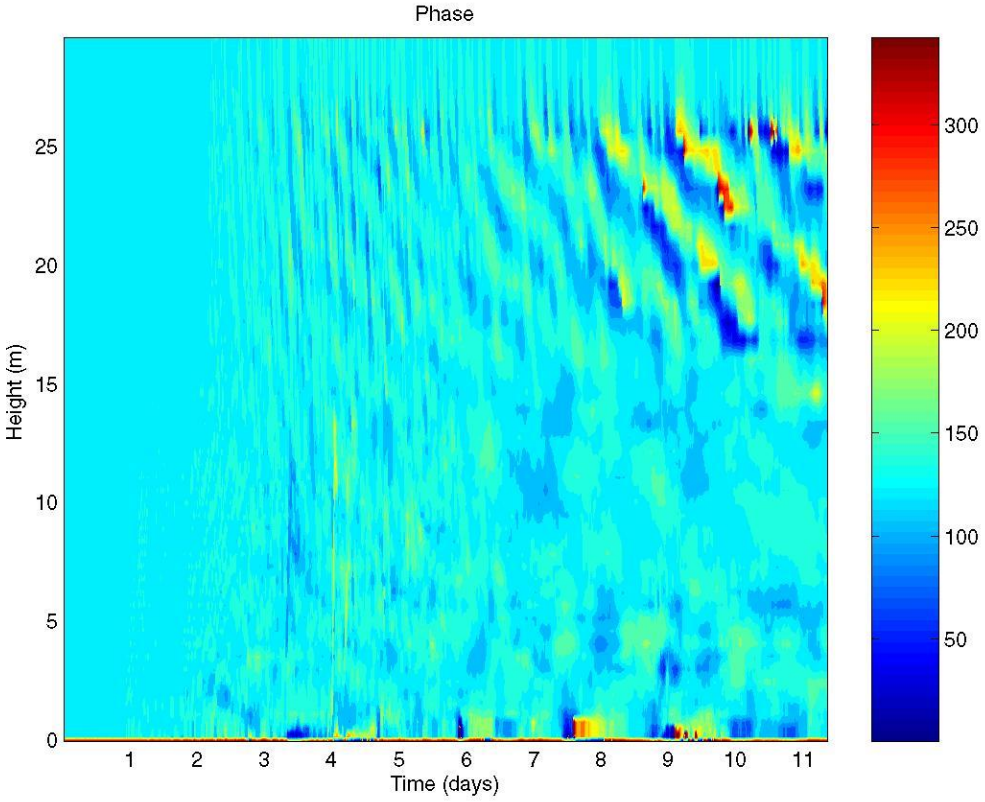

Phase plot for u 7 – *wavenumber 7*

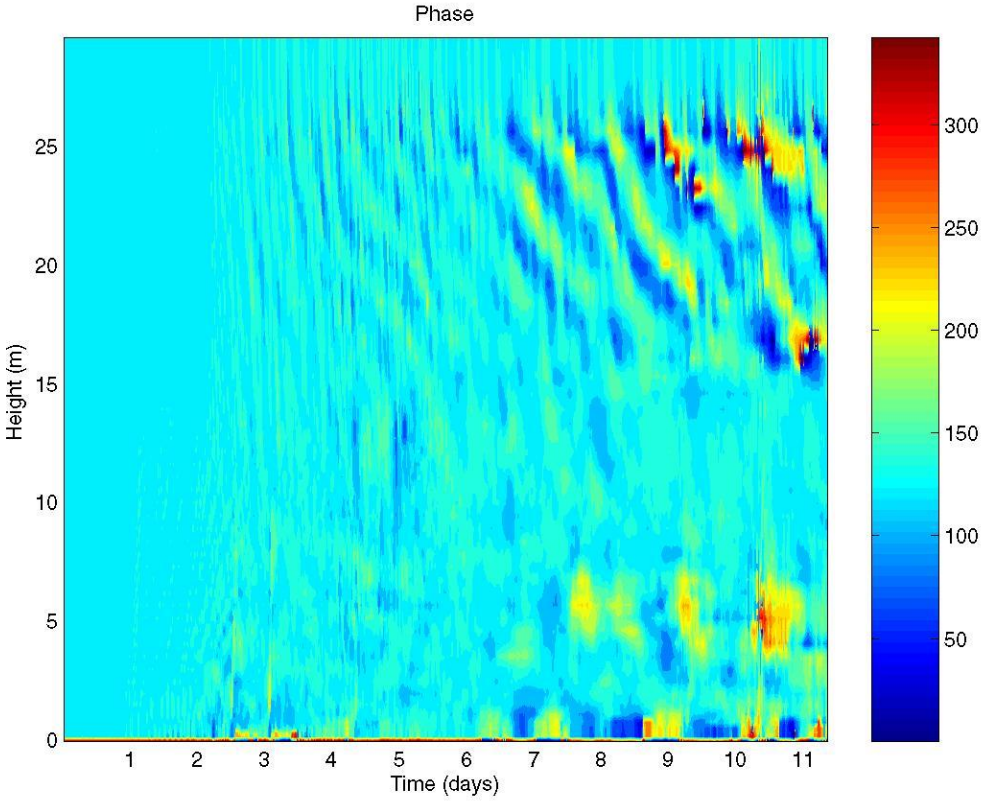

Phase plot for u 8 – *wavenumber 8*

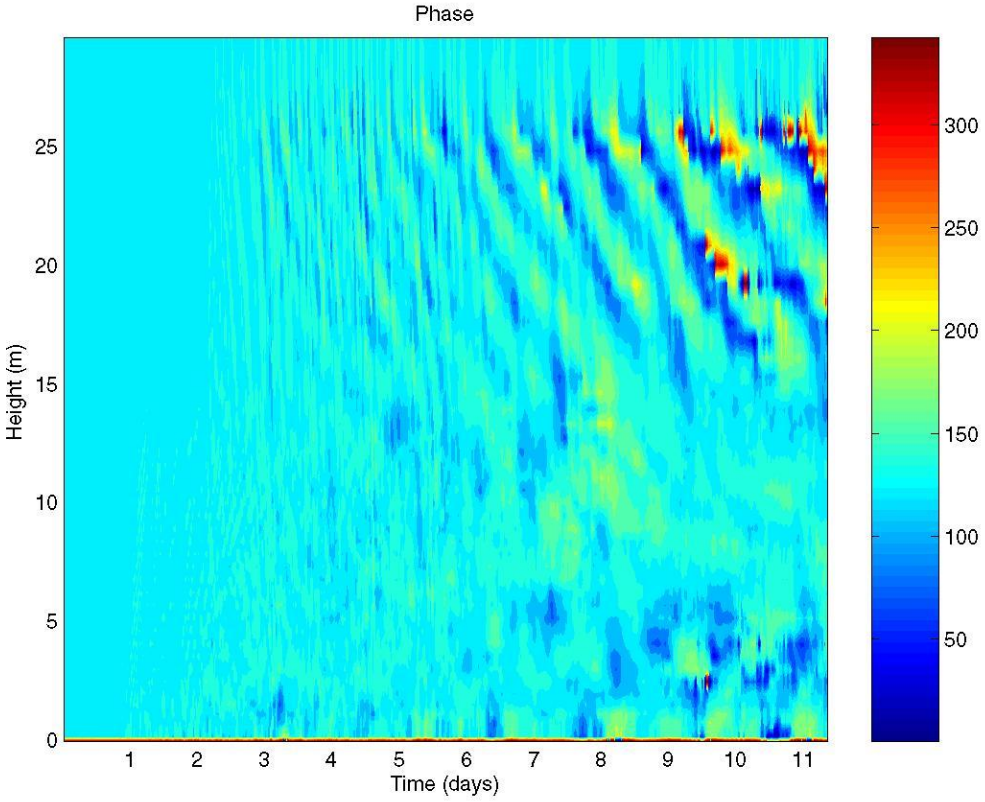

Phase plot for u 9 – *wavenumber 9*

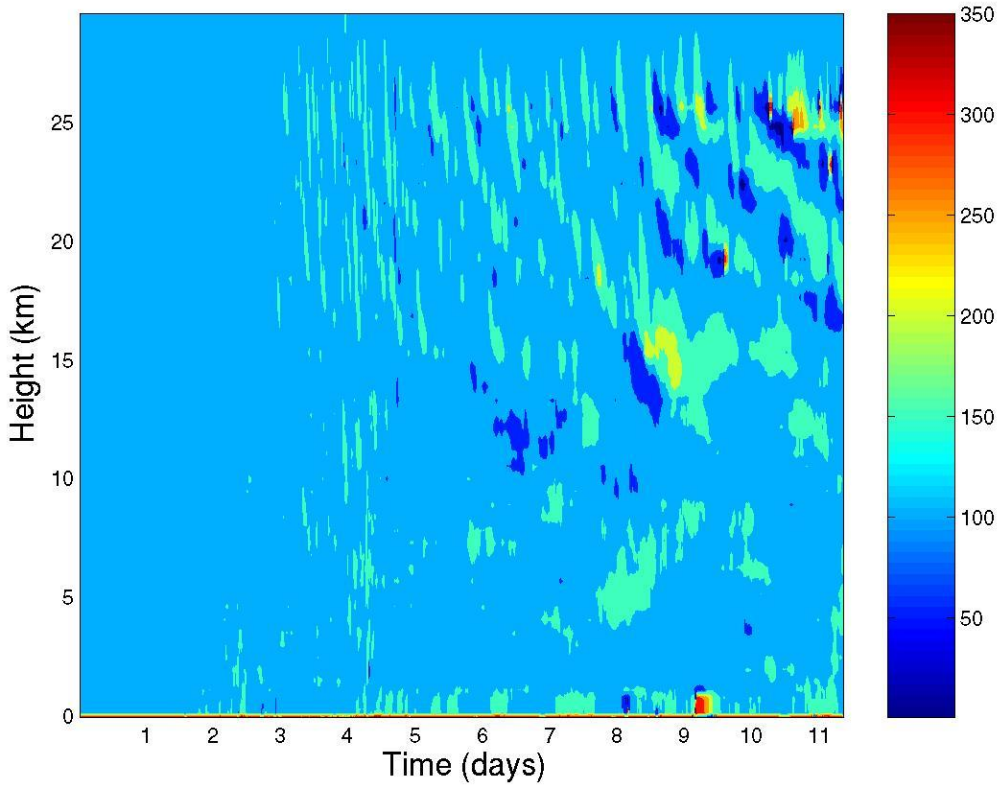

Phase plot for u 10 – *wavenumber 10*

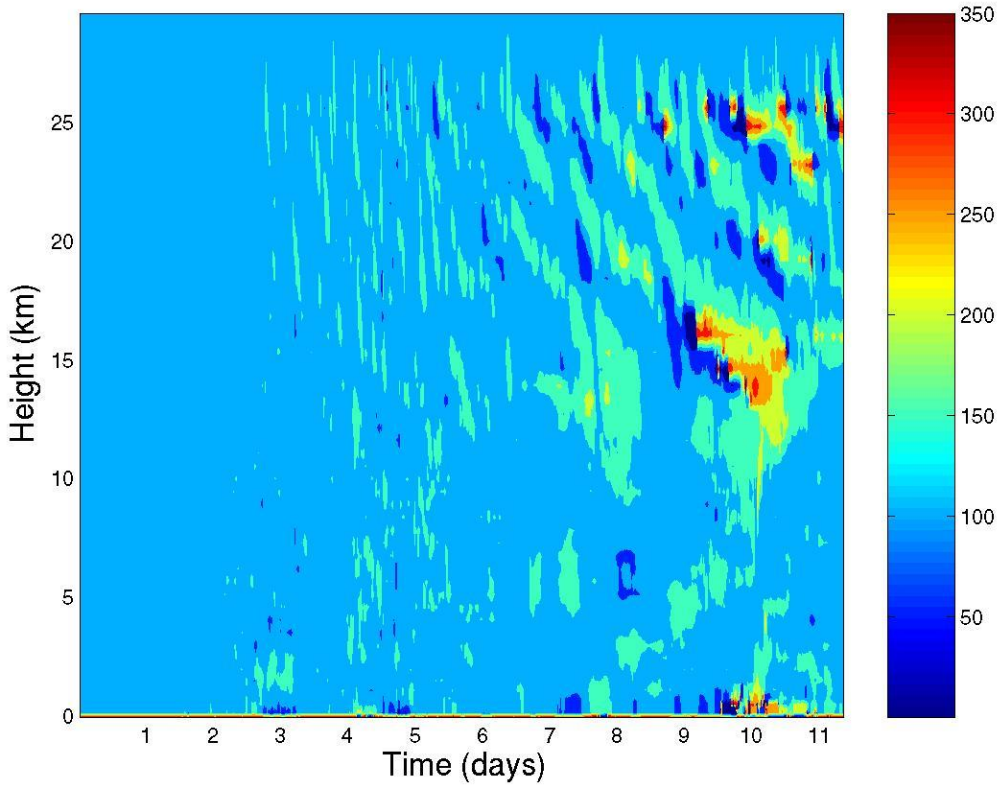

Phase plot for u 11 – *wavenumber 11*

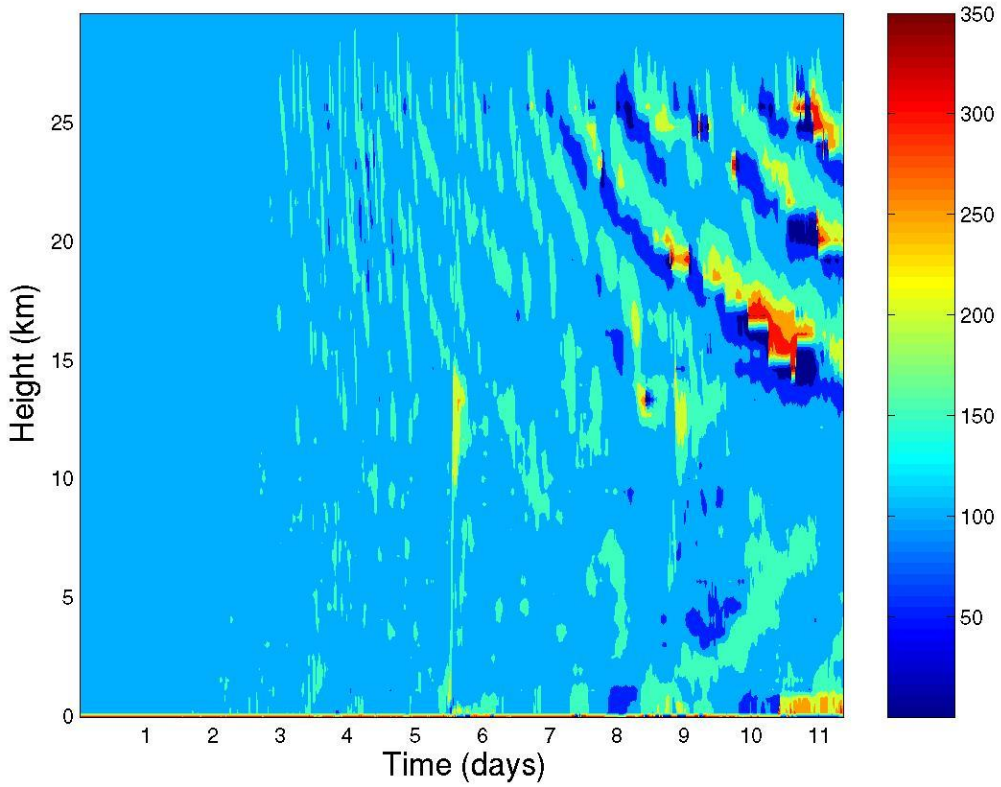

Phase plot for u 12 – *wavenumber 12*

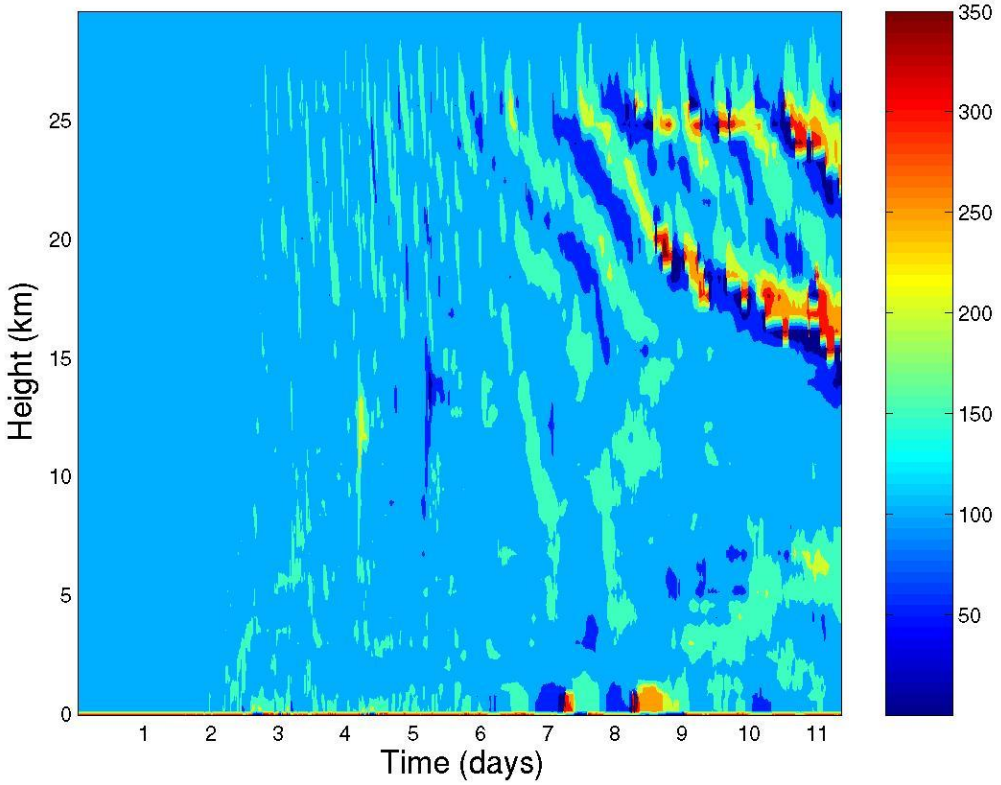

Phase plot for u 13 – *wavenumber 16*

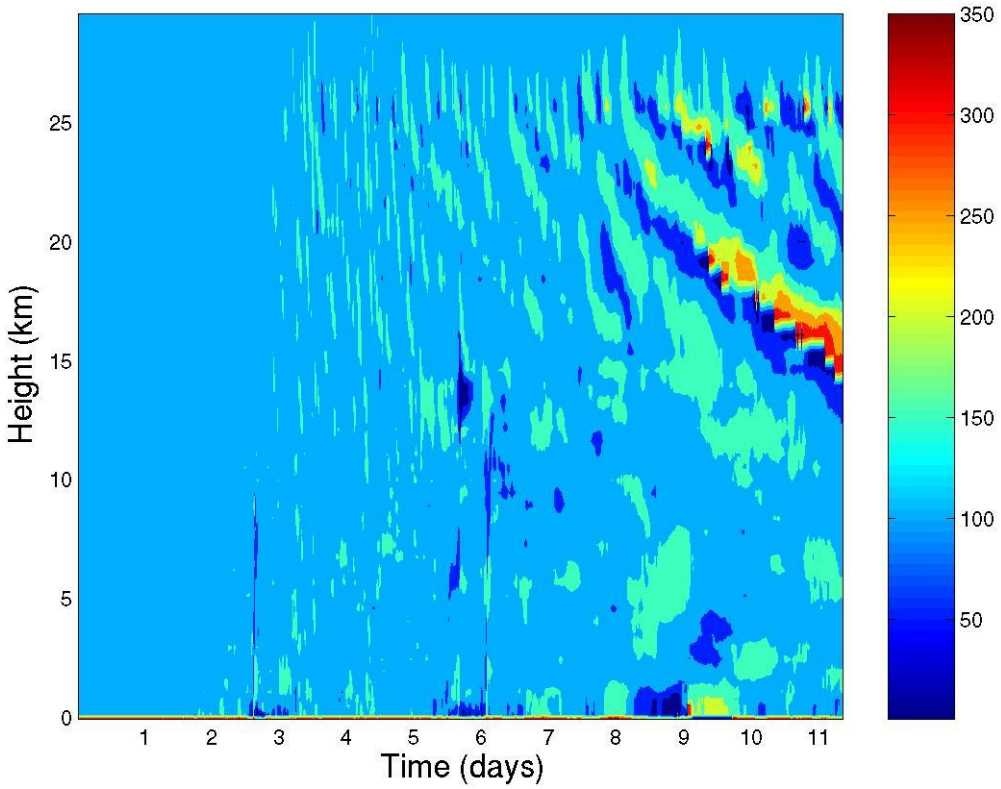

Phase plot for u 14 – *wavenumber 25*

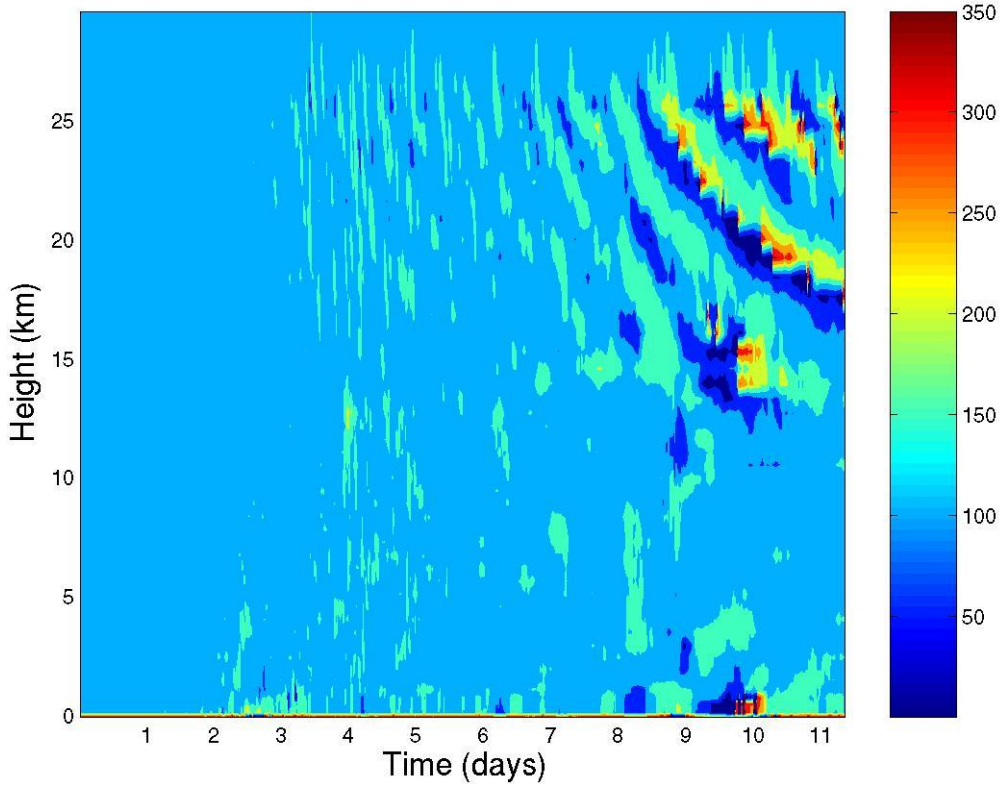

Phase plot for u 15 – *wavenumber 26*

Appendix B – Phase plots for *v*.

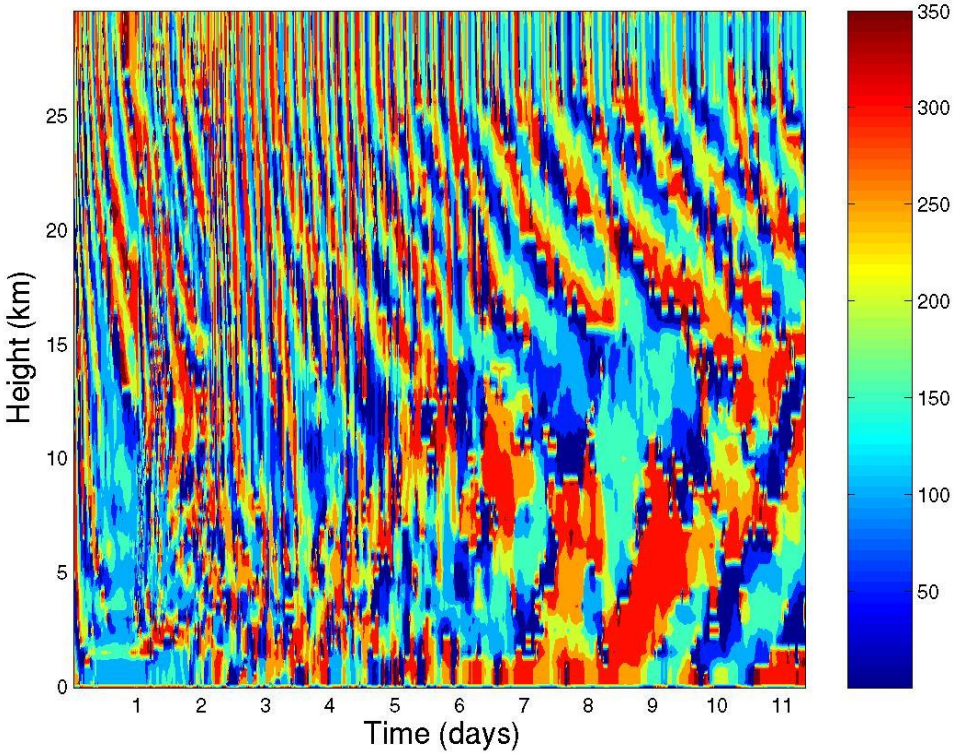

Phase plot for v 1 – *wavenumber 1*

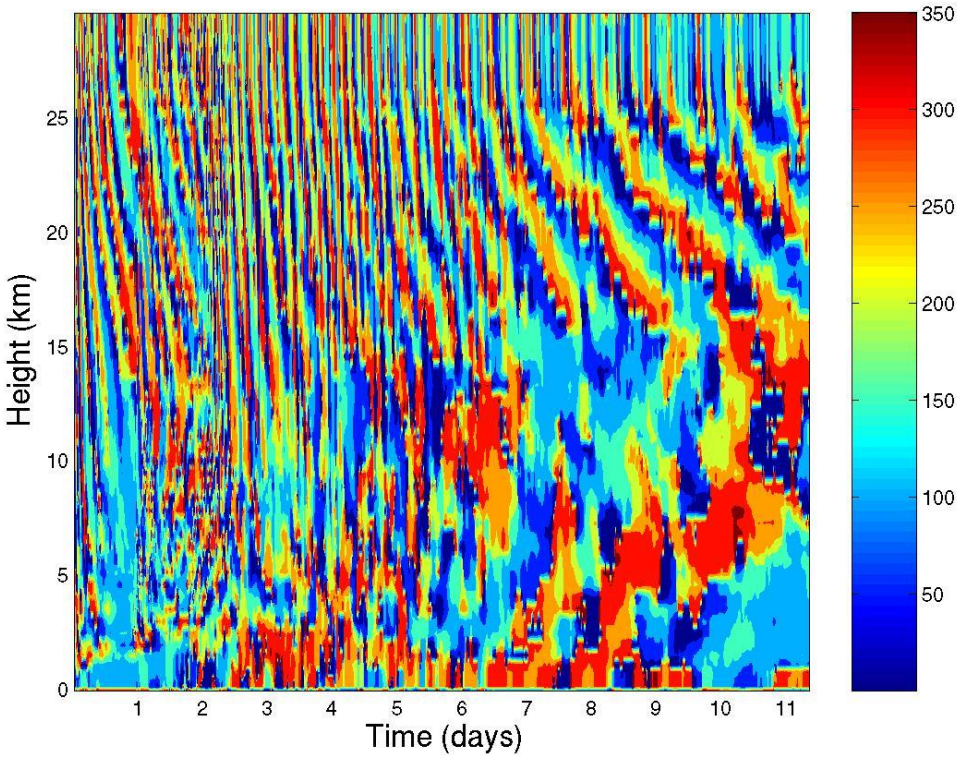

Phase plot for v 2 – *wavenumber 2*

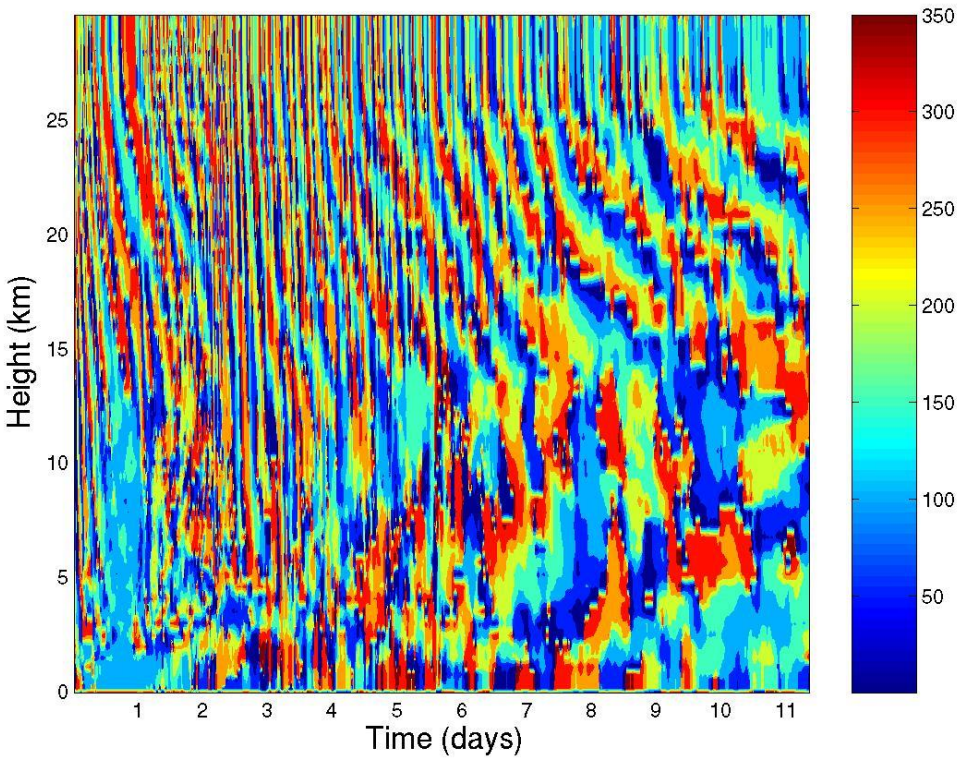

Phase plot for v 3 – *wavenumber 3*

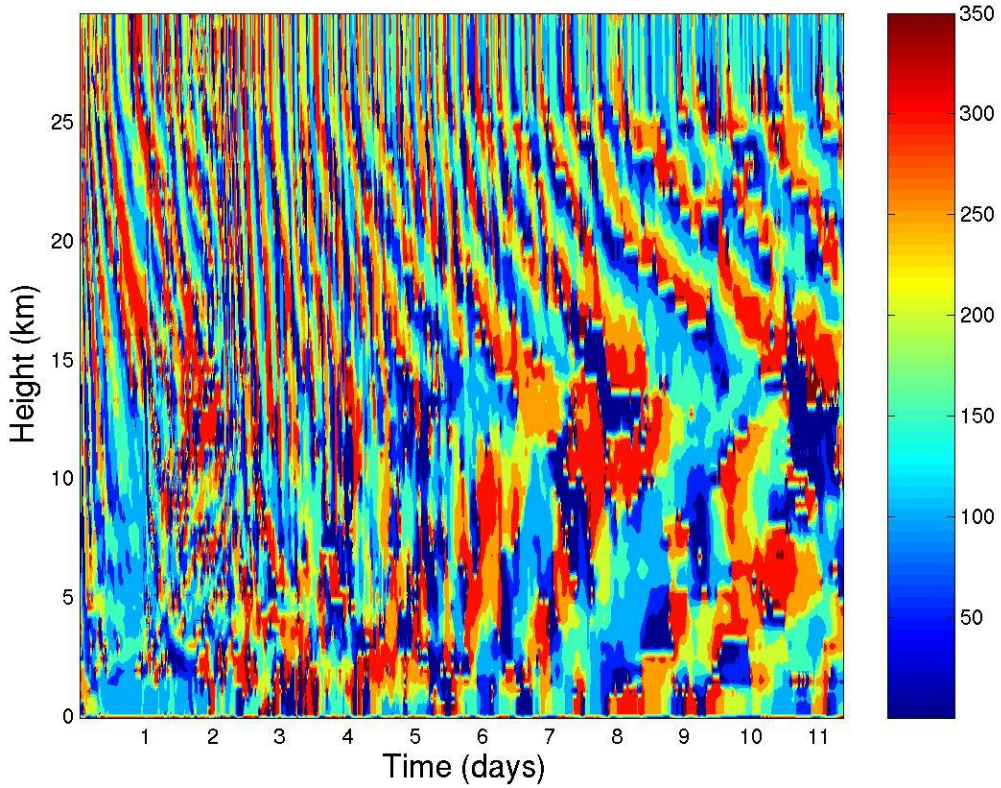

Phase plot for v 4 – *wavenumber 4*

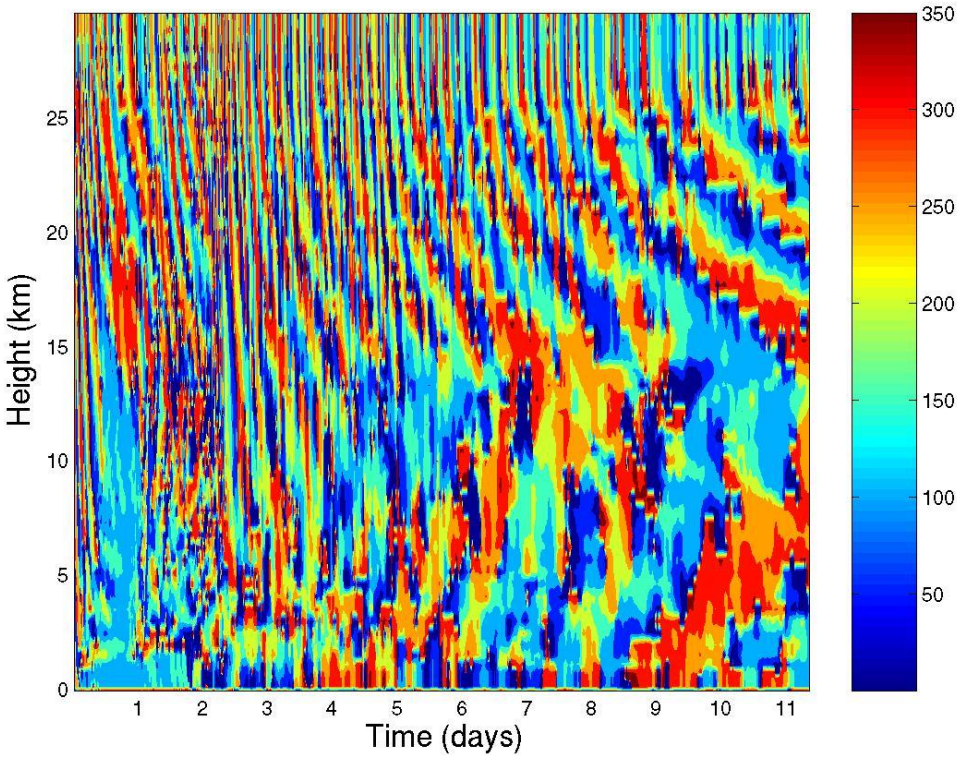

Phase plot for v 5 – *wavenumber 5*

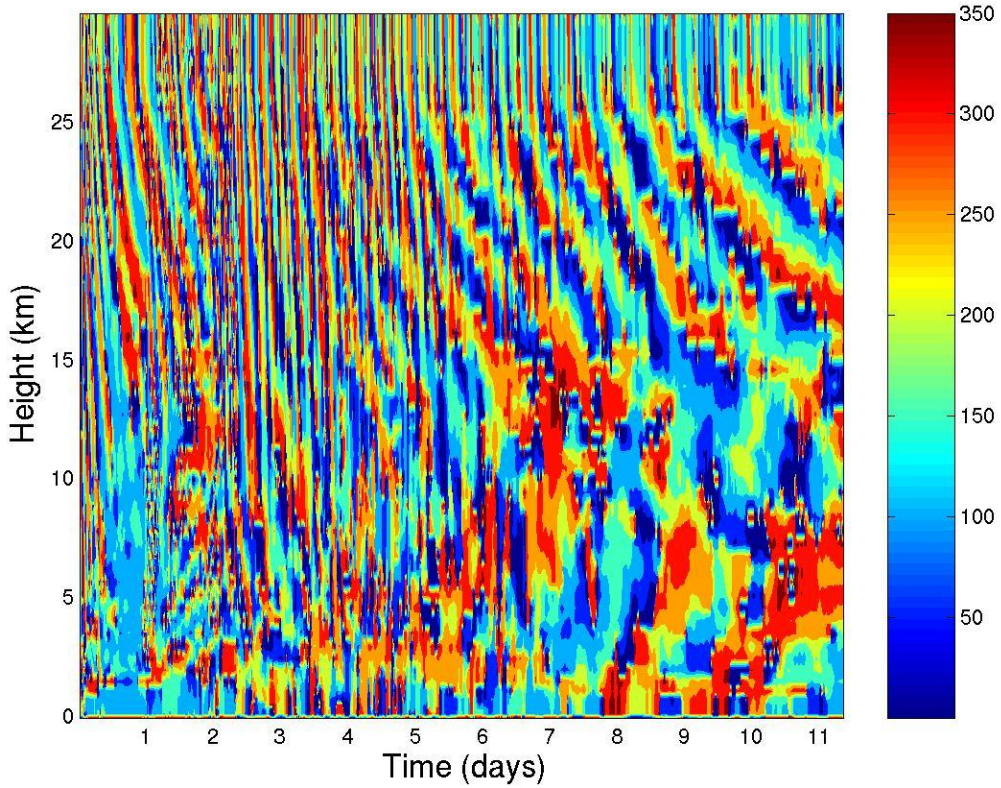

Phase plot for v 6 – *wavenumber 6*

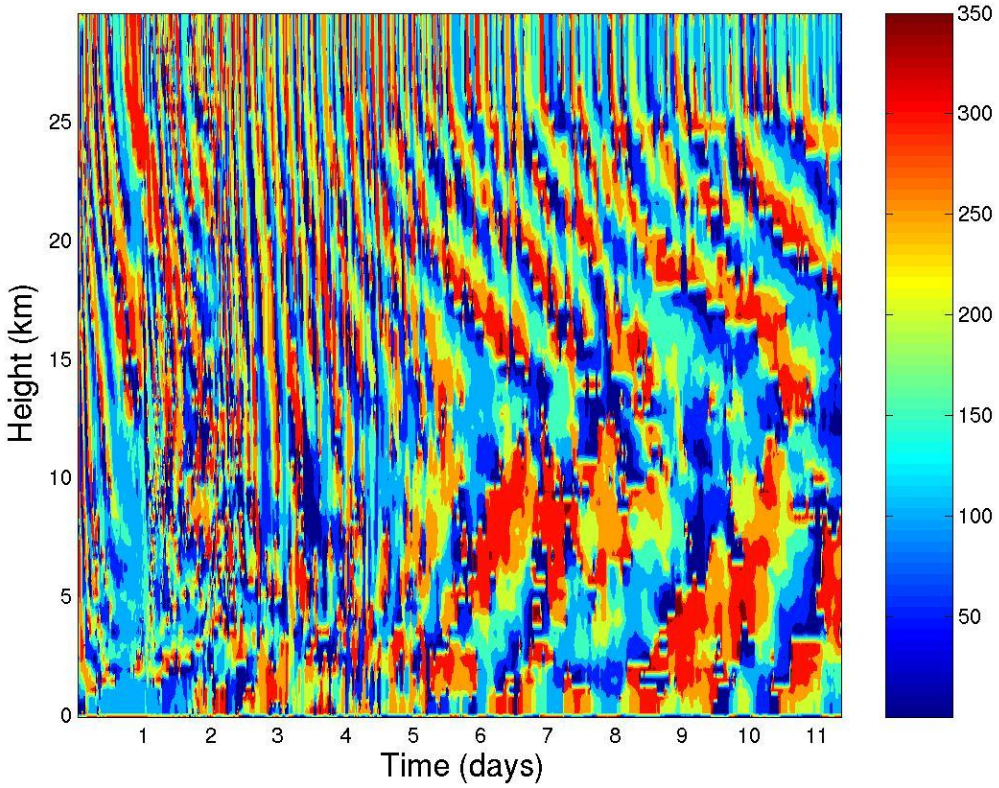

Phase plot for v 7 – *wavenumber 7*

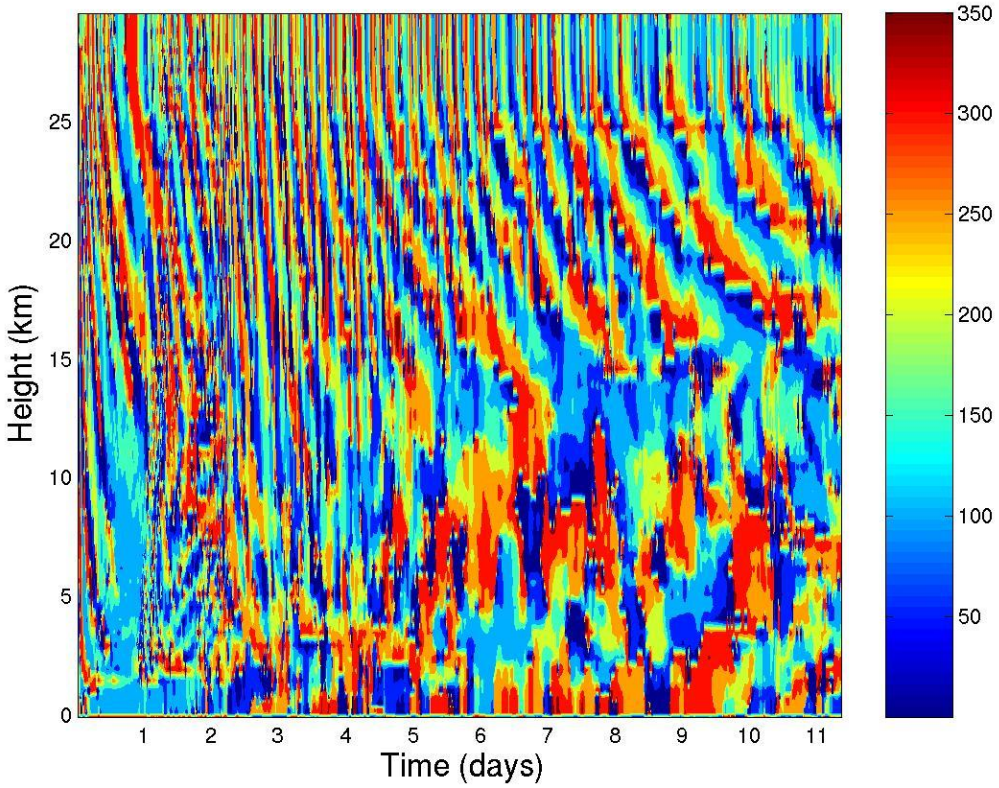

Phase plot for v 8 – *wavenumber 8*

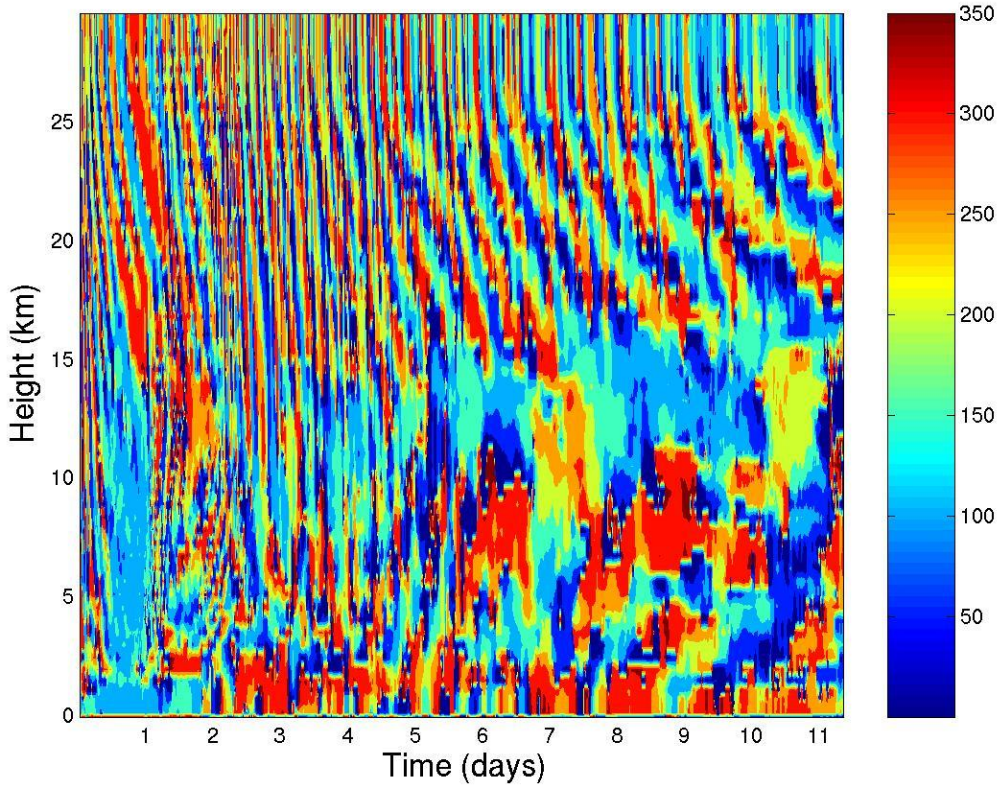

Phase plot for v 9 – *wavenumber 9*

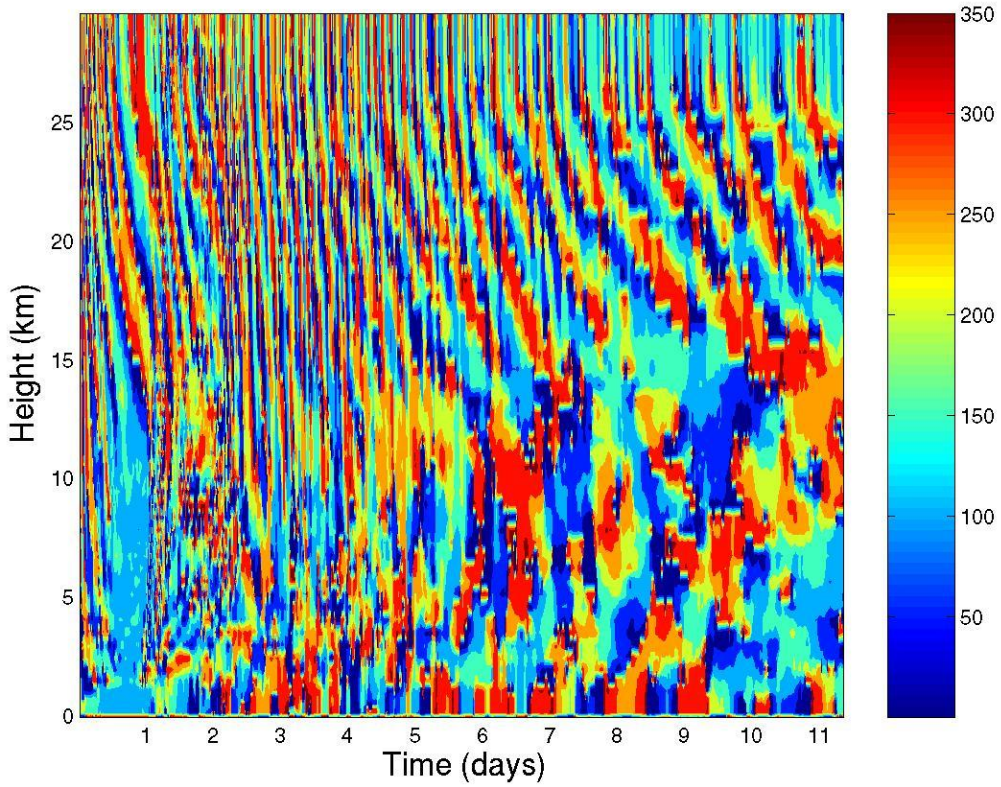

Phase plot for v 10 – *wavenumber 10*

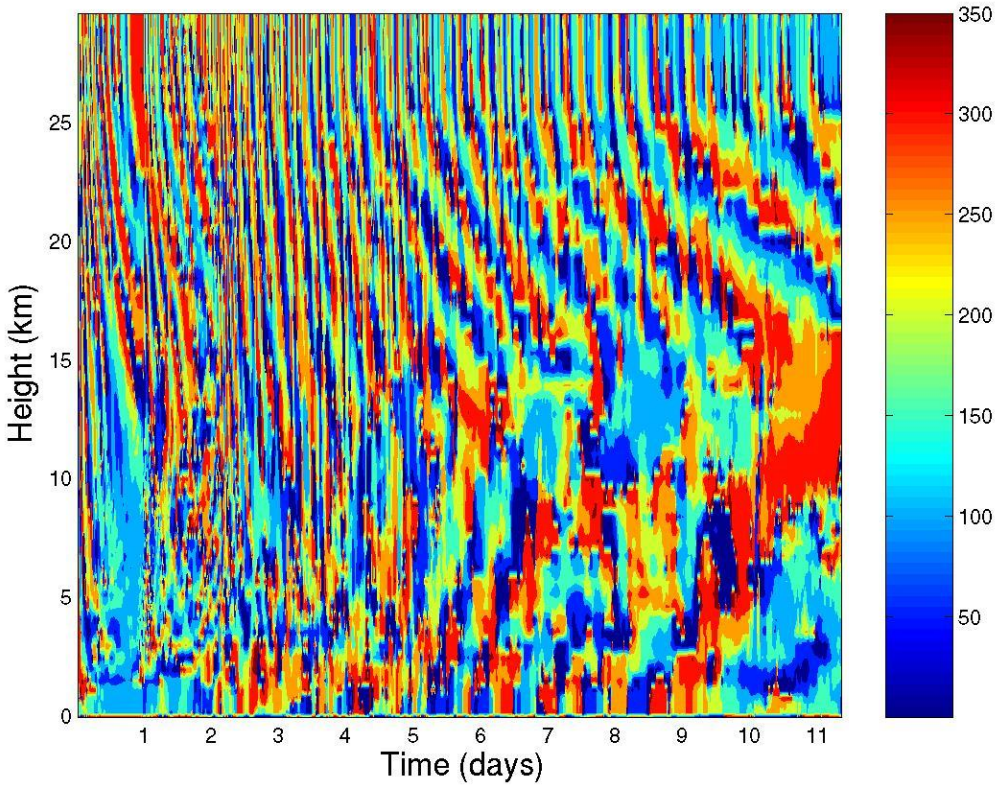

Phase plot for v 11 – *wavenumber 11*

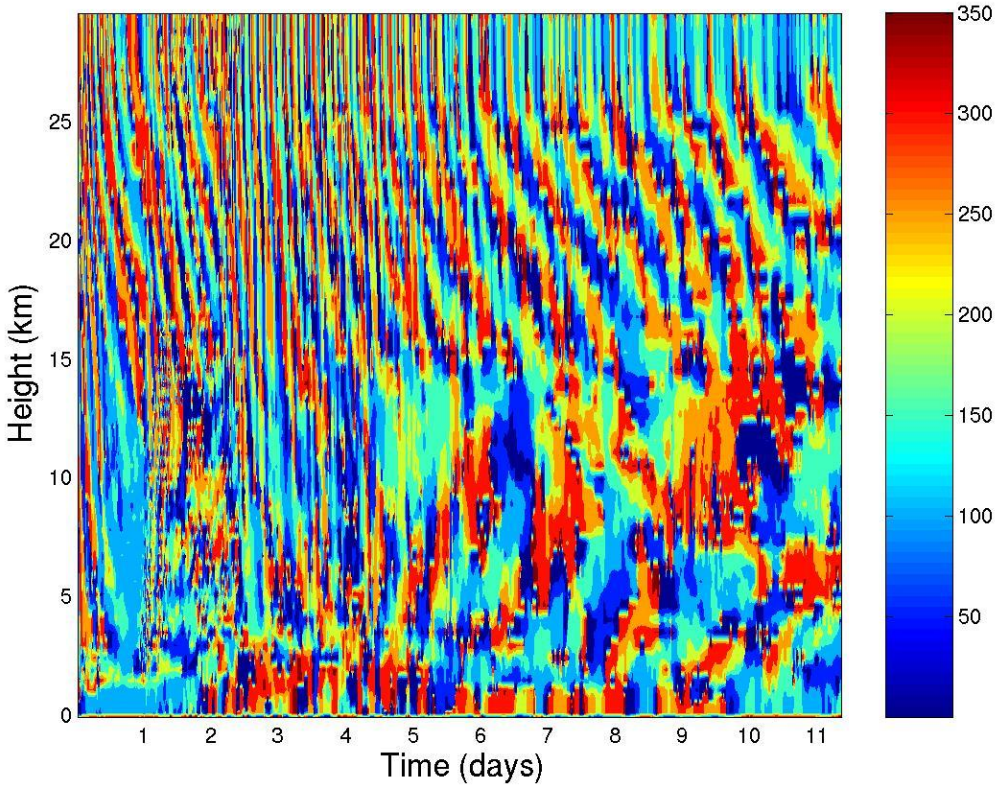

Phase plot for v 12 – *wavenumber 12*

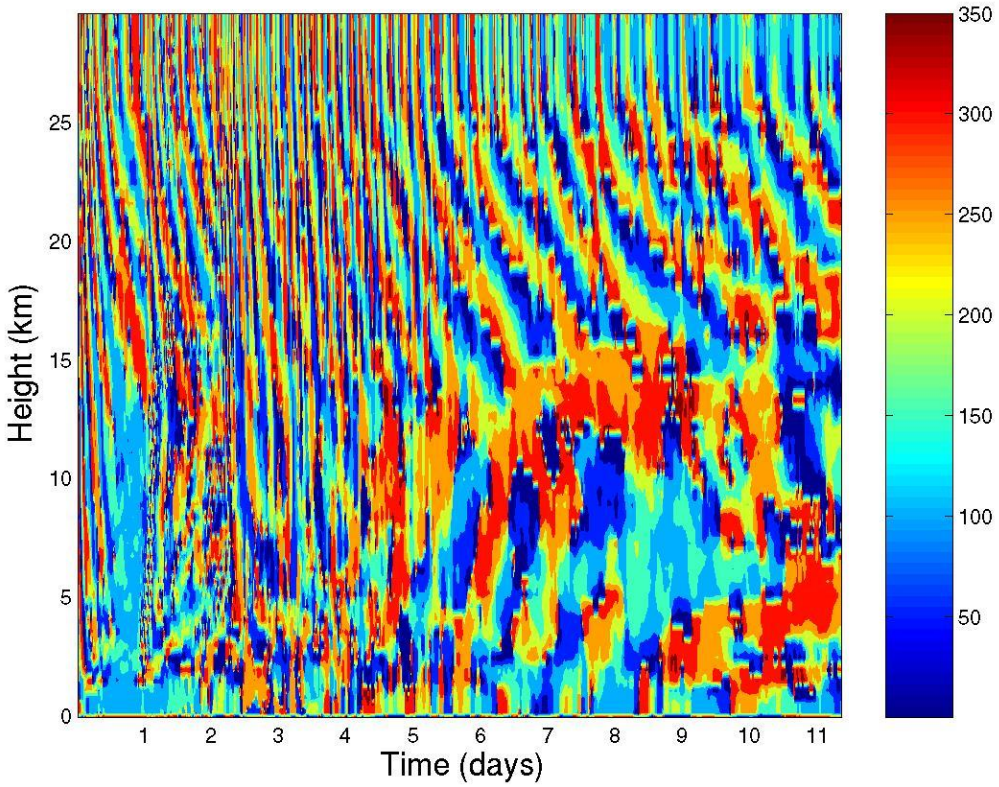

Phase plot for v 13 – *wavenumber 16*

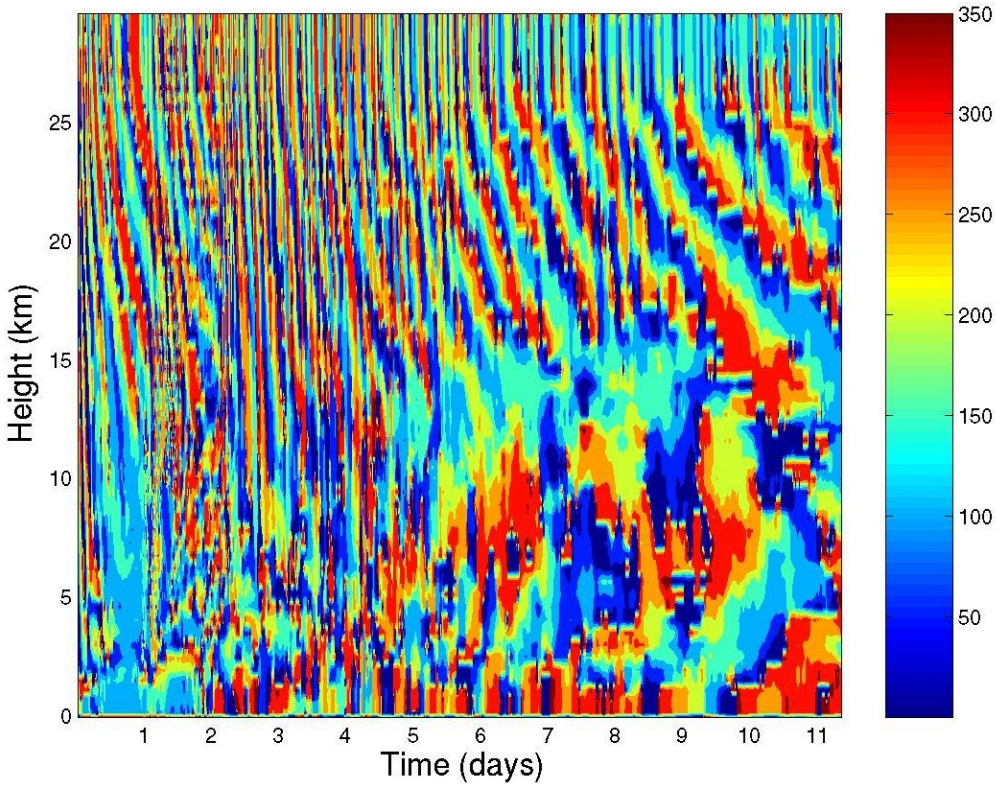

Phase plot for v 14 – *wavenumber 20*

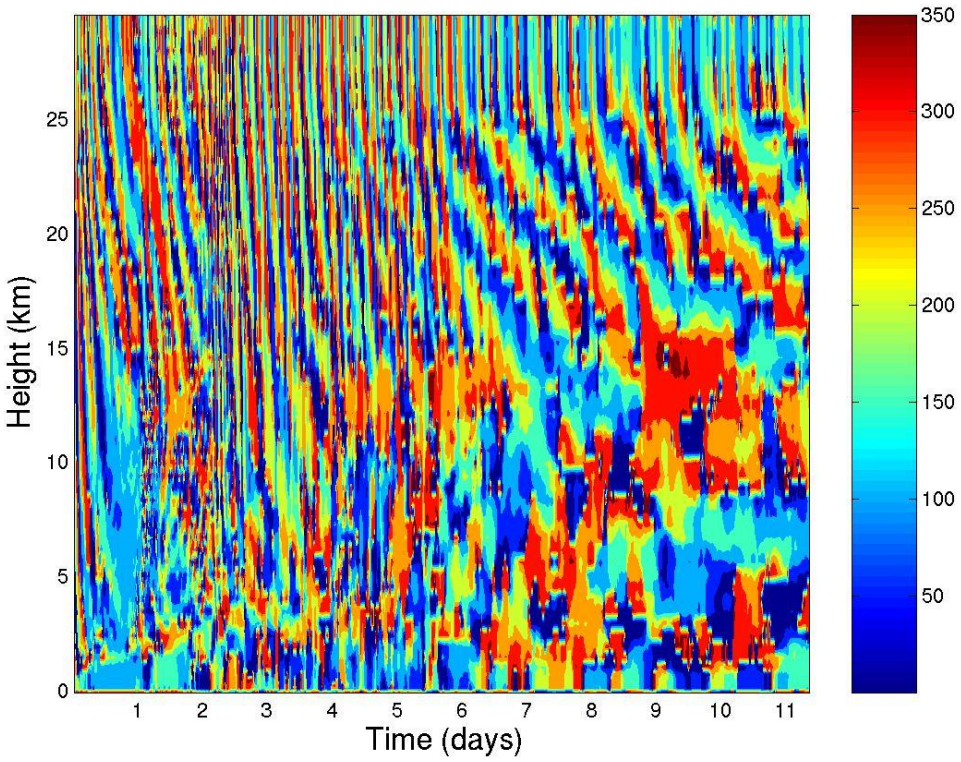

Phase plot for v 15 – *wavenumber 30*

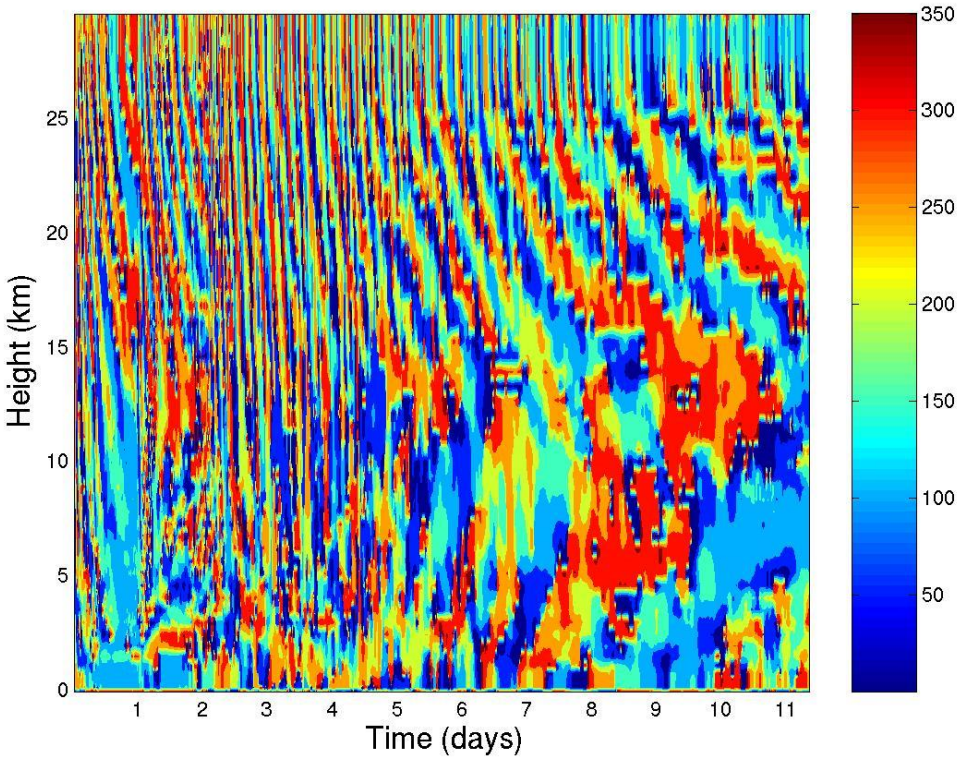

Phase plot for v 16 – *wavenumber 31*

Appendix C – Table of Calculations

This table shows the measured period and the values of *k, k*, m, m** and vertical wavelength calculated from the linear wave theory. The lines highlighted in bold represent the most relevant waves to the estimated actual vertical wavelength.

Wave-number	n	Period (s)	Wavelength (km)	k	k*	m	m*	Theoretical h(km)	phase speed
1	-1	72576	4.00E+07	1.57E-07	5.91E-01	4.57E-05	5.91E-01	137.419	551.146
1	0	72576	4.00E+07	1.57E-07	5.91E-01	1.23E-04	1.59E+00	51.060	551.146
1	1	72576	4.00E+07	1.57E-07	5.91E-01	2.54E-04	3.29E+00	24.724	551.146
1	2	72576	4.00E+07	1.57E-07	5.91E-01	4.01E-04	5.18E+00	15.681	551.146
1	3	72576	4.00E+07	1.57E-07	5.91E-01	5.52E-04	7.13E+00	11.392	551.146
1	**4**	**72576**	**4.00E+07**	**1.57E-07**	**5.91E-01**	**7.04E-04**	**9.10E+00**	**8.925**	**551.146**
1	**5**	**72576**	**4.00E+07**	**1.57E-07**	**5.91E-01**	**8.57E-04**	**1.11E+01**	**7.330**	**551.146**
1	6	72576	4.00E+07	1.57E-07	5.91E-01	1.01E-03	1.31E+01	6.216	551.146
1	7	72576	4.00E+07	1.57E-07	5.91E-01	1.16E-03	1.51E+01	5.394	551.146
2	-1	101606.4	2.00E+07	3.14E-07	8.45E-01	1.28E-04	8.45E-01	49.078	196.838
2	0	101606.4	2.00E+07	3.14E-07	8.45E-01	2.80E-04	1.84E+00	22.473	196.838
2	1	101606.4	2.00E+07	3.14E-07	8.45E-01	5.23E-04	3.45E+00	12.011	196.838
2	2	101606.4	2.00E+07	3.14E-07	8.45E-01	8.02E-04	5.29E+00	7.830	196.838
2	**3**	**101606.4**	**2.00E+07**	**3.14E-07**	**8.45E-01**	**1.09E-03**	**7.22E+00**	**5.745**	**196.838**
2	4	101606.4	2.00E+07	3.14E-07	8.45E-01	1.39E-03	9.17E+00	4.521	196.838
2	5	101606.4	2.00E+07	3.14E-07	8.45E-01	1.69E-03	1.11E+01	3.721	196.838
4	-1	120960	1.00E+07	6.28E-07	1.42E+00	3.05E-04	1.42E+00	20.613	82.672
4	0	120960	1.00E+07	6.28E-07	1.42E+00	5.20E-04	2.42E+00	12.092	82.672
4	1	120960	1.00E+07	6.28E-07	1.42E+00	8.34E-04	3.88E+00	7.531	82.672
4	**2**	**120960**	**1.00E+07**	**6.28E-07**	**1.42E+00**	**1.21E-03**	**5.61E+00**	**5.212**	**82.672**
4	3	120960	1.00E+07	6.28E-07	1.42E+00	1.60E-03	7.46E+00	3.921	82.672
4	4	120960	1.00E+07	6.28E-07	1.42E+00	2.01E-03	9.37E+00	3.123	82.672
4	5	120960	1.00E+07	6.28E-07	1.42E+00	2.43E-03	1.13E+01	2.588	82.672
12	-1	94348.8	3.33E+06	1.88E-06	5.46E+00	7.13E-04	5.46E+00	8.809	35.330
12	0	94348.8	3.33E+06	1.88E-06	5.46E+00	8.44E-04	6.46E+00	7.445	35.330
12	1	94348.8	3.33E+06	1.88E-06	5.46E+00	9.96E-04	7.62E+00	6.307	35.330
12	**2**	**94348.8**	**3.33E+06**	**1.88E-06**	**5.46E+00**	**1.17E-03**	**8.94E+00**	**5.377**	**35.330**
12	3	94348.8	3.33E+06	1.88E-06	5.46E+00	1.36E-03	1.04E+01	4.627	35.330
12	4	94348.8	3.33E+06	1.88E-06	5.46E+00	1.56E-03	1.19E+01	4.023	35.330
12	5	94348.8	3.33E+06	1.88E-06	5.46E+00	1.78E-03	1.36E+01	3.537	35.330
16	-1	87091.2	2.50E+06	2.51E-06	7.88E+00	8.78E-04	7.88E+00	7.157	28.706
16	0	87091.2	2.50E+06	2.51E-06	7.88E+00	9.89E-04	8.88E+00	6.352	28.706
16	1	87091.2	2.50E+06	2.51E-06	7.88E+00	1.11E-03	1.00E+01	5.641	28.706
16	**2**	**87091.2**	**2.50E+06**	**2.51E-06**	**7.88E+00**	**1.25E-03**	**1.12E+01**	**5.023**	**28.706**
16	3	87091.2	2.50E+06	2.51E-06	7.88E+00	1.40E-03	1.26E+01	4.488	28.706
16	4	87091.2	2.50E+06	2.51E-06	7.88E+00	1.56E-03	1.40E+01	4.030	28.706
16	5	87091.2	2.50E+06	2.51E-06	7.88E+00	1.73E-03	1.55E+01	3.637	28.706

Appendix D – Hovmöller diagrams of Precipitation

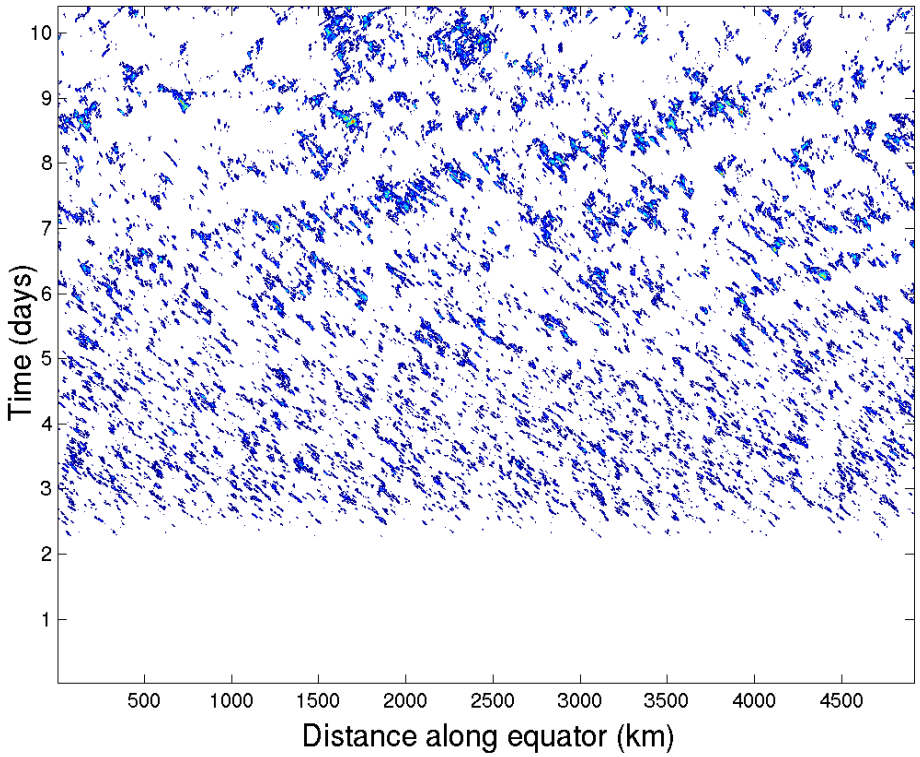

Hovmöller 1 – *0 to 5000 km*

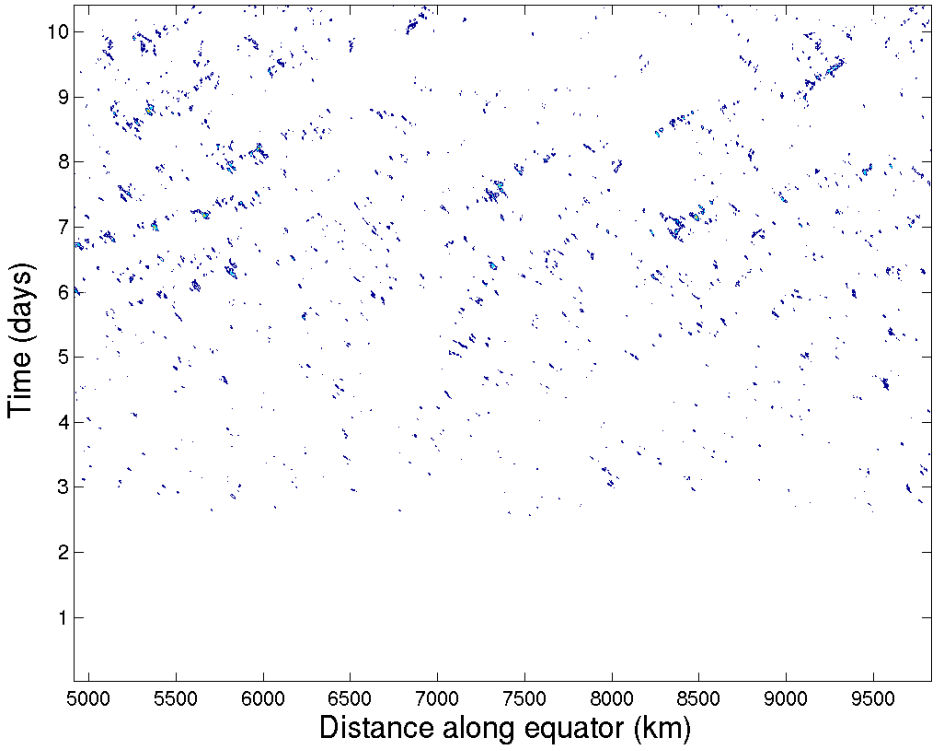

Hovmöller 2 – *5000 to 10,000 km*

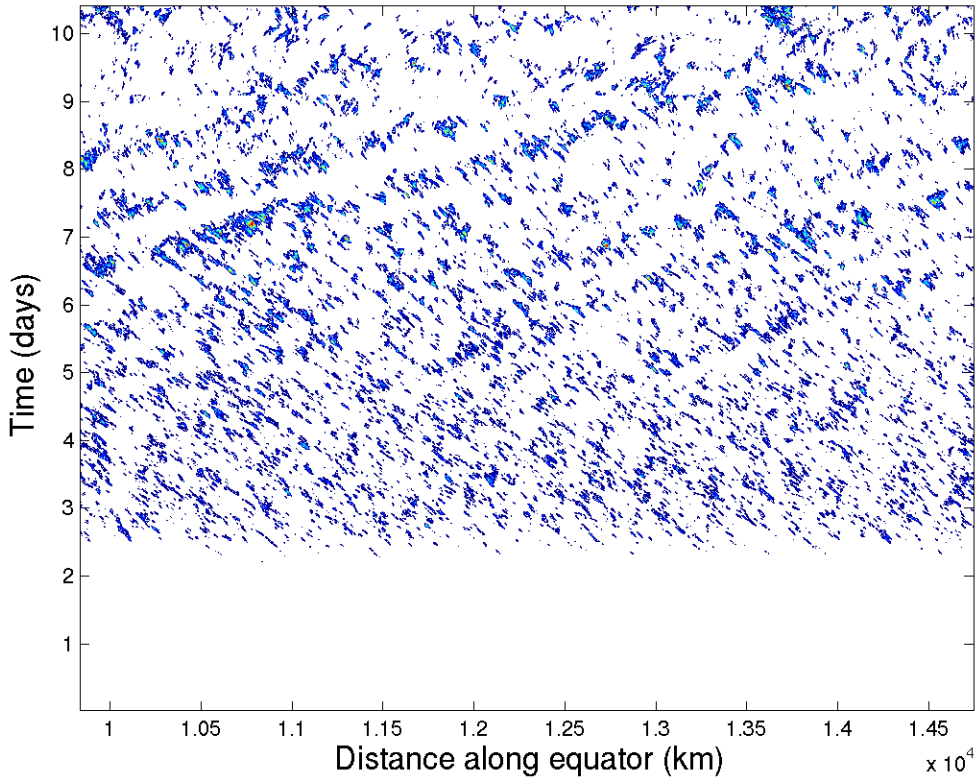

Hovmöller 3 – *10,000 – 15,000 km*

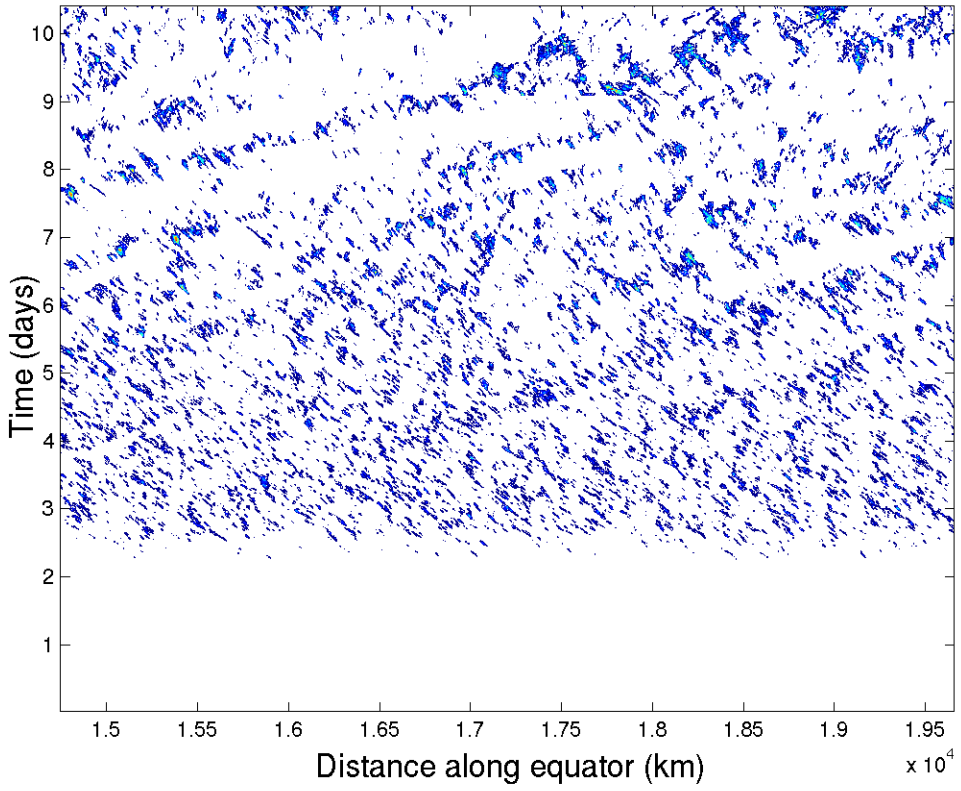

Hovmöller 4 – *15,000 – 20,000 km*

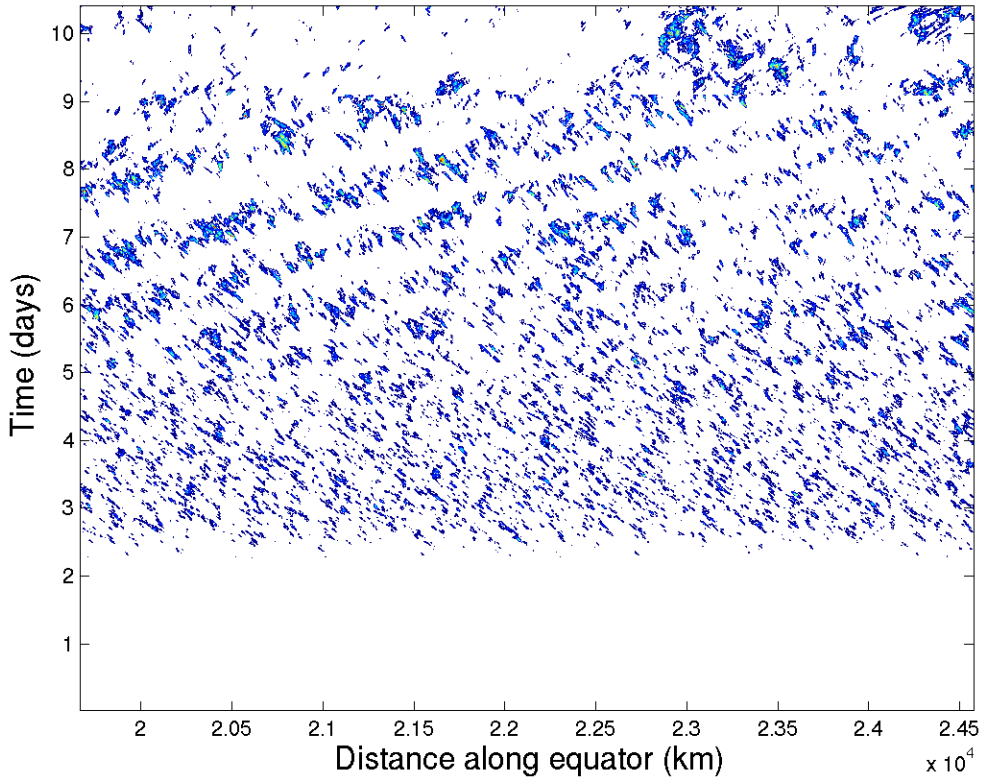

Hovmöller 5 – *20,000 – 25,000 km*

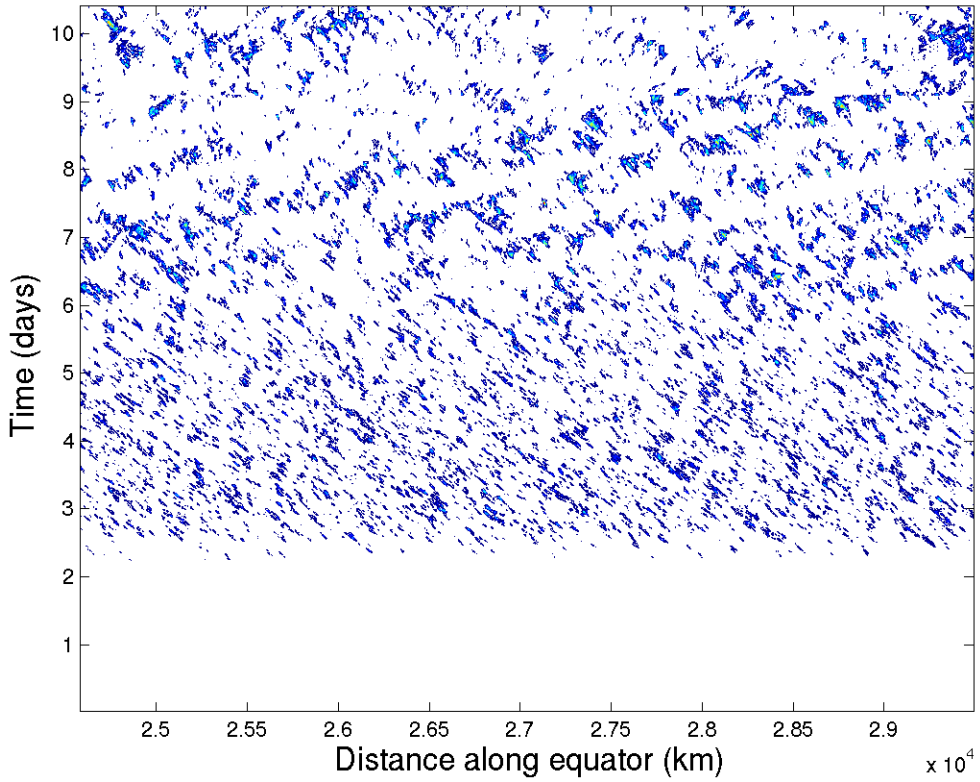

Hovmöller 6 – *25,000 – 30,000 km*

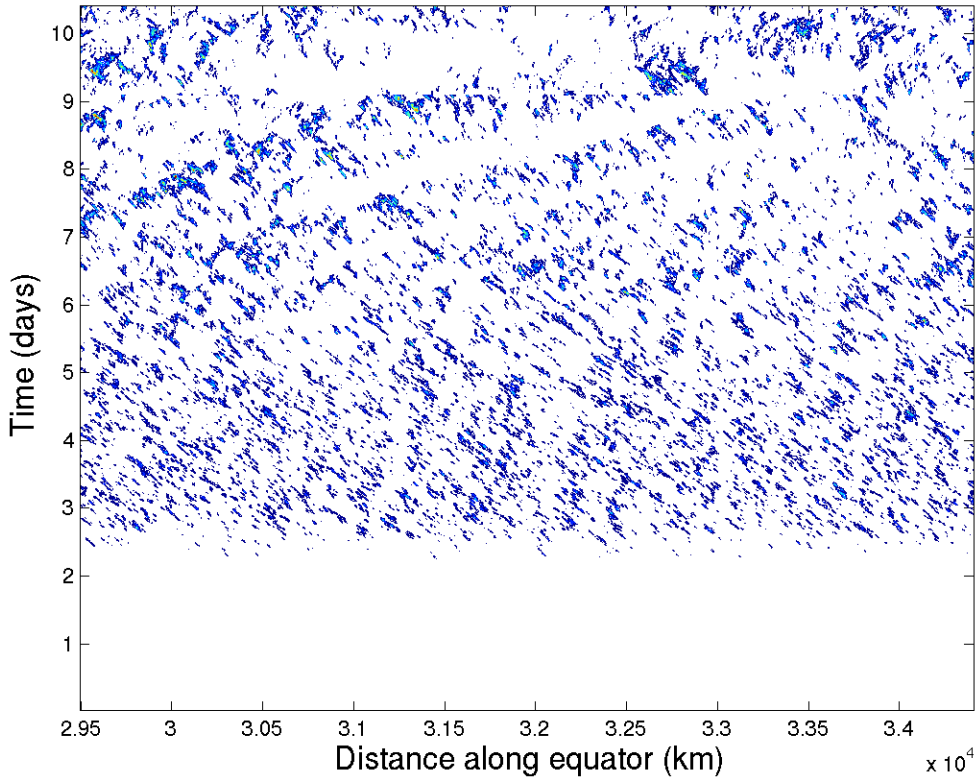

Hovmöller 7 – *30,000 – 35,000 km*

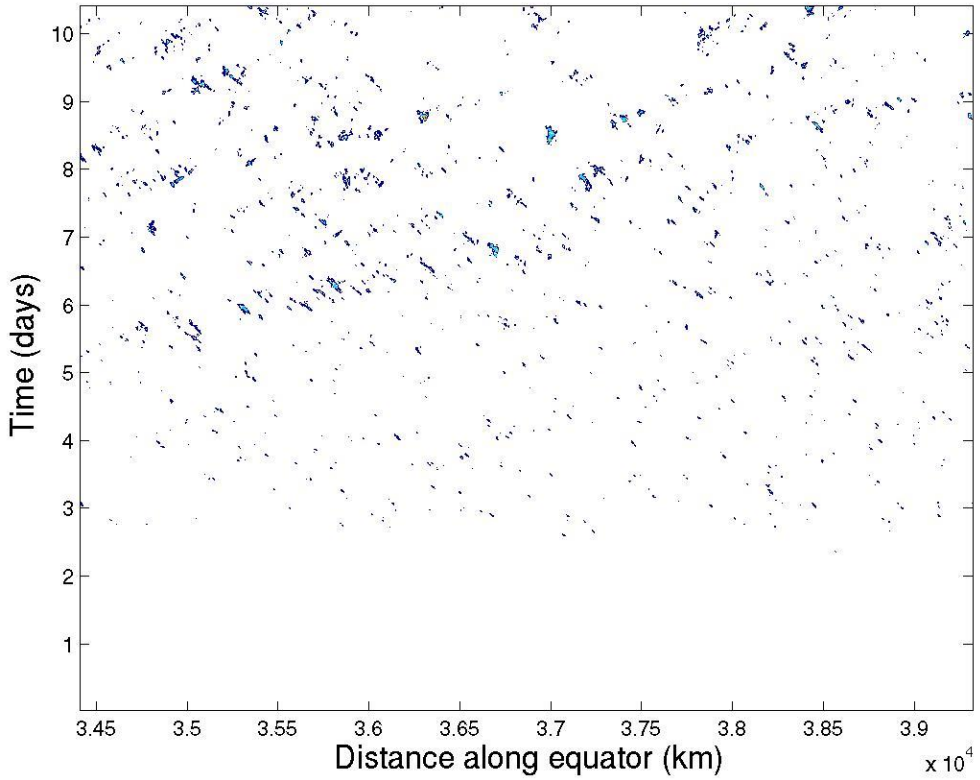

Hovmöller 8 – *35,000 – 40,000 km*